Title
Physical Phenotyping of Neutrophil NETosis Using Fluorescence-Imaging Deformability Cytometry

Author
Munoz, Hector Enrique

Publication Date
2020

Peer reviewed|Thesis/dissertation

UNIVERSITY OF CALIFORNIA

Los Angeles

Physical Phenotyping of Neutrophil NETosis Using Fluorescence-Imaging Deformability Cytometry

A dissertation submitted in partial satisfaction
of the requirements for the degree
Doctor of Philosophy in Bioengineering

by

Hector Enrique Muñoz

2020

ABSTRACT OF THE DISSERTATION

Physical Phenotyping of Neutrophil NETosis Using
Fluorescence-Imaging Deformability Cytometry

by

Hector Enrique Muñoz
Doctor of Philosophy in Bioengineering
University of California, Los Angeles, 2020
Professor Dino Di Carlo, Chair

The cell mechanical phenotype is a useful measure to understand cell identity and state. Cell mechanical properties such as deformability can provide an understanding of cellular processes or intracellular composition without direct labeling. The cell nucleus is a significant component of the cell and it is useful to understand how it impacts cell deformability. However, high throughput methods to measure cell deformability largely cannot directly integrate nuclear information. Here we present fluorescent imaging deformability cytometry (FI-DC), a high throughput platform capable of measuring cells in flow at 0.5 $m \cdot s^{-1}$, while providing simultaneous brightfield and fluorescent images. This technology enables us to identify cell subpopulations by their nuclear structure, as well as identify neutrophils undergoing neutrophil extracellular trap (NET) generation.

The dissertation of Hector Enrique Muñoz is approved.

Song Li

Aaron S. Meyer

Amy Catherine Rowat

Dino Di Carlo, Committee Chair

University of California, Los Angeles

2020

To Grammie and Grampie

We choose to go to the moon.
We choose to go to the moon in this decade and do the other things, not because they are easy, but because they are hard ...

– John F. Kennedy
September 12, 1962
Rice University
Houston, TX

Table of Contents

List of Figures

List of Tables

Acknowledgments

Chapter 2 is adapted from "Single-cell analysis of morphological and metabolic heterogeneity in *Euglena gracilis* by fluorescence imaging flow cytometry". Analytical Chemistry (2018). ML, CTR, HEM, and DD designed experiments. NN and KG brainstormed on experiment design and provided feedback. ML performed experiments with assistance from CTR. HEM performed analysis and interpretation of data. ED, JL, KO, and MB developed and assisted with operating imaging cytometry equipment and software. ML and HEM wrote the manuscript with contributions from NN, KG, CTR, and DD. DD supervised the project.

Chapter 3 is adapted from "Fractal-LAMP: Label-free analysis of fractal precipitate for digital loop-mediated isothermal nucleic acid amplification". ACS Sensors (2020). CTR, HEM, JEK, MvZ performed experiments. HEM analyzed data, and prepared the manuscript. OBG, AO, DD provided guidance throughout the work.

Chapter 4 is adapted from "A comparison of microfluidic methods for high throughput cell deformability measurements". Nature Methods (2020). JG, DD, and SRM conceptualized the project. MU, HEM, and JB performed the experiments and analyzed the data. OO provided methodological support with sDC data acquisition and analysis. MU and HEM visualized the data and prepared the original manuscript draft. All authors revised and edited the manuscript. JG, DD, SRM, and OO acquired funding.

This work was supported by funding from the ImPACT Program of the Council of Science, Technology and Innovation, and from the National Science Foundation Emerging Frontiers & Multidisciplinary Activities Division.

Thank you, God, for all the wonderful opportunities and people I have had in my life. I would not be the person I am today without these gifts. I have been blessed with an amazingly supportive family that has been instrumental in my success today. My parents Joan and Hector have supported and encouraged any interest I have ever had and instilled curiosity and passion in me. I have been fortunate to have a lifelong best friend in my sister, Elena. She has long been one of my biggest fans, and my childhood and adulthood would have been too empty without her. I have been lucky to have loving and caring grandparents in Carmen and Hector, and the late Marian and Frank, who could not be here to see the conclusion of my educational journey.

Graduate school would have been far more difficult and not quite as exciting without my best friend, fiancée, and future wife Jenny by my side. She has been with me for nearly all my time at UCLA and supported and celebrated me at each and every milestone. She remained a source of joy and happiness during the many dark times of frustration and stress along the way. The memories of our young and growing relationship will always be entwined with my journey through graduate school.

I have been lucky to have Dino as a wonderful mentor and advisor while at UCLA. He has always been engaged and excited in my work, and his own curiosity has fueled my own. I will forever be grateful for the opportunity to join his lab many years ago and cannot imagine what type of scientist and engineer I would have become under another advisor.

I have had the pleasure of learning from innumerable lab members that have made me a better researcher and communicator. Oladunni has become one of my dearest friends, and without her and our selfless blood donors, much of this work would never have come to exist.

All this work would not be possible without all the collaborators and advisors involved in the projects. Each person contributed in ways that improved the project in ways I, independently, could not have. Marta was instrumental in shaping our project into the strong piece of work it became, and in keeping the endeavor alive over many years.

Finally, I would like to thank the California sun, the music of Yo-Yo Ma, and coffee for making everything a little bit better.

Curriculum Vitae

2007 – 2011	B.S. in Bioengineering, Rice University.
2011 – 2013	Postbaccalaureate Fellow, National Institutes of Health
2013 – Present	Ph.D. Candidate in Bioengineering, University of California, Los Angeles (UCLA).
2013 – 2017	Cota-Robles Fellowship, Graduate Division, UCLA.

Publications

(In Progress) **Muñoz HE**, Lin J, Yeh B, Biswas T, Di Carlo D. Fluorescence Imaging Deformability Cytometry: Integrating Nuclear Structure with Mechanical Phenotyping.

Muñoz HE*, Urbanska M*, Bagnall JS, Otto O, Manalis SR, Di Carlo D, Guck J. A comparison of microfluidic methods for high-throughput cell deformability measurements. *Nature Methods* (2020).

Muñoz HE, Riche CT, Kong JE, van Zee M, Garner OB, Ozcan A, & Di Carlo D. Fractal LAMP: Label-Free Analysis of Fractal Precipitate for Digital Loop-Mediated Isothermal Nucleic Acid Amplification. *ACS Sensors* (2020).

Orfanos S, Jude J, Deeney BT, Cao G, Rastogi D, van Zee M, Pushkarsky I, **Muñoz HE**, Damoiseaux R, Di Carlo D, & Panettieri RA. Obesity increases airway smooth muscle responses to contractile agonists. *American Journal of Physiology-Lung Cellular and Molecular Physiology* (2018).

Muñoz HE*, Li M*, Riche CT, Nitta N, Diebold E, Lin J, Owsley K, Bahr M, Goda K, & Di Carlo D. Single-Cell Analysis of Morphological and Metabolic Heterogeneity in *Euglena gracilis* by Fluorescence-Imaging Flow Cytometry. Analytical Chemistry (2018).

Li M, **Muñoz HE**, Goda K, & Di Carlo D. Shape-based separation of microalga *Euglena gracilis* using inertial microfluidics. *Scientific Reports* (2017).

Li M, **Muñoz HE**, Schmidt A, Guo B, Lei C, Goda K, & Di Carlo D. Inertial focusing of ellipsoid *Euglena gracilis* cells in a stepped microchannel. *Lab on a Chip* (2016).

Burns JE, Yao J, **Muñoz HE**, & Summers RM. Automated Detection, Localization, and Classification of Traumatic Vertebral Body Fractures in the Thoracic and Lumbar Spine at CT. *Radiology* (2016).

Muñoz HE, Che J, Kong JE, & Di Carlo D. Advances in the production and handling of encoded microparticles. *Lab on a Chip* (2014).

Yao J, Burns JE, **Muñoz HE**, & Summers RM. Cortical Shell Unwrapping for Vertebral Body Abnormality Detection on Computed Tomography. *Computerized Medical Imaging and Graphics* (2014).

Burns JE, Wiese T, Yao J, **Muñoz HE**, Jones EC, & Summers RM. Automated Detection of Sclerotic Metastases in the Thoracolumbar Spine at CT. *Radiology* (2013).

CHAPTER 1

Introduction

Biological research has largely focused on gene and protein expression of cells, which provide fine scale details of processes in cells. Mechanical phenotyping has emerged as a method to measure mechanical properties of cells, specifically, the cells' deformability or stiffness under an applied load [1]. Mechanical phenotyping provides an integrative picture of the composition and organization of cells, as it may be affected by the cytoskeleton, nucleus, cell membrane, or other organelles. This form of phenotyping is attractive over other traditional methods in that it generally does not require cell labeling and is mostly non-destructive.

Mechanical phenotyping has been used to determine cell identity or disease state including changes in cell cycle [2], leukocyte activation [3], cancer malignancy [4], and cell differentiation [5, 6]. There are many methods to measure cell deformability including atomic force microscopy (AFM) [7], passing cells through constrictions [8], or deforming cells hydrodynamically in microfluidic devices [5, 2]. All these methods measuring cells are inherently measuring single cells, which provides granular details that may reveal cell heterogeneity, which may otherwise be lost when measuring properties at the tissue level. Newer microfluidic methods often provide high throughputs, which makes it easier to measure more cells, and understand the topology of the cells' mechanical properties.

While some deformability methods indirectly measure cells via changes to frequency [9] or current [10], many of these methods utilize high speed video or images for analysis. Using images to assess deformability provides rich data that can be used to completely understand cell shape, size, texture, and other morphological properties.

While mechanical phenotyping often aims to be label-free, there is value in understanding

how measured cell deformability relates to intracellular composition or gene and protein expression levels. Recent work has sought to bridge this gap in deformability cytometry by providing fluorescence integration, although this does not provide fluorescent images [11, 12]. This follows a trend in improvements in fluorescence imaging flow cytometry [13, 14, 15]. To date, high speed cell deformability methods have been unable to leverage conventional fluorescent imaging due to restrictions in fluoresce image integration time, but new, novel approaches can address this. Incorporating more imaging information, by adding brightfield and fluorescence images when possible will give us a more complete understanding of cell mechanical phenotyping assays.

These advances can be useful in investigating neutrophils, which undergo largescale internal reorganization when creating neutrophil extracellular traps (NETs) [16]. In addition to neutrophils' traditionally understood role in the immune system, it is now understood that they also create NETs, composed of their own chromatin, which serves to trap and kill pathogens. During this process, the neutrophil's chromatin decondenses and fills the cell as its nuclear envelope breaks down, before being released extracellularly with antimicrobials. Utilizing fluorescence enable cell deformability can enable us to understand how the cells' deformability changes in relation to the internal alterations. Identifying cells by their deformability may be useful in assessing pathogen load, or for future study, after sorting in flow.

Bibliography

[1] Eric M. Darling and Dino Di Carlo. High-Throughput Assessment of Cellular Mechanical Properties. *Annual Review of Biomedical Engineering*, 17(1):35–62, 2015.

[2] Oliver Otto, Philipp Rosendahl, Alexander Mietke, Stefan Golfier, Christoph Herold, Daniel Klaue, Salvatore Girardo, Stefano Pagliara, Andrew Ekpenyong, Angela Jacobi, Manja Wobus, Nicole Töpfner, Ulrich F Keyser, Jörg Mansfeld, Elisabeth Fischer-Friedrich, and Jochen Guck. Real-time deformability cytometry: on-the-fly cell mechanical phenotyping. *Nature Methods*, 12(3):199–202, 2015.

[3] T J Thauland, K H Hu, M A Bruce, and M J Butte. Cytoskeletal adaptivity regulates T cell receptor signaling. *Sci Signal*, 10(469):1–11, 2017.

[4] Henry T K Tse, Daniel R Gossett, Yo Sup Moon, Mahdokht Masaeli, Marie Sohsman, Yong Ying, Kimberly Mislick, Ryan P Adams, Jianyu Rao, and Dino Di Carlo. Quantitative diagnosis of malignant pleural effusions by single-cell mechanophenotyping. *Science translational medicine*, 5(212):212ra163, 2013.

[5] D. R. Gossett, H. T. K. Tse, S. a. Lee, Y. Ying, a. G. Lindgren, O. O. Yang, J. Rao, a. T. Clark, and D. Di Carlo. Hydrodynamic stretching of single cells for large population mechanical phenotyping. *Proceedings of the National Academy of Sciences*, 109(20):7630–7635, 2012.

[6] Jonathan Lin, Donghyuk Kim, Henry T. Tse, Peter Tseng, Lillian Peng, Manjima Dhar, Saravanan Karumbayaram, and Dino Di Carlo. High-throughput physical phenotyping of cell differentiation. *Microsystems & Nanoengineering*, 3:17013, May 2017.

[7] Manfred Radmacher. Studying the Mechanics of Cellular Processes by Atomic Force Microscopy. *Methods in Cell Biology*, 83(07):347–372, 2007.

[8] Kendra D. Nyberg, Kenneth H. Hu, Sara H. Kleinman, Damir B. Khismatullin, Manish J. Butte, and Amy C. Rowat. Quantitative Deformability Cytometry: Rapid, Calibrated Measurements of Cell Mechanical Properties. *Biophysical Journal*, 113(7):1574–1584, 2017.

[9] Sangwon Byun, Sungmin Son, Dario Amodei, Nathan Cermak, Josephine Shaw, Joon Ho Kang, Vivian C Hecht, Monte M Winslow, Tyler Jacks, Parag Mallick, and Scott R Manalis. Characterizing deformability and surface friction of cancer cells. *Proceedings of the National Academy of Sciences of the United States of America*, 110(19):7580–5, 2013.

[10] Yi Zheng, John Nguyen, Chen Wang, and Yu Sun. Electrical measurement of red blood cell deformability on a microfluidic device. *Lab on a Chip*, 13(16):3275–83, aug 2013.

[11] Ahmad Ahsan Nawaz, Marta Urbanska, Maik Herbig, Martin Nötzel, Martin Kräter, Philipp Rosendahl, Christoph Herold, Nicole Toepfner, Markéta Kubánková, Ruchi

Goswami, Shada Abuhattum, Felix Reichel, Paul Müller, Anna Taubenberger, Salvatore Girardo, Angela Jacobi, and Jochen Guck. Intelligent image-based deformation-assisted cell sorting with molecular specificity. *Nature Methods*, 17(6):595–599, jun 2020.

[12] Philipp Rosendahl, Katarzyna Plak, Angela Jacobi, Martin Kraeter, Nicole Toepfner, Oliver Otto, Christoph Herold, Maria Winzi, Maik Herbig, Yan Ge, Salvatore Girardo, Katrin Wagner, Buzz Baum, and Jochen Guck. Real-time fluorescence and deformability cytometry. *Nature Methods*, 15(5):355, 2018.

[13] Eric D Diebold, Brandon W Buckley, Daniel R Gossett, and Bahram Jalali. Digitally synthesized beat frequency multiplexing for sub-millisecond fluorescence microscopy. *Nature Photonics*, 7(10):806–810, sep 2013.

[14] Sebastian Karpf, Carson T. Riche, Dino Di Carlo, Anubhuti Goel, William A. Zeiger, Anand Suresh, Carlos Portera-Cailliau, and Bahram Jalali. Spectro-temporal encoded multiphoton microscopy and fluorescence lifetime imaging at kilohertz frame-rates. *Nature Communications*, 11(1):1–9, dec 2020.

[15] Hideharu Mikami, Jeffrey Harmon, Hirofumi Kobayashi, Syed Hamad, Yisen Wang, Osamu Iwata, Kengo Suzuki, Takuro Ito, Yuri Aisaka, Natsumaro Kutsuna, Kazumichi Nagasawa, Hiroshi Watarai, Yasuyuki Ozeki, and Keisuke Goda. Ultrafast confocal fluorescence microscopy beyond the fluorescence lifetime limit. *Optica*, 5(2):117, feb 2018.

[16] Volker Brinkmann, Ulrike Reichard, Christian Goosmann, Beatrix Fauler, Yvonne Uhlemann, David S. Weiss, Yvette Weinrauch, and Arturo Zychlinsky. Neutrophil Extracellular Traps Kill Bacteria. *Science*, 303(5663):1532–1535, mar 2004.

CHAPTER 2

Single-cell analysis of morphological and metabolic heterogeneity in *Euglena gracilis* by fluorescence imaging flow cytometry

2.1 Introduction

A grand challenge facing the world today is the depletion of fossil fuels, which are finite, non-renewable, and environmentally harmful. As alternatives to petroleum-based diesel fuel, biofuels produced by microalgae with energy-rich lipids are a promising solution [1, 2]. In comparison with other traditional terrestrial biofuel feedstocks, such as oil crops and plants, microalgae offer many potential advantages, including relatively higher lipid productivity [3], no need for arable land [4], control of water pollution [5], and a viable drop-in equivalent fuel product [6]. Moreover, microalgal biomass is rich in a variety of valuable nutrients including vitamins, proteins, amino acids, and essential trace minerals, which have already been utilized for dietary supplements, animal feeds, fertilizers, and biomaterials [7, 8].

Euglena gracilis (*E. gracilis*), a single-celled eukaryotic microalga, has been actively investigated as a production source for biofuels and biomass because of many beneficial traits. *E. gracilis* has been shown to efficiently accumulate neutral lipids (primarily wax esters) [9] that could be used for the production of lipid-based biodiesel and jet fuel, along with as many as 59 types of nutrients, such as β-carotene, paramylon (β-1,3-glucan), vitamins C and E, and Omega-3c [10, 11].

Unicellular microalgae (including *E. gracilis*) are highly diverse in terms of morphology,

and metabolite formation (metabolism). They have distinct and multiple endosymbiotic events, leading to substantial morphological and metabolic diversity. The size and shape of a cell in a given species can vary dramatically depending on the phase of the growth cycle (i.e. lag, exponential and stationary), biological clock proteins, and the conditions for photosynthesis versus respiration [12]. Moreover, these cells change shape [13, 14] and intracellular metabolite content [15, 16] in response to environmental conditions, such as exposure to light or changing pH. Due to the diversity and abundance of microalgae, it is essential to investigate large numbers of individual cells for the characterization of metabolite productivity at the population level as well as variations and divergence within populations.

Current analysis modalities have been limited in ability to characterize rare subpopulations of microalgae or incorporate morphological features in phenotypic stratification. Conventional analytical tools, such as thin-layer chromatography (TLC) [17], liquid chromatography tandem-mass spectrometry (LC-MS/MS) [18], gas chromatography-mass spectrometry (GC-MS) [19], are unable to characterize the heterogeneity within a population, and only assay the average phenotype, rather than identifying unique subpopulations or outlier cells. The number of cells needed for these analyses is in the range of 5×10^5-10^6 cells per sample, making it practically useless for the analysis of rare subpopulations. Moreover, these techniques involve extraction and chromatographic analysis of bulk samples, which are relatively time-consuming and labor-intensive. Although mass spectrometry imaging (MSI) [20], fluorescence microscopy [21], and Raman scattering microscopy [22, 23] could aid in profiling cellular morphological variations and intracellular molecular distributions, the throughput limits their application to rapidly assay a large number of cells. The large integration times for fluorescence acquisition with standard CMOS cameras also is prohibitive in obtaining non-motion-blurred images for highly motile cells such as *E. gracilis*. Flow cytometry (FC) [24] and fluorescence-activated cell sorting (FACS) [25] are widely used tools for high-throughput analysis of single mammalian cells, but they cannot provide morphological or molecular localization information achievable with intracellular imaging, which may impose limitations in characterizing accumulation of metabolites per biomass of

cells, for example. Previous work to perform IFC on *E. gracilis* utilized optical time-stretch microscopy, which provided bright field images and fluorescence values, but not fluorescence images [26] .

To overcome the limits associated with conventionally used analytical tools, it is imperative to develop more information-rich approaches that can evaluate algae lipid productivity or other metabolite productivity per biomass in a high-throughput and multiparametric manner, and at the single-cell level. Fluorescence imaging flow cytometry (FIFC) combines speed, statistical power, and fluorescence sensitivity of standard flow cytometry with both spatial and temporal resolution and quantitative morphology of digital microscopy, which is capable of reflecting cell-to-cell variability, and at the same time unraveling the complexity and interdependence of cellular components in the individual cells of a heterogeneous population.

Fluorescence Imaging using Radiofrequency-tagged Emission (FIRE) [27] is one of the fastest techniques that have been developed to speed up the acquisition of fluorescence images with the dynamic range and sensitivity of a photomultiplier tube (PMT). By using the beating of digitally synthesized optical fields to map the image into the radiofrequency spectrum, FIRE imaging enables over-kilohertz frame rate in fluorescence microscopy. Although FIRE operates at a throughput similar to what is possible with high-speed brightfield imaging flow cytometry based on serial time-encoded amplified microscopy (STEAM) [28], it is equipped with additional capabilities to quantitatively characterize intracellular metabolites and biomolecules, i.e. lipid droplets (LDs) and pigment autofluorescence such as chlorophyll, which has peak emission spectra ranging from 682-731 nm [29], and carotenoids [30].

Here, we use FIRE imaging in a hydrodynamic flow cytometric sample delivery format to analyze microalgae with a high spatial resolution, simultaneously acquiring two fluorescence (e.g. FITC [529/28 nm] and PE-Cy5 [679/41 nm]) and brightfield (BF) images of each cell (Figure 2.1a). These images are reconstructed from the frequency components associated with pixel positions over time (Figure 2.1b) as the microalgae transit the excitation line, enabling the analysis of cell morphology, intracellular lipid droplets (LDs) stained with

BODIPY$^{505/515}$ and chlorophyll distribution in BF, FITC and PE-Cy5 channels, respectively. The quality of images generated by our setup is comparable to that of images captured by a conventional wide-field fluorescence microscope with a metal-oxide-semiconductor (CMOS) camera (Figure 2.1c-d). Important features calculated from FIRE images include cell aspect ratio, cell circularity, cell area, total fluorescence, average chloroplast and lipid fluorescence, and chloroplast and lipid area (Figure 2.1e).

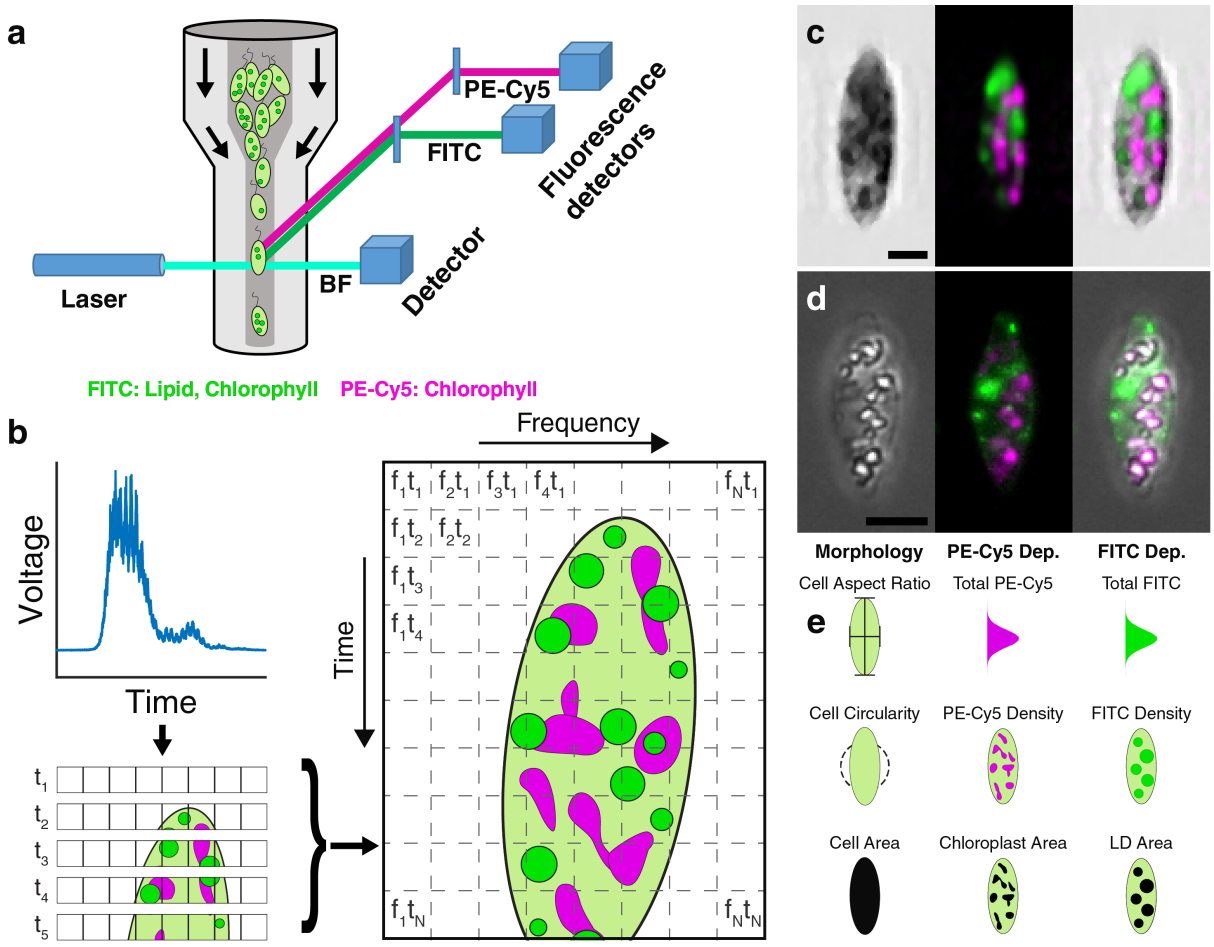

Figure 2.1: **FIRE imaging principle and calculated image features for *E. gracilis*.** (**a**) Simplified optical schematic of the analysis system. (**b**) In FIRE flow cytometry, a two-dimensional image is generated as a cell flows through the excitation line consisting of radiofrequency-multiplexed excitation across one spatial dimension. The time domain signal collected from scattered and fluorescence emissions contains the spatial intensity modulations

that can be transformed back into the 1D line via Fourier transform. These 1D lines of pixels collected over time are assembled into the 2D image. (**c**) The reconstructed FIRE images are comparable to conventional fluorescence microscopy images (**d**). Brightfield images (left) provide information on cell size and shape, while merged fluorescence images (right) capture largely intracellular chlorophyll autofluorescence (magenta, PE-Cy5 [679/41 nm]), and lipid droplets stained with BODIPY$^{505/515}$ fluorescent dye (green, FITC [529/28 nm]). Imaged with Nikon Ti-E microscope (20x/0.45 objective), and Photometrics CoolSNAP HQ2 camera (6.45 µm pixel pitch). Scale bars = 10 µm . (**e**) FIRE data can be used to extract intensity information in fluorescence channels, but also spatial information that yields new single-cell descriptors including cell aspect ratio, cell circularity, cell area (µm^2), total fluorescence (AFU), chloroplast and lipid fluorescence density (AFU $\cdot$ µm^{-2}), and chloroplast and lipid droplet area (µm^2).

We apply the FIRE imaging flow cytometer to obtain a morphological atlas of images of *E. gracilis* under heterotrophic conditions, and following dark anaerobic fermentation for up to three days. We find that over the course of three days of fermentation, autofluorescence of chlorophyll within chloroplasts decreases, while both the stained lipid fluorescence intensity and area increase. We establish new chemo-morphological-based descriptors of cells which uncover unique subpopulations of cells with high lipid biomass production per unit area, which may not be as brightly stained for lipid dyes, and ignored by conventional flow cytometry. Our FIRE imaging approach and metrics for lipid productivity are validated by a high correlation ($R^2 > 0.90$, $p < 0.005$) with bulk lipid extraction in the same population. We anticipate that future imaging flow cytometry can enable identification of valuable strains and image-based sorting can eventually be used as part of a selection process for evolution of highly productive strains.

2.2 Experimental

2.2.1 Experimental design

The primary objective of this study was to develop novel metrics to identify high lipid-producing *E. gracilis*. FIRE was selected to image the cells due to its fast brightfield and fluorescence imaging capability in flow. *E. gracilis* cultures were subject to dark, anaerobic fermentation with times ranging from 0 hours to 3 days. This enabled lipid accumulation over time, leading to different distributions of lipid content in cells for 6 samples in total. All samples were processed and compared by FIRE on the same day after staining lipids with BODIPY$^{505/515}$, with a fraction of each sample reserved for gravimetric measurements of lipid production at a population level. An additional culture of *E. gracilis* was split and stained with different BODIPY$^{505/515}$ concentrations, ranging from 1.25 µm to 50 µm , to understand variations and effects due to staining.

2.2.2 Fluorescence imaging microscopy by beat frequency multiplexing

FIRE is an emerging technique that enables higher imaging speed (namely, temporal resolution) for fluorescence microscopy compared to conventional cameras by using high-sensitivity PMTs to readout signal. The approach enables over-kilohertz frame rate of high-speed imagers with higher light sensitivity and dynamic range of conventional cytometry. The FIRE setup uses a 100 mW, 488 nm laser, with FITC (529/28 nm) and PE-Cy5 (679/41 nm) band-pass filters. The transmitted light is measured using a photodiode to generate brightfield images while side scattered light is collected with a PMT to generate darkfield images. All generated images have a pixel pitch of 0.5 µm per pixel. The technique is described in more detail in previous work [27]. Approximately 4,000 events were recorded per sample.

2.2.3 Image analysis

First, raw images in three channels, BF (morphology and size), FITC (LDs stained by BODIPY$^{505/515}$ and chlorophyll autofluorescence), and PE-Cy5 (chlorophyll autofluorescence), are measured. Cells are segmented from BF images, and morphology metrics are calculated. Intracellular lipid and chloroplast structures are segmented from fluorescence channels by independent thresholding according to normal levels of extracellular fluorescence. Regions of high similarity between FITC and PE-Cy5 channels are identified for exclusion by computing Normalized Mutual Information (NMI) [31] and Normalized Cross-Correlation (NCC) [32] maps to compensate for the autofluorescence signals across both channels. Finally, various metrics such as the value of lipid droplets (LDs) to cell area ratio (LCAR), the parameter for evaluating lipid productivity per biomass, are calculated. A detailed workflow and information can be found in Figure 2.A.1.

2.2.4 Cell culture and treatment

The *E. gracilis* cells used in the study are *Euglena gracilis Z* (NIES-48) strain procured from Microbial Culture Collection at the National Institute for Environmental Studies (NIES), Japan. *E. gracilis* were cultured heterotrophically in 500 mL flasks using Koren-Hutner (KH) medium (pH 3.5) [33]. The cell cultures were kept at 29 ℃ with a shaking rate of 120 strokes $\cdot$ min under continuous illumination of 100 µmol photons $\cdot$ m^{-2} $\cdot$ s^{-1}. The fermentation was performed on cells in stationary phase by bubbling with nitrogen gas and incubating the flasks in the dark for three days.

2.2.5 BODIPY$^{505/515}$ staining of intracellular lipid droplets

The BODIPY$^{505/515}$ stock was prepared by dissolving original dye powder (4,4-Difluoro-1,3,5,7-Tetramethyl-4-Bora-3a,4a-Diaza-*s*-Indacene, D3921, Thermo Fisher Scientific) into 4 mL dimethyl sulfoxide (DMSO) with a concentration of 2.5 mg $\cdot$ mL^{-1}. The stain stock solution was diluted 1,000 times with distilled water before use. The *E. gracilis* cells in the

culture medium were washed with distilled water and resuspended in distilled water with a final concentration of around 2×10^6 cells $\cdot$ mL^{-1}. We mixed 2.5 µg $\cdot$ mL^{-1} BODIPY$^{505/515}$ solution with *E. gracilis* cell suspension solution at a volume ratio of 1:1, which is followed by gentle vibration and incubation in the dark for 10 min. The final concentration of BODIPY$^{505/515}$ and *E. gracilis* cells are 1.25 µg $\cdot$ mL and 10^6 cells $\cdot$ mL, respectively. The *E. gracilis* cells were washed three times with distilled water by centrifugation (2000g, 1 min), and then resuspended in distilled water and protected from light before taking imaging flow cytometric measurements.

2.2.6 Lipid extraction and quantification

E. gracilis cells in the culture medium were collected by centrifugation (5000g, 2 min) and washed with distilled water. The harvested *E. gracilis* cells were dried in a freeze dryer (FDV-1200, EYELA), and the lipid component was extracted using *n*-hexane as indicated in the previous report [34]. *n*-hexane was used to adhere to the cited report, but n-heptane is a less toxic substitute. In brief, 10 mg of dried algal cells was suspended in 10 mL of *n*-hexane, and the cells were disrupted twice for 90 s using a probe sonicator (Q125, QSonica). The *n*-hexane aqueous solution with dissolved lipid was collected by filtering through a piece of glass microfiber filter paper (GF/F, 1825-047, Whatman). The solution was then evaporated and dried overnight, and the weight of the residue was measured and quantified as the extracted total lipid. Bulk lipid extraction was performed on the samples of heterotrophically cultured *E. gracilis*, fermented for different durations. Least squares linear regression was performed with each sample's bulk lipid extraction ratio and the proposed lipid-production metrics (Figure 2.A.2).

2.2.7 Statistical analysis

All fluorescence-derived parameters are reported with a $\log_{10}$ transformation, which results in an approximately normal distribution when unimodal. Two-tailed Student's t tests are used to compare changes in chloroplast area, total PE-Cy5 intensity, and chlorophyll density

between the start (0 hours) and end (3 days) of fermentation. These follow the t test requirements for approximately normal distributions with equal variance. The comparison of chloroplast to cell area ratio (CCAR) at the start and end does not fulfill these requirements and requires the non-parametric two-tailed Wilcoxon rank sum test. Similarly, lipid droplet area, total FITC intensity, lipid density and lipid to cell area ratio (LCAR) are not normally distributed with equal variance, so a one-tailed Wilcoxon rank sum test is used as we expected these values to increase with fermentation time. The variability of total FITC intensity versus LCAR when varying BODIPY$^{505/515}$ staining concentrations is assessed using the non-parametric Kruskal-Wallis H test due to their non-normal distributions. Least squares linear regression is performed on calculated cell metrics that may vary with fermentation time, or with cell shape or area.

2.3 Results and discussion

2.3.1 Imaging flow cytometric analysis reveals morphology and intracellular metabolite variations

We used FIRE imaging flow cytometry to characterize morphological heterogeneity, intracellular state of chlorophyll and LDs, and potential correlations between these morphological and molecular parameters at the single-cell level. Heterotrophically cultured *E. gracilis* cells undergoing fermentation in dark and anaerobic conditions up to 3 days were analyzed. PE-Cy5 and FITC fluorescence signals show the changes in chlorophyll and LDs with fermentation time, respectively (Figure 2.2a). The increase in FITC signal due to the accumulation of intracellular LDs during fermentation [35] is clear starting at 6 hours, and continues through 3 days. The changes in FITC signal reflect a larger spread in distribution within the population with increased fermentation time, rather than a systemic shift in the population. This implies that *E. gracilis* cells in the population are not fermenting uniformly, and there are cells that are not accumulating much lipid, while other cells have up to 2 orders of magnitude higher fluorescence intensity, indicating significantly higher lipid accumula-

tion. However, from total fluorescence intensity measurements alone, which traditional FC provides, it is difficult to ascertain whether factors such as cell size, shape or intracellular structure contribute to these overall changes in fluorescence intensity.

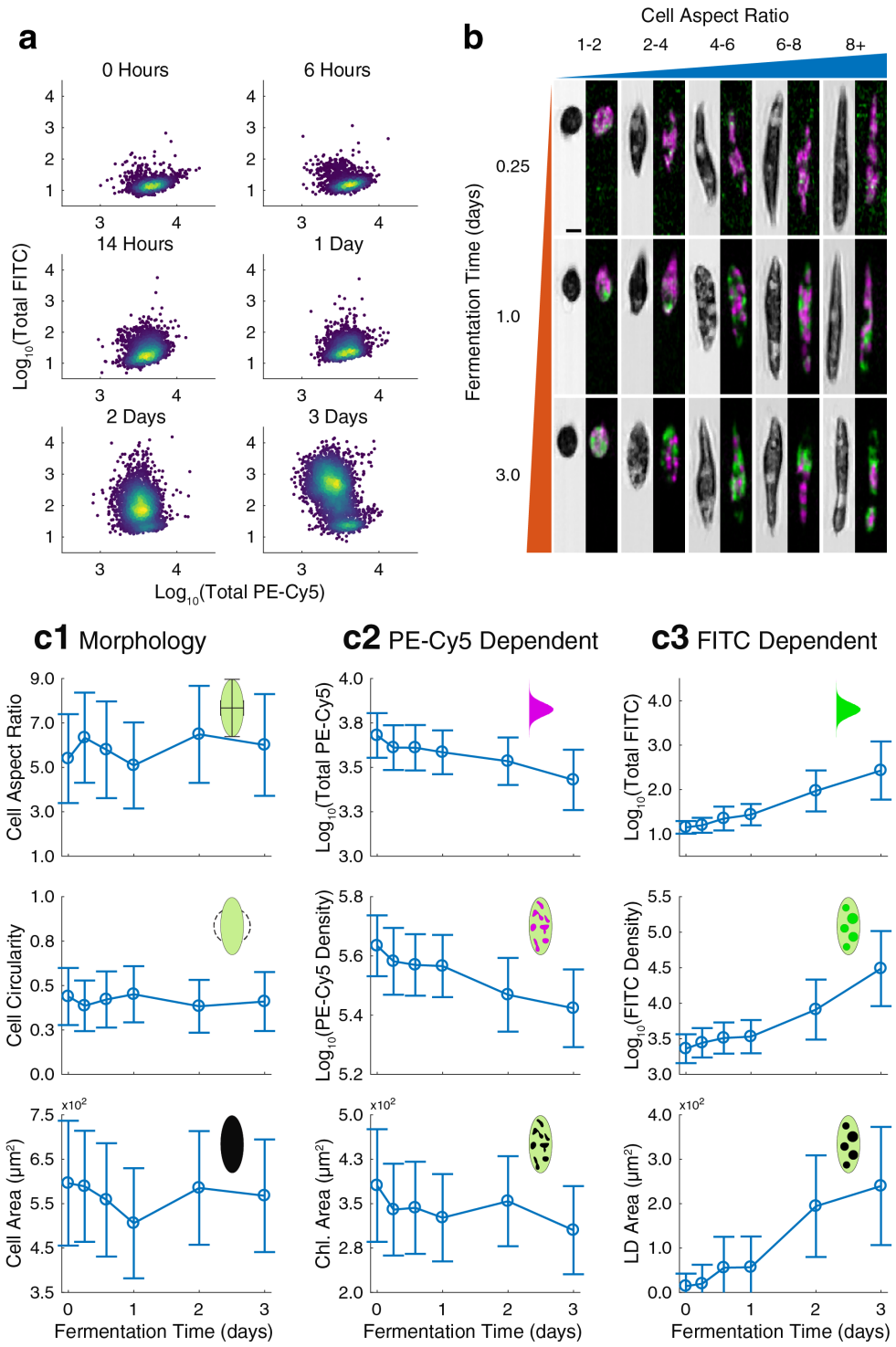

Figure 2.2: **Evaluation and evolution of cellular heterogeneity for *E. gracilis* under dark anaerobic fermentation.** (**a**) Density scatter plots of total fluorescence signals from pigments within chloroplasts and stained lipids throughout fermentation. Increased fermentation time induces increased lipid accumulation on average, which can be seen in the increasing levels of overall fluorescence in the FITC channel (529/28 nm, correlated with higher BODIPY$^{505/515}$ staining and chlorophyll levels). (**b**) FIRE images of *E. gracilis* across the range of fermentation times reveal a variety of cell shapes, as represented by aspect ratio, or length of major axis dived by the minor axis of the cell. Fluorescence images (right) include PE-Cy5 (679/41 nm, magenta), which contain chlorophyll autofluorescence and FITC (green), which is dominated by BODIPY$^{505/515}$ staining of lipid droplets, but also contains autofluorescence from chlorophyll. Scale bar = 10 µm . (**c1**) Morphology-dependent parameters calculated throughout fermentation reveal trends in intracellular composition. (**c2** & **c3**) Chlorophyll and lipid droplet content (AFU) are inversely correlated during fermentation, while there is no systemic change in cell size (µm^2) or shape. The decrease in intracellular chlorophyll reflects decreased fluorescence density of autofluorescent pigment (AFU · µm^{-2}), rather than overall diminished chloroplast area (µm^2). Error bars represent standard deviation.

In addition to the overall intensity of fluorescence, FIRE imaging flow cytometry provides precise morphological information from images in brightfield and fluorescence channels that can be combined to compute the spatial arrangement of intracellular components. *E. gracilis* cells across all states of fermentation display a wide range of cell morphology, which can be seen in brightfield images (Figure 2.2b). Brightfield images enable calculation of cell shape metrics, including cell area, perimeter, length, width, aspect ratio and solidity. At the beginning of fermentation (i.e. 0 hours), *E. gracilis* cells in the population have a mean aspect ratio of 5.4 ± 2.0, mean circularity of 0.44 ± 0.16, and mean cell area of 596 ± 141 µm^2 (Figure 2.2c1). After three days of fermentation, we measured a mean aspect ratio of 6.0 ± 2.3, mean circularity of 0.41 ± 0.16, and mean cell size of 568 ± 127 µm^2. Over the course

of fermentation, there is no strong correlation between cell aspect ratio and fermentation time ($R^2 = 0.12$, $p = 0.50$), cell circularity and fermentation time ($R^2 = 0.08$, $p = 0.58$), or cell area and fermentation time ($R^2 = 0.01$, $p = 0.83$).

The strong autofluorescence of chlorophyll and its relative abundance compared to other pigments in the *E. gracilis* provides a clear label-free image in the PE-Cy5 channel to characterize chloroplasts in terms of both size and chlorophyll content, which aligns with visible pigments (Figure 2.A.3). Chlorophyll a and b account for more than 75% of pigment molecules in *E. gracilis*, including carotenoids (neoxanthin, diadinoxanthin, and β-carotene) [30]. Changes in critical parameters at the beginning (i.e. 0 hours) and end of fermentation (i.e. 3 days) are compared with a two-sided t-test; the $\log_{10}$ transform of all fluorescence derived parameters is reported. We found that at the beginning of fermentation, mean total PE-Cy5 intensity per cell is 3.68 ± 0.13 AFU, mean chloroplast area per cell is 381 ± 95 μm^2, and mean chloroplast area per cell area is 0.65 ± 0.11. After three days of fermentation, mean total PE-Cy5 intensity per cell is 3.43 ± 0.17 AFU ($p < 0.001$, 95% CI [0.24, 0.26]), mean chloroplast area per cell is 305 ± 74 μm^2 ($p < 0.001$, 95% CI [71, 79]), and mean chloroplast area per cell area is 0.55 ± 0.13 (Figure 2.2c2). A Wilcoxon rank sum test indicates a statistically significant change in the chloroplast area per cell area over fermentation time ($Z = 32.9$, $p < 0.001$). These significant findings illustrate a decrease in chlorophyll content from the beginning to the end of fermentation.

Accumulated lipid droplets are visualized in the FITC channel using $BODIPY^{505/515}$ dye, however, there is an overlap of chlorophyll autofluorescence and $BODDIPY^{505/515}$ when excited at the 488 nm wavelength of FIRE (Figure 2.A.3). FIRE's ability to generate multi-channel images concurrently allows signals across channels to be colocalized spatially. This is especially valuable when quantifying the lipid content of *E. gracilis*, as chlorophyll autofluorescence may appear in the FITC channel, but fluorescence compensation is applied using the chlorophyll signal in the PE-Cy5 channel. This allows lipid droplets to be quantified in both size and content. Changes in critical parameters at the beginning (i.e. 0 hours) and end of fermentation (i.e. 3 days) are compared with a one-tailed Wilcoxon rank sum test;

the $\log_{10}$ transform of all fluorescence derived parameters is reported. At the beginning of fermentation, *E. gracilis* cells in the population have a mean total FITC intensity per cell of 1.15 ± 0.14 AFU, and average lipid droplet area of 14 ± 28 µm^2 (Figure 2.2c3). While after three days of fermentation, we measured a mean total FITC intensity per cell of 2.43 ± 0.65 AFU (Z = -70.8, $p < 0.001$), and mean lipid droplet area of 240 ± 133 µm^2 (Z = -60.8, $p < 0.001$).

Chlorophyll and lipid structural and intensity metrics were also analyzed as a function of the morphological properties of individuals cells, yielding more refined segmentation of the subpopulations of cells. The entire dataset as a function of cell aspect ratio and area is presented in Figure 2.A.4. We see that cell area correlates with LD area, chloroplast area, and chlorophyll intensity, while aspect ratio does not have a strong correlation with these parameters. Closer inspection of the relationship between aspect ratio, fluorescence intensity, and fermentation time indicates that there is not an overall trend that relates the three parameters (Figure 2.A.5). However, this same inspection applied to cell area, fluorescence intensity, and fermentation time reveals a trend towards smaller cells during the first 24 hours of fermentation time and increased PE-Cy5 levels in larger cells (Figure 2.A.6). This suggests that normalization of fluorescence metrics with respect to cell area can remove correlated effects of structural changes on molecular readouts.

Fluorescence intensity information provided by a traditional flow cytometer misses key information that can explain cell structural and molecular changes. Changes in overall chlorophyll or lipid fluorescence signal cannot be ascribed to either changes in structure or density of intracellular fluorophores with an overall intensity measurement alone. There is a noticeable decrease in overall chlorophyll signal throughout fermentation as noted previously, which continues throughout the fermentation period, according to a least squares linear regression (R^2 = 0.95, $p < 0.01$). However, this decrease cannot be explained well by a decrease in chloroplast area with fermentation time (R^2 = 0.45, p = 0.14). Instead, this decrease is more strongly correlated to the decrease in chlorophyll density (AFU/µm^2) (R^2 = 0.96, $p < 0.001$) in each chloroplast, and therefore suggests a reduction in chlorophyll

content in each chloroplast for cells undergoing fermentation. This is further supported when comparing the standardized coefficients of a multiple linear regression of overall chlorophyll content as a function of chlorophyll density and chloroplast area. The standardized coefficient of chlorophyll density (0.78) is more than 2.5 times greater than that of chloroplast area (0.28), indicating its contribution to overall chlorophyll signal.

2.3.2 Normalizing fluorescence intensity by cell size corrects cellular lipid productivity

Identifying high lipid per biomass producing *E. gracilis* by total FITC signal alone is problematic because it does not account for factors that can contribute to FITC intensity, such as cell size, variations in BODIPY$^{505/515}$ staining, background fluorescence signal, chlorophyll autofluorescence and imaged doublets. Furthermore, we have found that cells of different sizes can have the same FITC intensity, although smaller cells with high FITC are expected to be more efficient in converting biomass to lipid product (Figure 2.A.6). We aimed to address these issues using image-based metrics. We developed an algorithm to quantify lipid production utilizing area of lipid droplets detected in FITC, corrected for any autofluorescence appearing to be co-localized in both FITC and PE-Cy5 images via image processing (Figure 2.A.1). Furthermore, we normalized the lipid droplet area by cell size to calculate the Lipid to Cell Area Ratio (LCAR), to more closely approximate lipid productivity per biomass (Figure 2.3a). Our algorithms to automatically calculate LCAR correlated well to manually defined LCAR with $R^2 = 0.68$ ($p < 0.001$) (Figure 2.A.7).

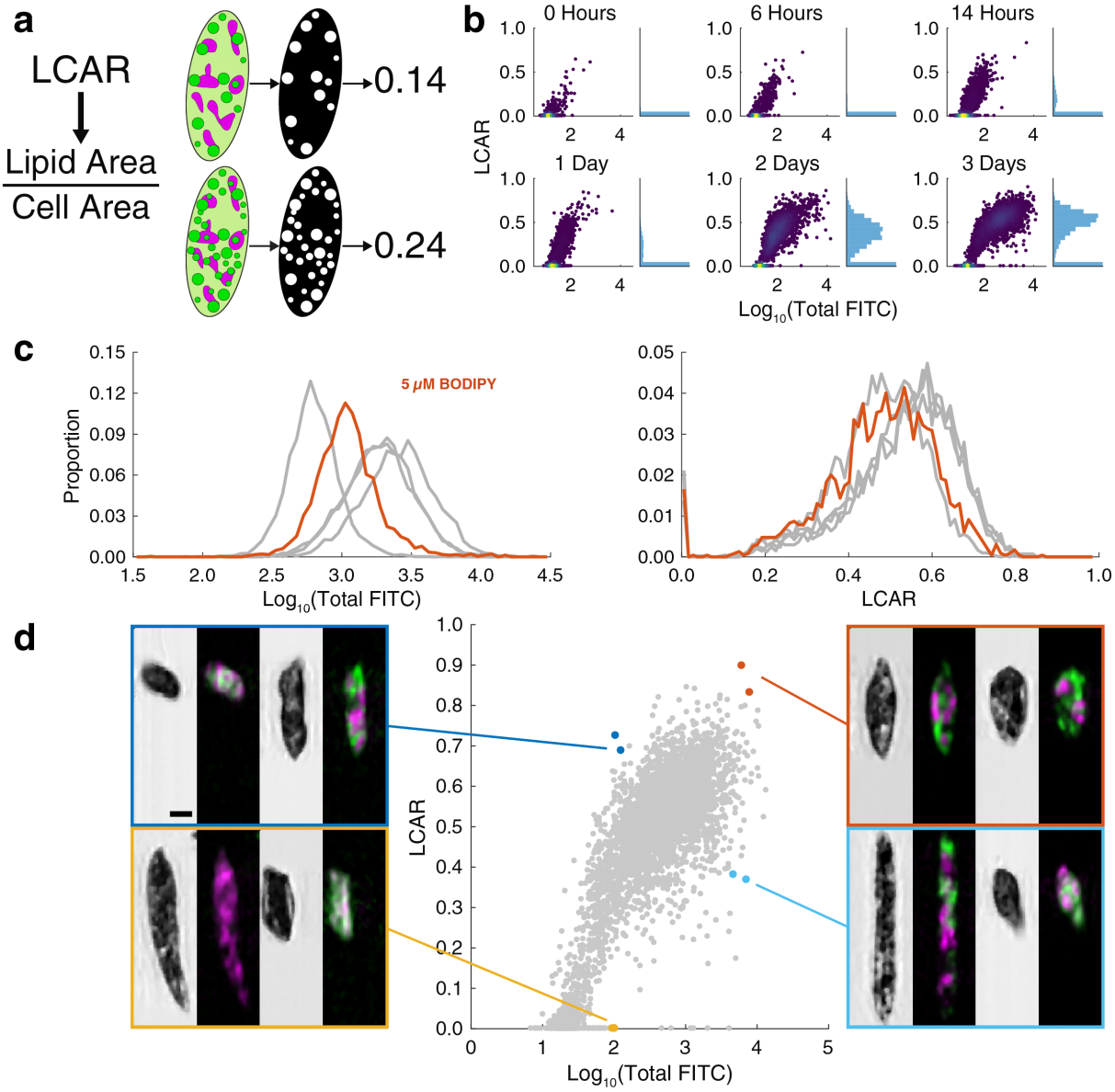

Figure 2.3: **Normalization by size improves the evaluation of cellular lipid productivity.** (**a**) Schematics of Lipid to Cell Area Ratio (LCAR), which approximates microalgal lipid productivity per biomass. The area of BODIPY$^{505/515}$ stained lipid droplets detected in FITC (529/28 nm, green) uncorrelated with PE-Cy5 (679/41 nm, magenta) intensity regions is normalized by cell area. (**b**) Calculated LCAR increases with fermentation time (histogram) and is positively correlated with FITC intensity ($R^2 = 0.83$, $p < 0.001$). (**c**) *E. gracilis* cells stained at 5 µm BODPIY (orange) maintain similar LCAR levels with cells

stained with a range of BODIPY$^{505/515}$ concentrations (1.25 to 50 µm ; gray), despite heavy variation in FITC intensity. (**d**) LCAR provides enhanced information at the single cell level in the population fermented for 3 days. Both LCAR and FITC reveal high lipid-producing cells (orange), but for similar LCAR levels, FITC values span orders of magnitude. At lower FITC values (blue), LCAR identifies cells that have a small area, but high lipid accumulation per biomass. Likewise, cells with high FITC and reduced LCAR (light blue) may exhibit high chlorophyll autofluorescence in FITC, or larger cell size. Both metrics identify non-producing cells at the lower limits of each range (yellow). Scale bar = 10 µm .

LCAR is a more attractive parameter for lipid productivity than FITC because it normalizes by cell size. All values fall between 0 and 1, while FITC has a wide range that must be calibrated for different conditions. Across all fermentation durations, there is a strong positive correlation between LCAR and FITC signal (R^2 = 0.83, $p < 0.001$) (Figure 2.3b). Heterotrophically cultured *E. gracilis* had a mean LCAR of 0.01 ± 0.03, and after three days of dark and anaerobic culture, we measured a mean LCAR of 0.44 ± 0.23, which was a significant increase according to a one-tailed Wilcoxon rank sum test (Z = -67, $p < 0.001$). Interestingly, LCAR reveals a bimodal bifurcation of the population during fermentation where a large fraction of cells maintain a value of zero LCAR, while the fraction of the population and average value of LCAR both increase with fermentation time. This bifurcation in the population is less clear in the FITC intensity alone. The same *E. gracilis* population stained across a range of BODIPY$^{505/515}$ concentrations including 1.25 µm , 5 µm , 6.25 µm , 12.5 µm , 25 µm , and 50 µm demonstrated a wide variation between samples, while LCAR was largely consistent across samples (Figure 2.3c). *E. gracilis* stained with 5 µm BODIPY$^{505/515}$ had similar LCAR values to the other BODIPY$^{505/515}$ staining concentrations, while the FITC values of all stains vary widely. It should be noted that because LCAR relies on thresholding, the main requirement for uniformity is that sufficient staining is necessary to maintain a signal above the background noise level.

Looking at a plot of LCAR vs. total FITC intensity following 3 days of fermentation

reveals unique outlier cells that may be important for lipid productivity that would not be identified with FITC intensity alone (Figure 2.3d). For example, in the upper left quadrant two representative high LCAR cells with low FITC are shown. The smaller cell size leads to a lower FITC signal, although it would be anticipated that these cells would produce high levels of lipid per biomass. Cells in the lower left quadrant have similar FITC intensity, due to high chlorophyll content, but are found to have no lipid droplets when observing images. Both metrics can pick up high-producing cells (upper right quadrant).

Lipid droplet intensity information is also improved by normalizing according to cell area or droplet area (Figure 2.A.8). Lipid droplet intensity per cell area is an alternative metric to approximate lipid production per biomass. It assumes the quantitative reliability of FITC signal, but is scaled to avoid selecting for large cells, and missing high producing small cells. If ignoring chlorophyll contributions to FITC intensity, cell FITC per cell area can more easily approximate this value. Lipid droplet intensity per droplet area is another potentially useful metric to characterize the properties of lipid droplets produced by *E. gracilis*. Given that BODPIY staining is correlated to lipid content, this measure can identify cells that create higher density lipid droplets, or how lipid production varies across culture conditions. However, these intensity-based measurements rely on BODIPY$^{505/515}$ staining performance and identical imaging conditions between samples.

Although we cannot currently test these metrics with secondary approaches to verify lipid content at the single-cell level, when comparing at the population level using bulk lipid extraction, area-normalized metrics performed similarly to total FITC intensity in terms of least squares linear regression (Figure 2.A.2). All methods had R^2 greater than 0.90, ($p < 0.01$), with Total FITC Intensity and Droplet FITC per Cell Area achieving 0.94, LCAR achieving 0.92, and Cell FITC per Cell Area achieving 0.93. Notably, all metrics underestimate the bulk lipid extraction calculated for the 1-day fermentation. These results indicate that there are multiple methods that correlate well in aggregate, although there are differences that arise when comparing cells individually.

2.3.3 The capability to image cells reduces false positive events

Visualizing the cell improves data collection and analysis by excluding partially visible cells, multiple cells, and normalizing signals to cell area. As discussed, the origin of increased fluorescence with the size of a cell is not clearly recognized in fluorescence intensity data alone. Fluorescence intensity information will also fail to identify images with multiple cells present, leading to an increased FITC signal (Figure 2.4a). Multi-cell images may be captured when cells are dividing or have become stuck together (Figure 2.4b). Morphology data can be algorithmically analyzed to identify and exclude multi-cell images using shape metrics such as cell area or cell width (Figure 2.4c). Cell solidity is the ratio of cell area to its respective convex outlined shape and provides another useful metric to find clusters of connected cells (Figure 2.4d). Across all fermentation times, we performed double cell random forest classification using shape metrics and achieved 90.99% sensitivity and 99.93% specificity in identifying multiple-cell events. In contrast, random forest classification performed using only side scatter area and height, and axial light loss area and height, which are routinely used in doublet discrimination, provided lower sensitivity and specificity of 83.78% and 99.79%, respectively. We note that even if a high FITC doublet could not be distinguished via image processing, its LCAR value would allow it to be assessed as the proper average of the two joined cells.

2.3.4 FIRE enhancements over flow cytometry

The images from FIRE make many approximate measurements in flow cytometry more explicit. In traditional flow cytometry, forward scatter (FSC) is commonly associated with the size of the particles measured, while side scatter (SSC) relates to the composition or complexity of the particle measured. However, previous work has found that FSC can be altered due to the refractive index of particles, particle composition, and machine design [36]. Therefore, even the use of calibration beads used to calibrate the FSC signals with true cell size may not be precise if the bead composition does not closely match that of the particles. These issues are eliminated by being able to process images of particles instead, i.e.

the use of FIRE imaging flow cytometry in our study. Additionally, measurements of FSC and SSC pulse width and height are used to distinguish cell doublets [37, 38]. This operates on the principle that two cells following immediately after each other may have pulses of the same height, but a width (or time of flight) that is twice as long as a normal cell. The use of time of flight to identify cell doublets breaks down unless the cells are oriented in the direction of flow and maintain the same pulse width of a single cell. As we show in Figure 2.2b, there is a normal range of *E. gracilis* lengths, so single cells may have similar pulse heights, but different pulse widths. Most *E. gracilis* doublets can be discriminated using images unless the two cells perfectly overlap with identical shapes. Finally, we show here the utility of normalizing fluorescence by cell size, as well as fluorescent structure size by cell size (Figure 2.3). The latter cannot be achieved with traditional flow cytometry, and the former cannot be wholly trusted if the cell measurements derived from FSC are imprecise.

E. gracilis cells are generally aligned with flow, especially longer cells. Exact orientations in the xy plane (i.e. the plane perpendicular to the laser beam) don't impact imaging unless orientation drastically alters cell linear velocity or rotation. We believe the sheath flow in the flow cell helps orient the cells, and we have previously demonstrated that longer cells are more likely to be aligned with flow, and that increasing Reynolds numbers helps to aligns shorter cells [39]. Cells non-parallel to the xy plane can reduce image quality for both brightfield and fluorescence images, especially for cells significantly outside the depth of focus of the objective. The ability to see the out-of-focus components in the brightfield channel, and discount fluorescence values may not be possible in traditional point-based flow cytometry. The ability to discern out-of-focus components of lower aspect cells is more difficult than with longer cells. Even if a shorter cell stays within the objective depth of focus, a partially rotated cell in the z-direction (i.e. the laser beam direction) can obscure the fluorescence images due to overlapping structures.

2.3.5 Investigating cell heterogeneity

The cell heterogeneity witnessed here can be further investigated to understand the underlying causes. Variations in *E. gracilis* metabolite contents can be attributed to temporary environmental conditions, or mutations within the cell population. Beyond the chloroplast content and cell morphology investigated here, we expect that additional FIRE fluorescent channels can be utilized to assess stigma carotenoid content or the cytoskeleton, which may indicate the cells' ability to react to, and respond to light. Understanding the exact conditions that a subset of cells experience during culturing may prove to be more difficult. But this could be studied by simulating cell populations with environmental conditions that represent the periphery of a bioreactor that experiences maximal light, and that of the center with reduced light. No single cell likely spends its time in only one of these settings, but this can help characterize responses in these two extremes. Candidate *E. gracilis* cells can be isolated by integration with downstream active sorting techniques such as acoustics [40], and pulsed lasers [41], which can sort cells at rates between 7,000-23,000 per second. A method utilizing external membrane pumps has been demonstrated with *E. gracilis*, and achieved a sort rate of 23,000 cells per second [42]. Integrating any of these methods will be dependent on image processing time, spacing of adjacent cells, cell velocity, and any effects due to the cells' non-circular shape.

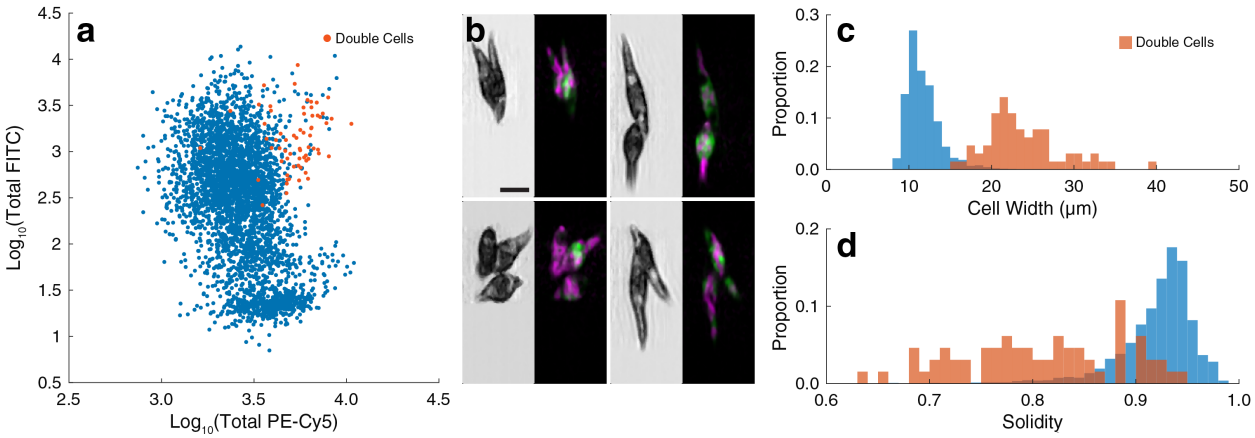

Figure 2.4: **High FITC cells include doublet populations.** (**a**) Selecting for high FITC (529/28 nm) values in this sample of heterotrophically cultured *E. gracilis* under fermentation for 3 days can include double cells (orange). (**b**) These doublets can be clearly distinguished in FIRE images. Scale bar = 20 µm . (**c**) Double cell images can be excluded based on morphology metrics including cell area, width, or (**d**) solidity.

2.4 Conclusion

In this work, we performed quantitative analysis of the chemo-morphological heterogeneity at the single-cell level within *E. gracilis* cell populations using a fluorescence imaging flow cytometric technique. Using FIRE, high-throughput, multi-parameter, and high-content imaging of each cell simultaneously in brightfield, and two fluorescence channels (FITC and PE-Cy5) enables the assembly of a morphological atlas of cells under different environmental conditions. The cell-to-cell variations of both morphology and intracellular molecular organization (lipid droplets and chloroplasts) allowed isolation of metrics that may be better correlated to lipid productivity per biomass at the single-cell level. The additional phenotypic information provided by fluorescence imaging makes this approach more informative than a bulk measurement or conventional flow cytometry, and much higher throughput than static microscopic techniques. This approach will ultimately allow for a better understanding of microalgal heterogeneity and potential underlying mechanisms of response to environmental

cues, and bifurcation of response at the subpopulation level.

Although LCAR measurements are correlated with FITC values at the single-cell level, and with bulk lipid measurements at a population level, the impact of these new metrics can best be validated by direct measurements of lipid per biomass for individual cells. By combining with active cell sorting based on the identified metrics, direct quantification at the single-cell level can be enabled. Sorting based on chemo-morphological states will ultimately enable the identification and isolation of microalgal mutants and rare cell populations with desirable phenotypes for biomass and biofuel production.

2.A Appendix

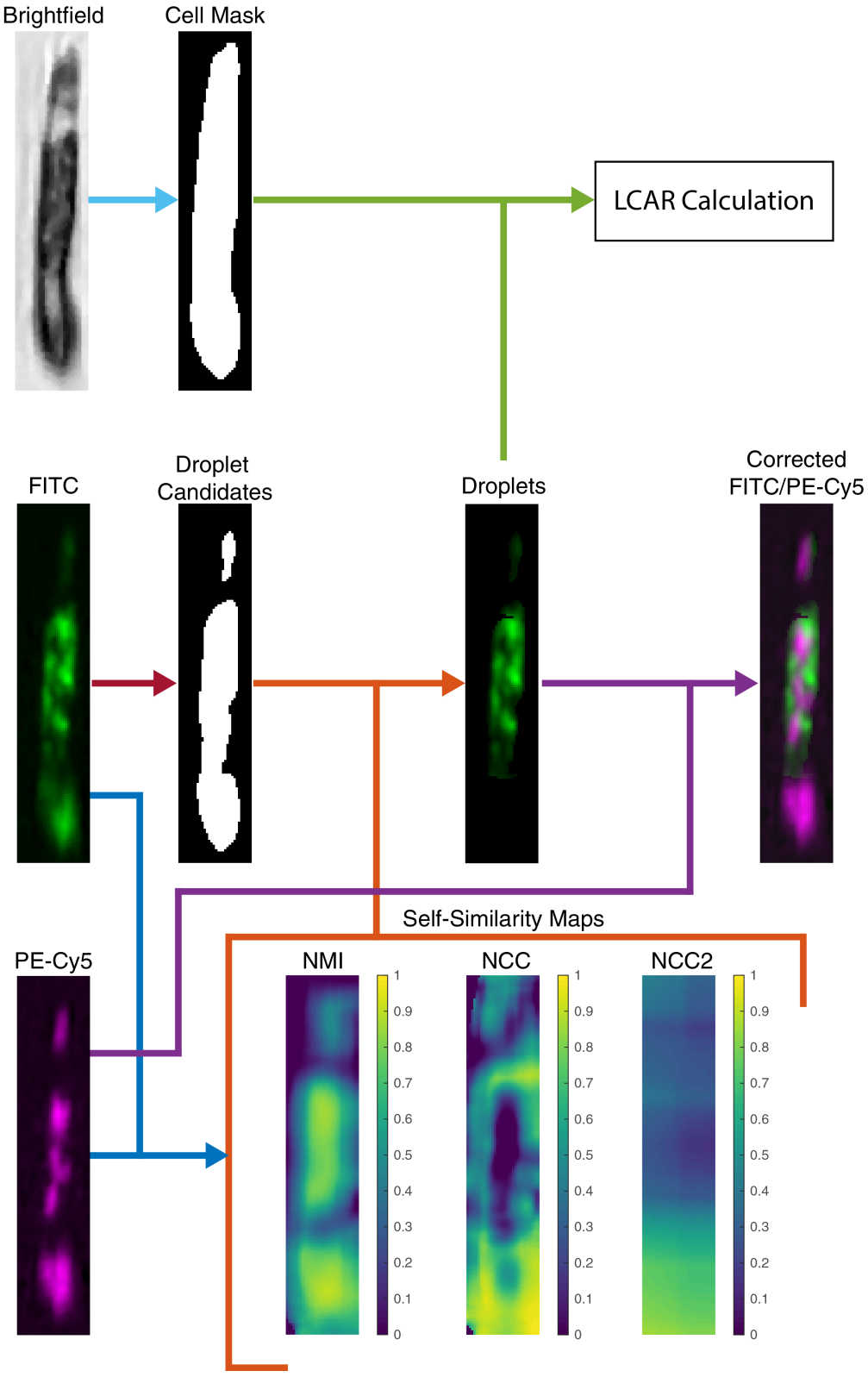
Brightfield
Cell Mask
LCAR Calculation
FITC
Droplet Candidates
Droplets
Corrected FITC/PE-Cy5
Self-Similarity Maps
PE-Cy5
NMI
NCC
NCC2
1
0.9
0.8
0.7
0.6
0.5
0.4
0.3
0.2
0.1
0

Figure 2.A.1: **Overview of image processing and analysis workflow.** FIRE imaging flow cytometric technique enables imaging of *E. gracilis* in flow in bright-field, PE-Cy5 (679/41 nm), and FITC (529/28 nm) channels. Brightfield images are used to locate the cell boundary and calculate morphological parameters. PE-Cy5 (magenta) captures chlorophyll auto-fluorescence, while FITC captures lipids stained with BODIPY$^{505/515}$ and part of the spectrum of chlorophyll auto-fluorescence. Structures in each channel may be spatially distinct, but spatial overlap in regions with high similarity in FITC and PE-Cy5 channels are attributed to chlorophyll auto-fluorescence. FITC images are used to detect lipid droplets via dynamic thresholding, and structures appearing in both fluorescence images are excluded from this detection. This is achieved by calculating normalized mutual information (NMI) and normalized cross-correlation (NCC) maps for both fluorescence channels. NMI measures mutual dependence between corresponding regions of FITC/PE-Cy5 images, and ranges from 0 to 1. NCC measures cross-correlation of pixel pairs between corresponding regions of FITC/PE-Cy5 images at a fine and rougher scale ($NCC2$), and ranges from -1 to 1. Values from these three self-similarity maps are combined and used to determine if a region exhibits high self-similarity, and should be excluded from the final lipid droplet detection. $ExcludedRegion = (NMI \geq 0.6275)$ && $(NCC \geq 0.51)$ && $(NCC2 \geq 0.2)$.

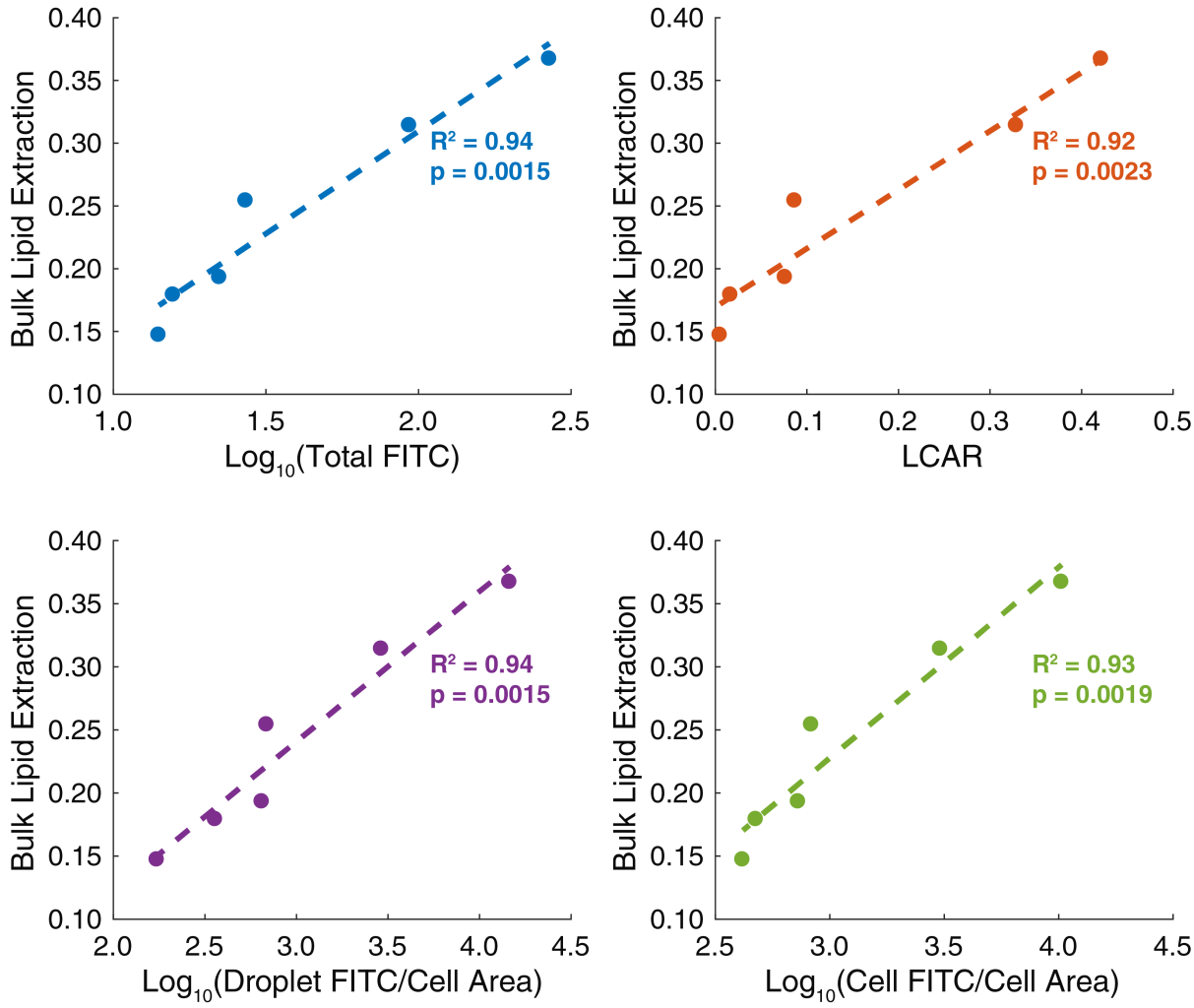

Figure 2.A.2: **Fluorescence intensity and image-based analysis of intracellular lipid content correlate well with bulk lipid measurements.** *E. gracilis* cells cultured in KH medium were treated for six different fermentation durations, 0 hours, 6 hours, 14 hours, 1 day, 2 days and 3 days. FIRE imaging flow cytometric analysis and gravimetric bulk measurements were performed and compared. Integrated FITC (529/28 nm) intensity is positively correlated with bulk lipid measurement with $R^2 = 0.94$, $p = 0.0015$. LCAR, which calculates the area of detected lipid droplets per cell area is also positively correlated with bulk lipid extraction ($R^2 = 0.92$, $p = 0.0023$). Normalizing lipid droplets FITC intensity by cell area ($R^2 = 0.94$, $p = 0.0015$), and normalizing cellular FITC intensity by cell area ($R^2 = 0.93$, $p = 0.0019$) are also closely, positively correlated with bulk lipid extraction.

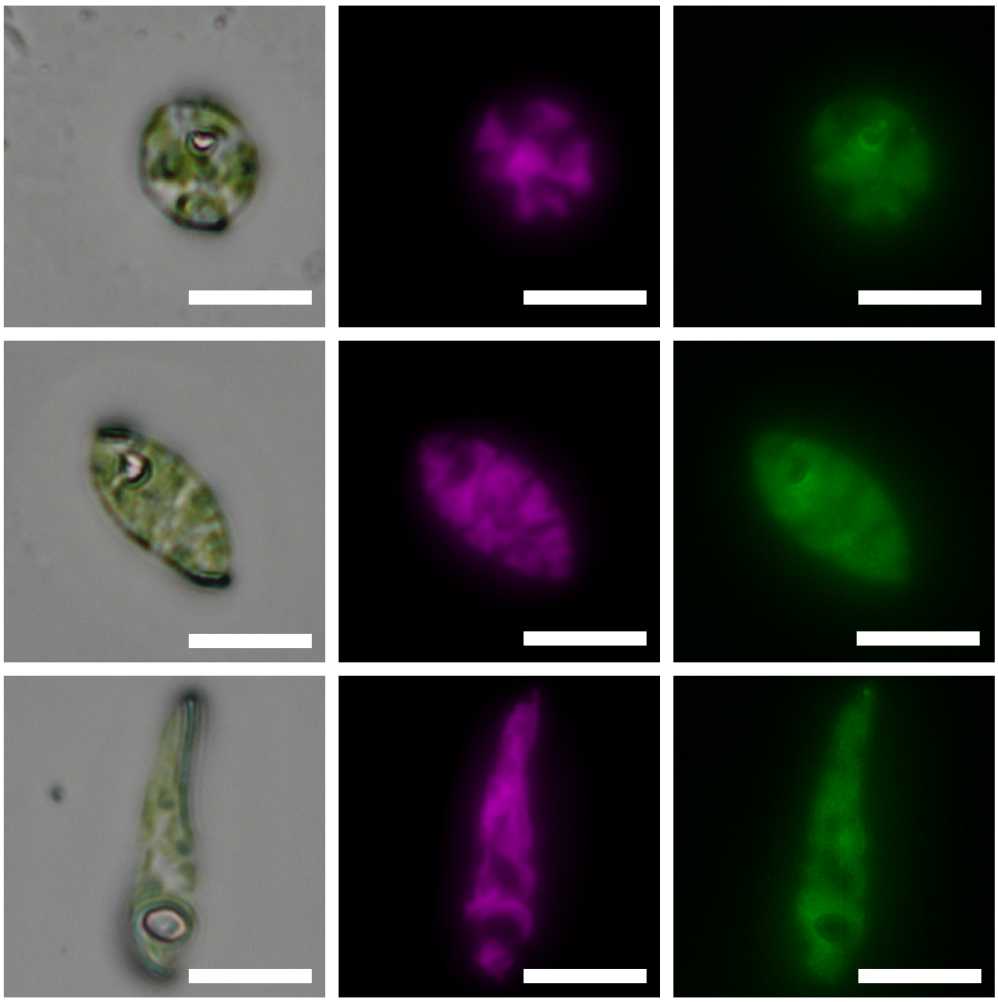

Figure 2.A.3: **The autofluorescence of pigments in chloroplasts in *E. gracilis*.** Chloroplast structures that contain high levels of green pigment in *E. gracilis* cells also show co-located autofluorescence in multiple channels when imaged with a fluorescence microscope. These structures are visible in the FITC channel (green) and Cy5 channels (magenta). FITC and Cy5 images are exposed for 6 s and 200 ms, respectively. Imaged with Nikon Ti-E microscope (20x/0.45 objective with 1.5x), Nikon DS-Fi3 camera (color image, 2.4 µm pixel pitch), and Photometrics Prime camera (fluorescence images, 6.5 µm pixel pitch). Scale bar = 20 µm .

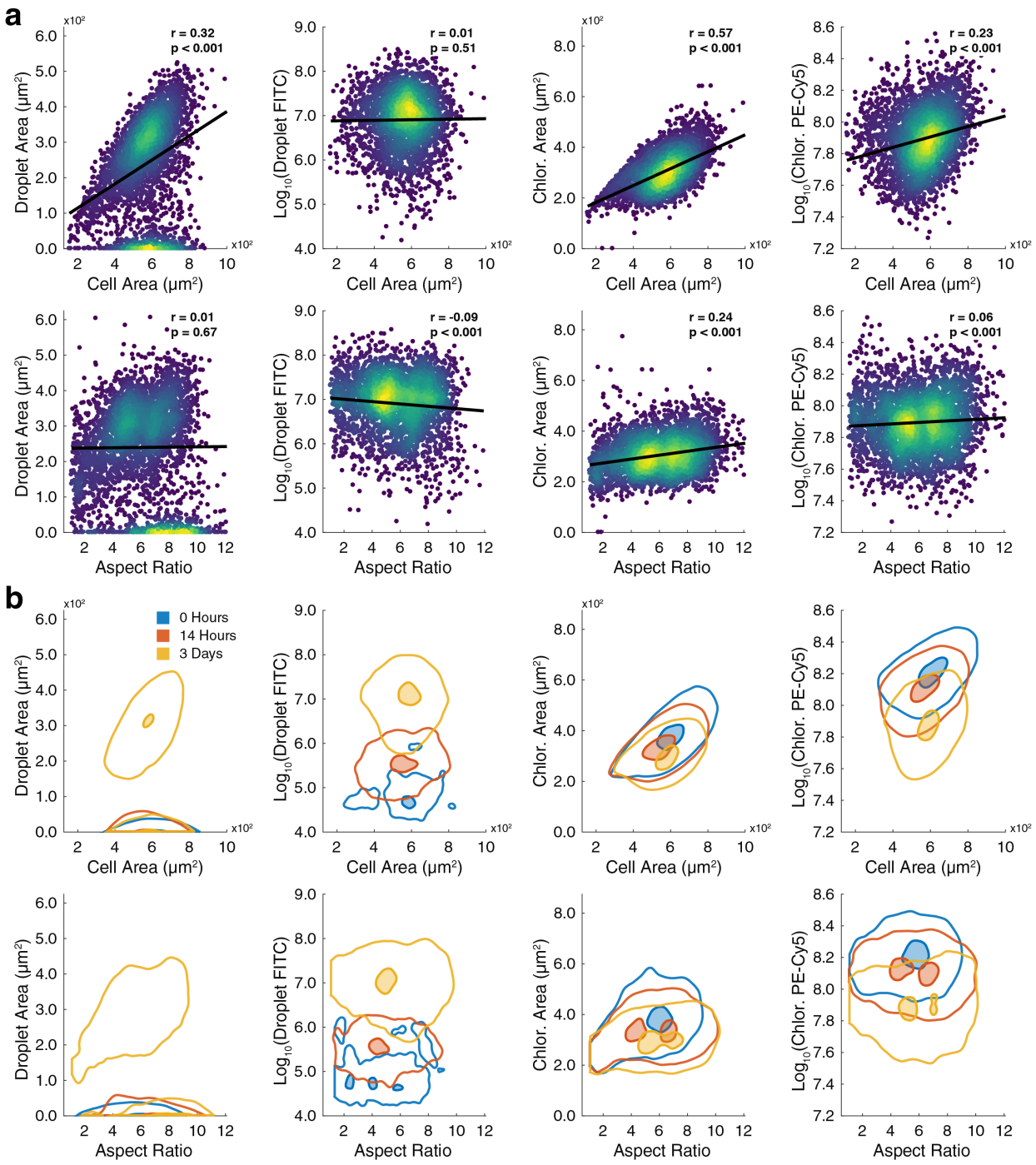

Figure 2.A.4: **Relationship of *E. gracilis* intracellular components with cell morphology.** (**a**) Density scatter plots of *E. gracilis* cultured in KH medium and fermented for 3 days. Least squares linear regression is calculated and shown with Pearson correlation coefficient p value. Cell area is positively, significantly correlated with lipid and chloroplast

areas, as well as chloroplast PE-Cy5 (679/41 nm) intensity. Cell aspect ratio has smaller, significant correlations with chloroplast area, and chloroplast and lipid fluorescence intensity. (**b**) Density contours for several fermentation times (0 hours, 14 hours, 3 days), are compared for the same morphology and intracellular component metrics. Contours and shaded regions indicate 80^{th} and 10^{th} percentiles of the estimated density, respectively. Cells fermented for 3 days have clear increased lipid droplet amounts and associated FITC intensity. All days have conserved distributions and trends with chloroplast area, but cells show a negative relationship between fermentation time and chlorophyll PE-Cy5 fluorescence, in addition to an altered distribution shape for cell area at 3 days.

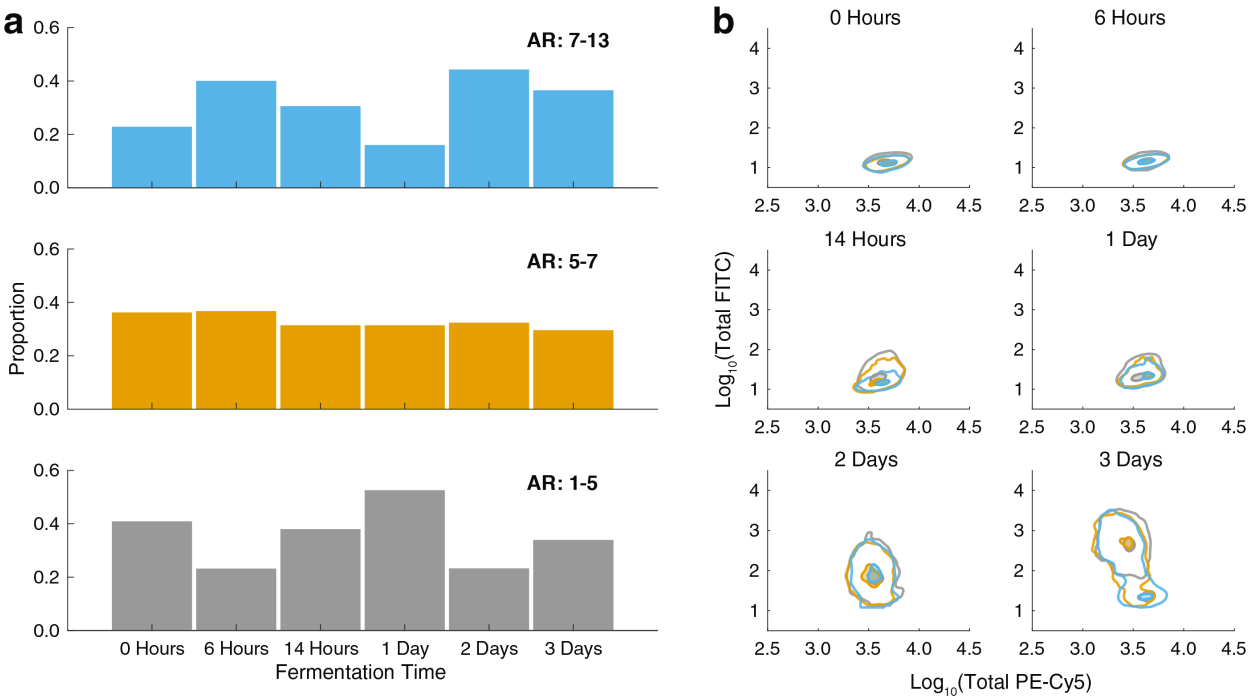

Figure 2.A.5: ***E. gracilis* aspect ratio (AR) has no strong relationship with fermentation time or fluorescence intensity.** *E. gracilis* cells cultured in KH medium were treated for six different fermentation durations, 0 hours, 6 hours, 14 hours, 1 day, 2 days and 3 days. (**a**) Cells imaged with FIRE were divided into three groups based on AR: 1–5, 5–7, and 7–13. There is no discernable relationship between these groups and fermentation time. (**b**) Density contours of total FITC (529/28 nm) and PE-Cy5 (679/41 nm) fluorescence intensity binned by these three AR groups are not distinctly different, except at 14 hours, when AR 7–13 cells have a lower range of FITC intensity. Contours and shaded regions indicate 80^{th} and 10^{th} percentiles of the estimated density, respectively.

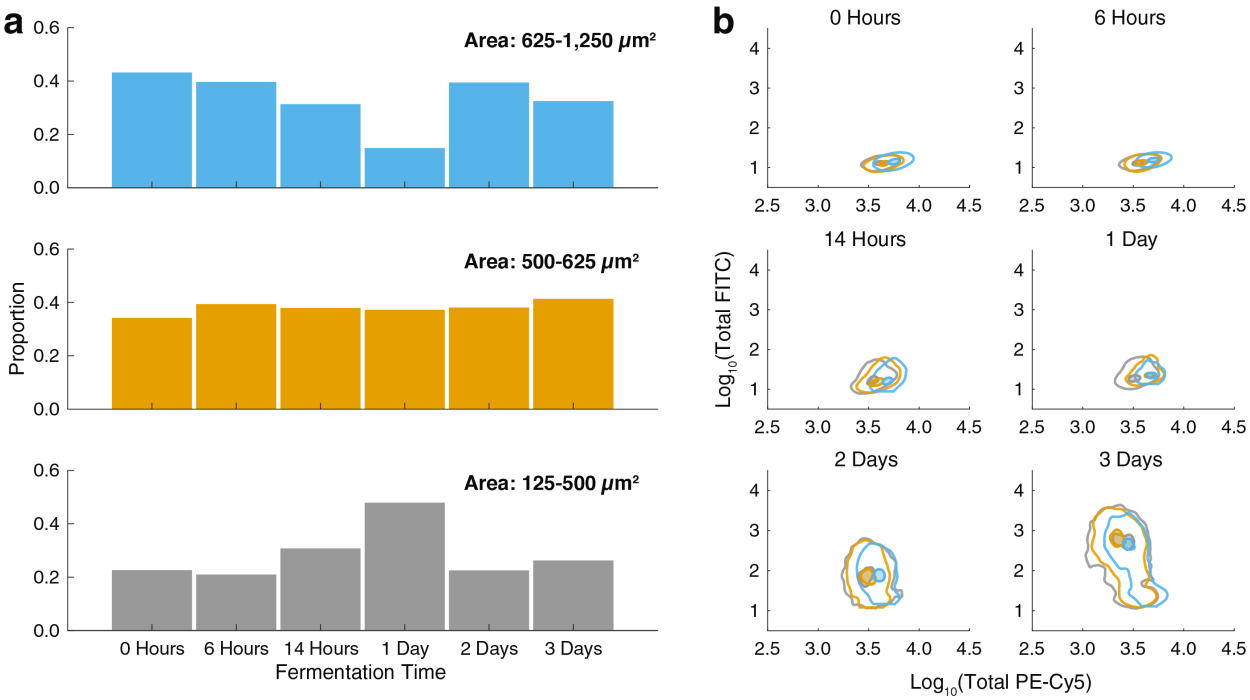

Figure 2.A.6: ***E. gracilis* area shows some relationship with fermentation time and fluorescence intensity.** *E. gracilis* cells cultured in KH medium were treated for six different fermentation durations, 0 hours, 6 hours, 14 hours, 1 day, 2 days and 3 days. (**a**) Cells imaged with FIRE were divided into three groups based on cell area: 125-500, 500-625, and 625-1,250 μm^2. During the first 24 hours of fermentation, there is a trend towards an increased proportion of smaller cells. (**b**) Density contours of total FITC (529/28 nm) and PE-Cy5 (679/41 nm) fluorescence intensity, when binned in these three area groups show a positive trend between cell area and PE-Cy5 fluorescence, which is consistently observed with cells 625-1,250 μm^2. Contours and shaded regions indicate 80$^{\text{th}}$ and 10$^{\text{th}}$ percentiles of the estimated density, respectively.

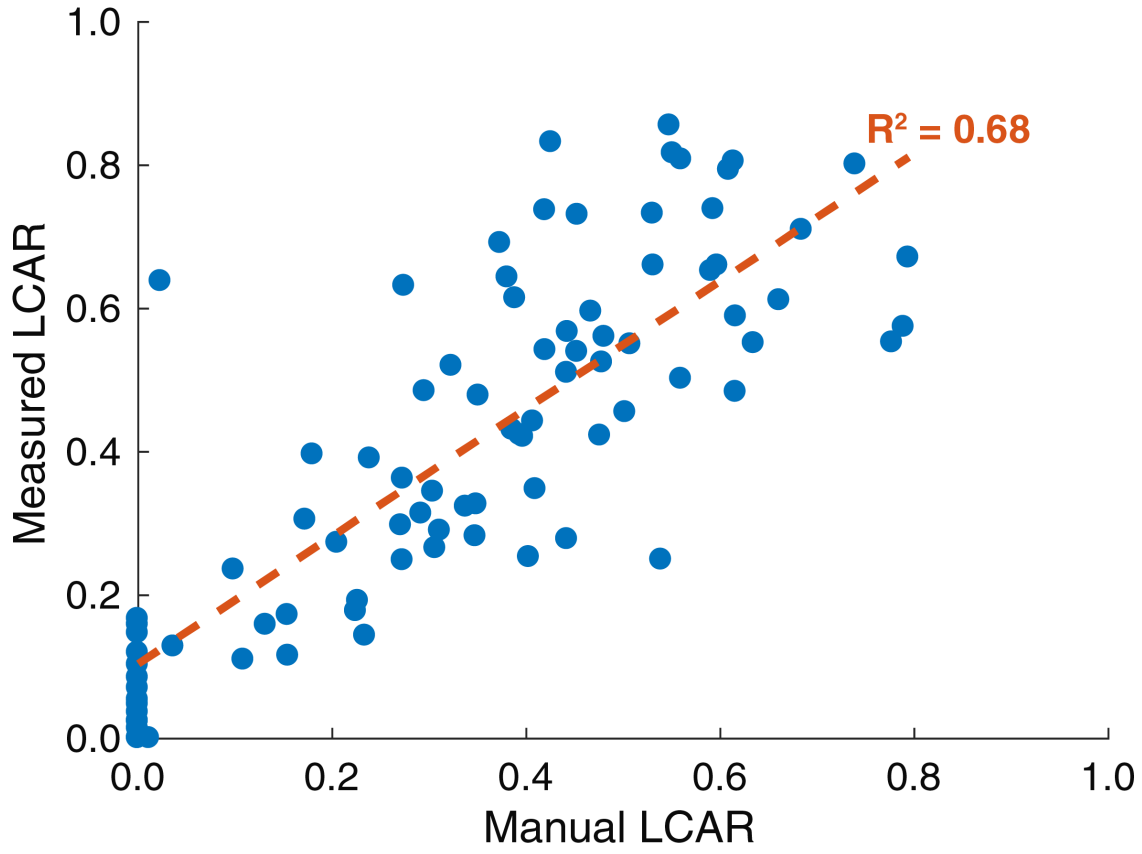

Figure 2.A.7: **Automated calculation of lipid to cell area ratio (LCAR) of *E. gracilis* is positively correlated with manually measured LCAR.** 88 cells were selected from a culture grown in KH medium and fermented for 2 days, across a range of LCAR. Cells and lipid droplets were segmented manually using MIPAV software. Least squares linear regression was performed with manual and automatic LCAR values, resulting in a line with equation $y = 0.8904x + 0.1043$ ($R^2 = 0.68$, $p < 0.001$). Our automatic method has a slight bias to overestimate LCAR as indicated by the y-intercept, especially at low values of LCAR.

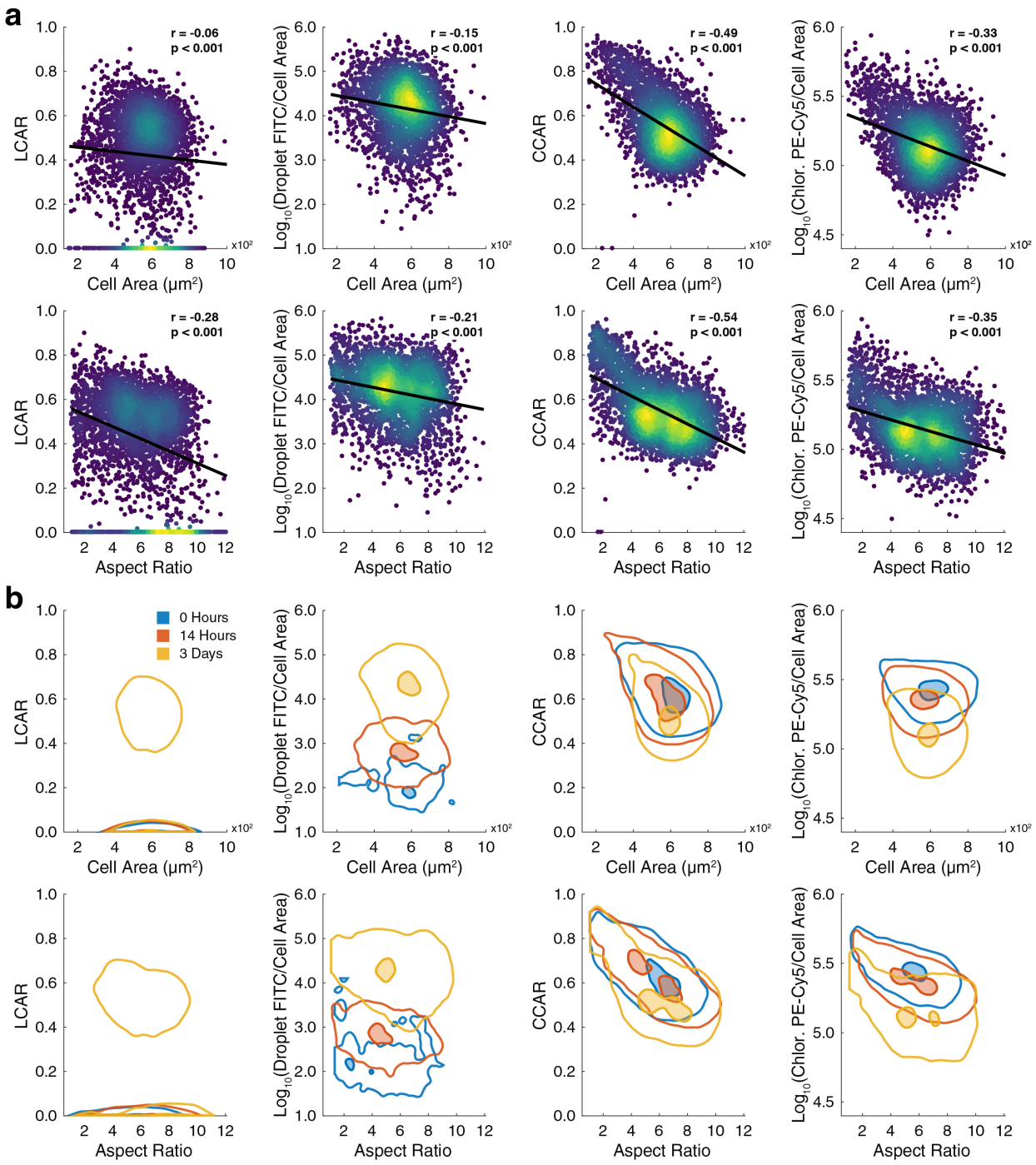

Figure 2.A.8: **Normalized intracellular component measurements of *E. gracilis* reveal new relationships with morphology parameters.** (**a**) Density scatter plots of *E. gracilis* cultured in KH medium and fermented for 3 days. Previous intracellular measurements are normalized by cell area to yield lipid to cell area ratio (LCAR), lipid FITC

per cell area (529/28 nm), chloroplast to cell area ratio (CCAR), and chloroplast PE-Cy5 per cell area (679/41 nm). Least squares linear regression is calculated and shown with Pearson correlation coefficient p value. Normalization reduces the correlation of cell area with lipid measurements, while revealing new negative correlations with chloroplast measurements. The same negative chloroplast trends are also now seen with cell aspect ratio measurements. (**b**) Density contours for several fermentation times (0 hours, 14 hours, 3 days), are compared for the same morphology and intracellular component metrics. Contours and shaded regions indicate 80^{th} and 10^{th} percentiles of the estimated density, respectively. Cells fermented for 3 days have clear increased LCAR levels and associated normalized FITC intensity. All days have conserved distributions and trends with CCAR, but cells show a negative relationship between fermentation time and chlorophyll PE-Cy5 fluorescence, in addition to an altered distribution shape for cell area at 3 days. These plots reveal a subpopulation of small, round cells that are extremely dense with chlorophyll content.

Bibliography

[1] Jeffrey W. Moody, Christopher M. McGinty, and Jason C. Quinn. Global evaluation of biofuel potential from microalgae. *Proceedings of the National Academy of Sciences of the United States of America*, 111(23):8691–8696, Jun 2014.

[2] Matthew C. Posewitz. Algal oil productivity gets a fat bonus, Jul 2017.

[3] Peer M. Schenk, Skye R. Thomas-Hall, Evan Stephens, Ute C. Marx, Jan H. Mussgnug, Clemens Posten, Olaf Kruse, and Ben Hankamer. Second Generation Biofuels: High-Efficiency Microalgae for Biodiesel Production. *BioEnergy Research*, 1(1):20–43, Marc 2008.

[4] Timothy Searchinger, Ralph Heimlich, R. A. Houghton, Fengxia Dong, Amani Elobeid, Jacinto Fabiosa, Simla Tokgoz, Dermot Hayes, and Tun Hsiang Yu. Use of U.S. croplands for biofuels increases greenhouse gases through emissions from land-use change. *Science*, 319(5867):1238–1240, Feb 2008.

[5] Keri B. Cantrell, Thomas Ducey, Kyoung S. Ro, and Patrick G. Hunt. Livestock waste-to-bioenergy generation opportunities, Nov 2008.

[6] Stuart A. Scott, Matthew P. Davey, John S. Dennis, Irmtraud Horst, Christopher J. Howe, David J. Lea-Smith, and Alison G. Smith. Biodiesel from algae: Challenges and prospects. *Current Opinion in Biotechnology*, 21(3):277–286, Jun 2010.

[7] Otto Pulz and Wolfgang Gross. Valuable products from biotechnology of microalgae, Nov 2004.

[8] Pauline Spolaore, Claire Joannis-Cassan, Elie Duran, and Arsène Isambert. Commercial applications of microalgae. *Journal of Bioscience and Bioengineering*, 101(2):87–96, Feb 2006.

[9] Takeshi Furuhashi, Takumi Ogawa, Rai Nakai, Masami Nakazawa, Atsushi Okazawa, Adchara Padermschoke, Kazuki Nishio, Masami Yokota Hirai, Masanori Arita, and Daisaku Ohta. Wax ester and lipophilic compound profiling of Euglena gracilis by gas chromatography-mass spectrometry: toward understanding of wax ester fermentation under hypoxia. *Metabolomics*, 11(1):175–183, Jun 2014.

[10] Ashagrie Aemiro, Shota Watanabe, Kengo Suzuki, Masaaki Hanada, Kazutaka Umetsu, and Takehiro Nishida. Effects of Euglena (Euglena gracilis) supplemented to diet (forage: Concentrate ratios of 60:40) on the basic ruminal fermentation and methane emissions in in vitro condition. *Animal Feed Science and Technology*, 212:129–135, Feb 2016.

[11] Haruko Takeyama, Akihisa Kanamaru, Yuko Yoshino, Hiroyuki Kakuta, Yoshiya Kawamura, and Tadashi Matsunaga. Production of antioxidant vitamins, β-carotene, vitamin C, and vitamin E, by two-step culture of Euglena gracilis Z. *Biotechnology and Bioengineering*, 53(2):185–190, Jan 1997.

[12] Thomas A Lonergan. Regulation of cell shape in Euglena gracilis. I. Involvement of the Biological Clock, Respiration, Photosynthesis, and Cytoskeleton. *Journal of Plant Physiology*, 71:719–730, 1983.

[13] Thomas A Lonergan. Regulation of cell shape in Euglena gracilis. II. The Effects of Altered Extra- and Intracellular Ca2+ Concentrations and the Effect of Calmodulin Antagonists. *Journal of Cell Science*, 50:37–50, 1984.

[14] J.M. Murray. Control of cell shape by calcium in the euglenophyceae. *Journal of Cell Science*, 49(1), 1981.

[15] J. J. Blum and N. Bégin-Heick. Metabolic changes during phosphate deprivation in euglena in air and in oxygen. *The Biochemical journal*, 105(2):821–829, Nov 1967.

[16] L. W. Coleman, Barry H. Rosen, and Steven D. Schwartzbach. Environmental Control of Carbohydrate and Lipid Synthesis in Euglena. *Plant and Cell Physiology*, 29(3):423–432, Apr 1988.

[17] J. S. Bunt. Analysis of algal pigments by thin-layer chromatography. *Nature*, 203(4951):1261–1263, Sep 1964.

[18] Paul B. Fayad, Audrey Roy-Lachapelle, Sung Vo Duy, Michèle Prévost, and Sébastien Sauvé. On-line solid-phase extraction coupled to liquid chromatography tandem mass spectrometry for the analysis of cyanotoxins in algal blooms. *Toxicon*, 108:167–175, Dec 2015.

[19] Takeshi Furuhashi and Wolfram Weckwerth. Introduction to Lipid (FAME) Analysis in Algae Using Gas Chromatography-Mass Spectrometry. In *The Handbook of Plant Metabolomics*, pages 215–225. Wiley-VCH Verlag GmbH & Co. KGaA, Weinheim, Germany, Apr 2013.

[20] Pawel L. Urban, Thomas Schmid, Andrea Amantonico, and Renato Zenobi. Multidimensional analysis of single algal cells by integrating microspectroscopy with mass spectrometry. *Analytical Chemistry*, 83(5):1843–1849, Marc 2011.

[21] Mark Scott Cooper, William Robert Hardin, Timothy Wayne Petersen, and Rose Ann Cattolico. Visualizing "green oil" in live algal cells. *Journal of Bioscience and Bioengineering*, 109(2):198–201, Feb 2010.

[22] Yoshifumi Wakisaka, Yuta Suzuki, Osamu Iwata, Ayaka Nakashima, Takuro Ito, Misa Hirose, Ryota Domon, Mai Sugawara, Norimichi Tsumura, Hiroshi Watarai, Tomoyoshi Shimobaba, Kengo Suzuki, Keisuke Goda, and Yasuyuki Ozeki. Probing the metabolic heterogeneity of live Euglena gracilis with stimulated Raman scattering microscopy. *Nature Microbiology*, 1(10):1–4, Aug 2016.

[23] Huawen Wu, Joanne V. Volponi, Ann E. Oliver, Atul N. Parikh, Blake A. Simmons, and Seema Singh. In vivo lipidomics using single-cell Raman spectroscopy. *Proceedings of the National Academy of Sciences of the United States of America*, 108(9):3809–3814, Marc 2011.

[24] P. Hyka, S. Lickova, P. Přibyl, K. Melzoch, and K. Kovar. Flow cytometry for the development of biotechnological processes with microalgae, Jan 2013.

[25] Koji Yamada, Hideyuki Suzuki, Takuto Takeuchi, Yusuke Kazama, Sharbanee Mitra, Tomoko Abe, Keisuke Goda, Kengo Suzuki, and Osamu Iwata. Efficient selective breeding of live oil-rich Euglena gracilis with fluorescence-activated cell sorting. *Scientific Reports*, 6(1):1–8, May 2016.

[26] Baoshan Guo, Cheng Lei, Takuro Ito, Yiyue Jiang, Yasuyuki Ozeki, and Keisuke Goda. High-Throughput Accurate Single-Cell Screening of Euglena gracilis with Fluorescence-Assisted Optofluidic Time-Stretch Microscopy. *PLOS ONE*, 11(11):e0166214, Nov 2016.

[27] Eric D Diebold, Brandon W Buckley, Daniel R Gossett, and Bahram Jalali. Digitally synthesized beat frequency multiplexing for sub-millisecond fluorescence microscopy. *Nature Photonics*, 7(10):806–810, Sep 2013.

[28] Keisuke Goda, Ali Ayazi, Daniel R. Gossett, Jagannath Sadasivam, Cejo K. Lonappan, Elodie Sollier, Ali M. Fard, Soojung Claire Hur, Jost Adam, Coleman Murray, Chao Wang, Nora Brackbill, Dino Di Carlo, and Bahram Jalali. High-throughput single-microparticle imaging flow analyzer. *Proceedings of the National Academy of Sciences of the United States of America*, 109(29):11630–11635, Jul 2012.

[29] Jeanette S. Brown. Absorption and fluorescence spectra of chlorophyll-proteins isolated from Euglena gracilis. *BBA - Bioenergetics*, 591(1):9–21, Jun 1980.

[30] Francis X. Cunningham and Jerome A. Schiff. Chlorophyll-Protein Complexes from Euglena gracilis and Mutants Deficient in Chlorophyll b . *Plant Physiology*, 80(1):223–230, Jan 1986.

[31] C. Studholme, D. L.G. Hill, and D. J. Hawkes. An overlap invariant entropy measure of 3D medical image alignment. *Pattern Recognition*, 32(1):71–86, Jan 1999.

[32] JP Lewis. Fast Normalized Cross-Correlation. In *Vision Interface*, pages 120–123, 1995.

[33] L. E. Koren and S. H. Hutner. High yield media for photosynthesizing euglena gracilis abstract. *Journal of Protozoology*, 14(Suppl.):17, Nov 1967.

[34] A. L. Ayers and J. J. Dooley. Laboratory extraction of cottonseed with various petroleum hydrocarbons. *Journal of the American Oil Chemists' Society*, 25(10):372–379, 1948.

[35] Hiroshi Inui, Kazutaka Miyatake, Yoshihisa Nakano, and Shozaburo Kitaoka. Wax ester fermentation in Euglena gracilis. *FEBS Letters*, 150(1):89–93, Dec 1982.

[36] Amit Tzur, Jodene K. Moore, Paul Jorgensen, Howard M. Shapiro, and Marc W. Kirschner. Optimizing Optical Flow Cytometry for Cell Volume-Based Sorting and Analysis. *PLoS ONE*, 6(1):e16053, Jan 2011.

[37] Naotsugu Haraguchi, Masahisa Ohkuma, Hiroyuki Sakashita, Shinji Matsuzaki, Fumiaki Tanaka, Koshi Mimori, Yukio Kamohara, Hiroshi Inoue, and Masaki Mori. CD133+CD44+ population efficiently enriches colon cancer initiating cells. *Annals of Surgical Oncology*, 15(10):2927–2933, Oct 2008.

[38] Howard M. (Howard Maurice) Shapiro. *Practical flow cytometry*. Wiley-Liss, 2003.

[39] M. Li, H. E. Muñoz, A. Schmidt, B. Guo, C. Lei, K. Goda, and D. Di Carlo. Inertial focusing of ellipsoidal Euglena gracilis cells in a stepped microchannel. *Lab on a Chip*, 16(22):4458–4465, Nov 2016.

[40] Liqiang Ren, Yuchao Chen, Peng Li, Zhangming Mao, Po Hsun Huang, Joseph Rufo, Feng Guo, Lin Wang, J. Philip McCoy, Stewart J. Levine, and Tony Jun Huang. A high-throughput acoustic cell sorter. *Lab on a Chip*, 15(19):3870–3879, Aug 2015.

[41] Yue Chen, Aram J. Chung, Ting-Hsiang Wu, Michael A. Teitell, Dino Di Carlo, and Pei-Yu Chiou. Pulsed Laser Activated Cell Sorting with Three Dimensional Sheathless Inertial Focusing. *Small*, 10(9):1746–1751, May 2014.

[42] Shinya Sakuma, Yusuke Kasai, Takeshi Hayakawa, and Fumihito Arai. On-chip cell sorting by high-speed local-flow control using dual membrane pumps. *Lab on a Chip*, 17(16):2760–2767, Aug 2017.

CHAPTER 3

Fractal-LAMP: Label-free analysis of fractal precipitate for digital loop-mediated isothermal nucleic acid amplification

3.1 Introduction

The detection of nucleic acids is widely used in the diagnosis of disease, including identifying mutations in tumors [1, 2] or microbial and viral pathogens obtained from patient samples [3]. Nucleic acid detection has also become vital in assessing food and water quality by detecting pathogens, allergens, or genetic identity of food [4]. Ongoing research is aimed at detecting nucleic acids, such as DNA and RNA, at lower concentrations, more cheaply, or in a more portable, accessible manner [5].

Innovations in nucleic analysis include approaches to isolate and amplify target DNA, quantify the amount of target, as well as instrumentation to detect the isolated/amplified targets. When target DNA is present at sufficiently low concentrations, it must first be amplified by any number of methods including polymerase chain reaction (PCR) [6], rolling circle amplification [7], or loop-mediated isothermal amplification (LAMP) [8]. Once the target DNA has been sufficiently amplified, its presence is often measured using fluorescent dyes, whose intensity is correlated to the amount of DNA present, or through electrical signals [9, 10, 11]. Improved quantification and limits of detection can be achieved by partitioning the sample into micro-compartments, each independently amplified and read [12], i.e. digital nucleic acid amplification. Finally, readout instruments that leverage low-cost consumer electronic devices can lower costs and increase portability of these assays [13, 14, 15].

LAMP is an attractive method of amplifying DNA for its thermal simplicity and speed. Unlike some other DNA amplification methods, LAMP proceeds at a single temperature, simplifying the equipment needed to run it. It can also create a large quantity of amplified DNA on short timescales, with more than 50 times more product than PCR at comparable scales [16]. While many DNA amplification tests use fluorescent dyes directly on the main product, LAMP progress can be assessed by one of its byproducts. During the LAMP reaction, pyrophosphate forms as a byproduct and can precipitate with magnesium ions in solution to form magnesium pyrophosphate (Figure 3.1a) increasing solution turbidity as a function of DNA amplification [17, 18]. Solution turbidity has been shown to be a valid indicator for DNA amplification with LAMP and possesses particular advantages. In contrast one class of fluorescent dyes, intercalating dyes, which are usually incorporated into reaction solutions prior to reaction, has been shown to interfere with DNA reaction kinetics [19, 20, 21, 22], although there have been advances to counter this effect [23]. Previous work also showed that intercalating dyes can be variable and heat sensitive [23]. Other advantages of using intrinsic reaction products are that non-fluorescence measures such as turbidity in LAMP can avoid the need for extra dyes, fluorescence excitation and reading equipment, and improve amplification times.

Digitization of DNA amplification provides improved limits of detection and quantitative accuracy. DNA amplification has traditionally been carried out and measured in bulk solution. In that case, DNA content is correlated to a single analog measure describing the amplification in the bulk fluid. In a digital assay, the bulk solution is partitioned into many small volumes, such as wells or aqueous droplets [12]. Compartmentalization binarizes the initial readout, where the analog signal in each compartment can be thresholded to yield either a positive or negative event, which at sufficiently low DNA counts can be related to a single starting DNA molecule. Finally, the percentage of negative compartments is directly correlated to the original bulk concentration. Previous work has demonstrated this digital assay concept using LAMP whereby fluorescent intercalating dyes led to amplified compartment-specific fluorescent signals [24, 25, 23, 26, 27]. The use of the magnesium py-

rophosphate product of LAMP (Figure 3.1b) has not been used to our knowledge to detect amplified signal in a digital format.

Here we report Fractal-LAMP, a droplet-based method to perform label-free, digital DNA quantification. This is achieved by encapsulating target DNA samples and LAMP reaction mix in thousands of sub-nanoliter scale droplets. Following reaction, droplets with target DNA molecules accumulate magnesium pyrophosphate precipitate inside. This coalesced precipitate, with a unique fractal-like structure, is tens of microns in size and is clearly visible using brightfield imaging. We detect the precipitate with relatively low magnification brightfield microscopic imaging followed by image analysis with a customized computer vision algorithm. Utilizing partitioning statistics, the percentage of droplets containing precipitate is correlated with the original bulk DNA concentration, enabling automated detection of precipitate droplets and calculation of bulk DNA concentration. Combined with the reduced instrument complexity required for isothermal LAMP amplification, this new approach to digital detection of amplification should further reduce final instrument complexity and cost by employing cost-effective portable brightfield microscopy systems [14, 15].

3.2 Results

3.2.1 Overview

We have implemented a label-free, brightfield digital DNA amplification detection method using droplets. A droplet-based approach is preferred for Fractal-LAMP given that precipitate observed in wells after performing LAMP is not concentrated and may variably adhere to well walls (Figure 3.A.1). We hypothesize performing Fractal-LAMP in droplets promotes the accumulation of precipitate at a single point, due to droplet shape and reduced volume, further facilitating imaging and image analysis. Target DNA solution is combined with LAMP reaction mix and primers, and introduced into droplets using a 3D printed droplet generator. Droplets are heated to initiate the LAMP reaction and accumulate reaction products. Precipitate that accumulates within droplets that amplify target DNA is imaged and

analyzed, and compared to standard intercalating dye-based readout. We characterize how precipitate correlates with fluorescence at the single droplet level and how the number of droplets with precipitate correlates with overall differences in DNA target concentration. Finally, we develop image analysis tools based on a Bag of Visual Words (BOVW) [28] to identify precipitate in droplets in an automated fashion and report on our automated label-free results for predicting target DNA concentration.

Solutions of LAMP reaction mix, fluorescent nucleic acid intercalating dye, and target bacteriophage DNA were encapsulated in droplets via a 3D droplet generator [29] (Figure 3.1c) and incubated at 67℃ for 2 hours. After incubation, the droplets were transferred to a 120 µm slit chamber for brightfield and fluorescence imaging at 10× magnification (Figure 3.1d). Multiple fields of view across multiple sample chambers were imaged for each DNA concentration (5.7×10^1 copies DNA $\cdot$ µL^{-1}, 5.7×10^2 copies DNA $\cdot$ µL^{-1}, 5.7×10^3 copies DNA $\cdot$ µL^{-1}, 5.7×10^4 copies DNA $\cdot$ µL^{-1}, and 5.7×10^5 copies DNA $\cdot$ µL^{-1}). Droplets with coalesced magnesium pyrophosphate are also positive with the nucleic acid intercalating dye. The precipitate aggregates into clumps that are typically found in the center of droplets. Imaged droplets with diameters 65 – 96 µm (76.9 $\pm$ 6.9 µm) are detected and extracted from both brightfield and fluorescence images using a custom MATLAB script. 30,138 droplet images are extracted in total, with at least 2,700 droplets from each DNA concentration. Each droplet image is manually inspected to determine the presence of precipitate.

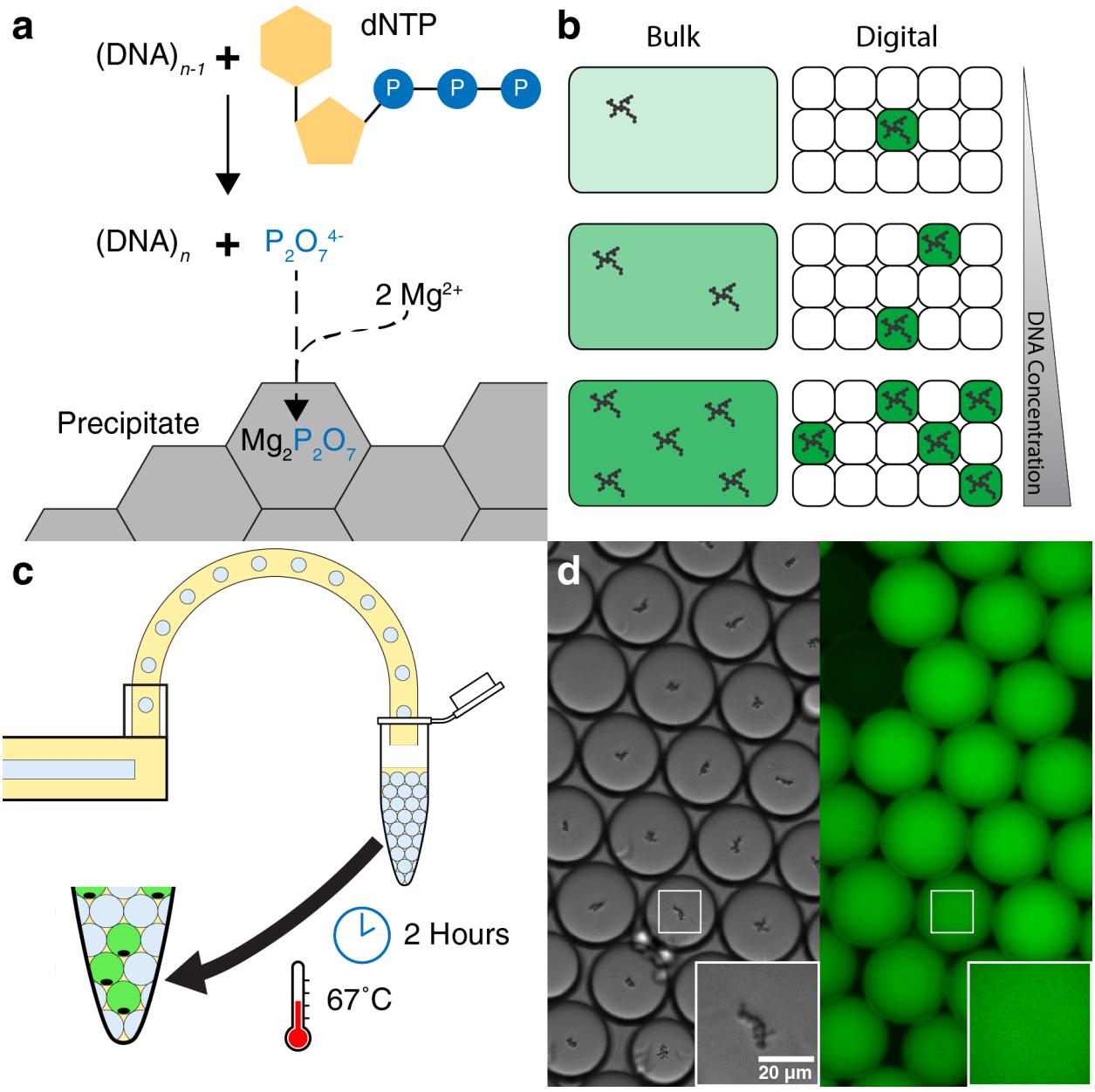

Figure 3.1: **Fractal-LAMP: Detection of DNA via LAMP byproducts in droplets imaged using brightfield microscopy.** (**a**) During DNA amplification by DNA polymerase, pyrophosphate (blue) is cleaved from the deoxynucleotide (dNTP) as a byproduct. Pyrophosphate reacts with magnesium ions in the LAMP solution mix, and precipitates at sufficiently high concentrations. (**b**) DNA amplification can be assessed via fluorescent dyes, or by turbidity in the case of LAMP. In bulk solution, the fluorescence or turbidity increases with DNA concentration, but may be difficult to discern at low concentrations or

across small differences in concentration. Compartmentalization of volume creates a digital readout, where fractal-like precipitate or fluorescence are not diluted by a large volume. The percentage of negative compartments are directly correlated to compartment size and the original bulk concentration. (**c**) LAMP reaction mix and DNA are compartmentalized with a 3D printed droplet generator and are incubated at 67℃ for 2 hours before imaging. (**d**) After incubation, the droplets are transferred to a 120 µm slit chamber for brightfield and fluorescence imaging. Magnesium pyrophosphate precipitate is visible in brightfield and corresponds to droplets with increased fluorescent intercalating dye signal.

3.2.2 Characterization of precipitate in droplets

We find that the presence of magnesium pyrophosphate precipitate is correlated with nucleic acid intercalating dye fluorescence in a droplet. The presence of precipitate in a droplet is compared with the integrated fluorescence of the droplet in corresponding fluorescence images. The precipitate-positive droplets (n = 5,390, Mdn = 5.25, SD = 1.44), have a clear increase in fluorescence over precipitate-negative droplets (n = 19,399, Mdn = 2.33, SD = 0.65) (Figure 3.2a). A point-biserial correlation is used to determine the relationship between fluorescence and precipitate presence. There is a positive correlation between fluorescence and precipitate, which is statistically significant ($r_{pb} = 0.81$, n = 24,789, $p < 0.001$).

Precipitate presence in droplets is correlated to bulk target DNA concentration. As bulk DNA concentration increases, the percentage of empty droplets decreases (Figure 3.2b). Partitioning of original target DNA in droplets is governed by the binomial and Poisson distributions [12]. As a result, the average number of target DNA molecules per droplet, λ is defined as $\lambda = Conc_{DNA} \cdot Vol_{drop}$, where $Conc_{DNA}$ is the bulk DNA concentration, and Vol_{drop} is the droplet volume. λ can also be related to the percentage of droplets (E), through the relationship $\lambda = -\ln(E)$. The extent to which our observed λ values deviate from the ideal λ for each DNA concentration is defined as the inefficiency factor ω ($\lambda_{ideal} = \omega \cdot \lambda_{observed}$) and is determined with hierarchical Bayesian inference [30]. The posterior of ω (median=127.14, 99% CI [121.81, 132.65]) indicates that there is a ∼127x inefficiency with

either partitioning the DNA molecules, or the LAMP reaction (Figure 3.2c). Nonetheless, there is a clear linear relationship between our measured λ values, based on counting droplets positive for precipitate, and DNA concentration. Despite deviations in observed λ from the regression, moderately informed priors in the Bayesian inference can produce 99% Highest Posterior Density (HPD) intervals that intersect the regression confidence band.

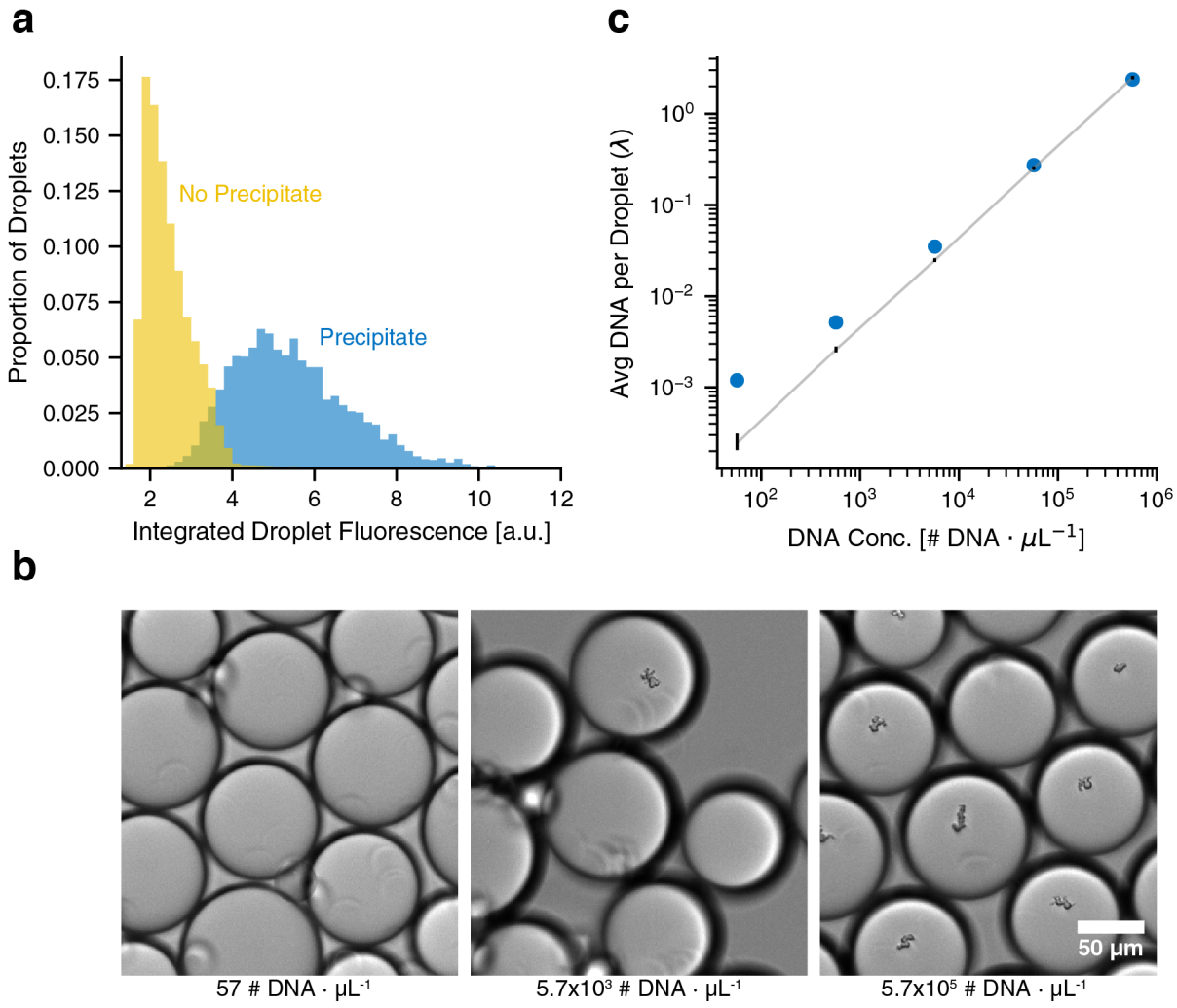

Figure 3.2: **The presence of precipitate in LAMP droplets is correlated to the integrated droplet fluorescence and the bulk DNA concentration.** (**a**) The presence of magnesium pyrophosphate precipitate in droplets where LAMP was performed is correlated to integrated droplet fluorescence. Images where droplets moved between brightfield and fluorescence imaging or with fluorescence aberrations are excluded. (**b**) The percentage

of droplets containing precipitate increases as the target DNA concentration in a sample increases. (**c**) The percentage of droplets without precipitate is used to calculate λ (blue), the average number of target DNA molecules per droplet, which is linearly related to the original DNA concentration ($\lambda = \omega^{-1} \cdot Conc_{DNA} \cdot Vol_{drop}$). Bayesian inference yields a median inefficiency factor ω of 127.14 and confidence interval (gray band, 99% HPD), indicating that there is a ∼127x inefficiency factor when performing LAMP in droplets. Inference also yields 99% HPD intervals (black) for each sample's λ estimate that are drawn back to linearity.

When performing the same Bayesian inference using thresholded fluorescence values instead of precipitate presence (Figure 3.A.2) ω is larger and has a wider posterior (median=204.48, 99% CI [195.09, 214.47]). Improved efficiency for reading precipitate presence vs. fluorescence can be attributed to the loss of some fluorescent droplets that are removed due to fluorescence photobleaching or droplet movement. Additionally, the fluorescence threshold used is determined by finding a local minimum in the intensity distribution, which may be imprecise or difficult to determine with an imbalanced distribution.

3.2.3 Automated classification of precipitate images

Automated classification of droplet images is enabled by image processing. To process and analyze droplet images for the presence of precipitate, some form of image processing is required. Detecting the precipitate is a challenge because although the fractal-like precipitate structures look similar, they vary in their size, morphology, location, and sharpness. A simple approach to droplet classification entails generating intensity-based statistics for each image, including mean and median intensity, sharpness, and measuring the result of automated thresholding. This approach is useful, but does not account for differences in lighting, or small or out of focus precipitates. Convolutional neural nets are another viable approach to automated classification [31]. This solution would likely be able to recognize the fractal subunits of the precipitate in a few different presentations. However, there is a degree of reduction of interpretability of neural nets, which would make it more difficult to

understand why an image was misclassified. In this paper we have chosen to implement the previously mentioned BOVW algorithm, which builds a dictionary of image patches (visual words) and then matches and counts the occurrence of image patches in each image [28]. Given a dictionary of a specified size, a feature vector of word counts is generated for each image, which can be utilized by a machine learning algorithm for automated classification of droplets. This method excels by recognizing a set of visually similar image patches, such as the fractal sub-units, that appear a variable number of times per image. We're able to diagnose the BOVW model by seeing which image patches are extracted from a droplet image, and whether they are indicative of precipitate positive or negative droplets. The entirety of the 30,138 extracted images are randomly assigned to Training, Validation, and Testing sets according to a 64/16/20 split.

We build our BOVW model by automatically extracting Speeded Up Robust Features (SURF) keypoints [32] from regions of high contrast(Figure 3.3a). SURF keypoint extraction is scale and rotation invariant, yielding the keypoints with highest contrast in a small region. Each SURF keypoint is then described by dividing the region around the keypoint into a 4×4 grid, where 4 horizontal and vertical wavelet responses are summed in each cell, resulting in a 64-dimensional feature space for each keypoint. Additionally, the sign of Laplacian (SoL), which indicates if the keypoint represents a dark blob on a light background (positive) or a light blob on dark background (negative) is also calculated. SURF keypoints from the Training set droplets are clustered based on their 64 features into a predefined number of words to form the BOVW dictionary (Figure 3.3b). SURF keypoints with positive or negative SoL are clustered separately to form Dark and Light words, respectively (Figure 3.A.3). Additionally, SURF keypoints can be filtered by a metric representing their contrast. Low-contrast features are likely image artifacts, but there are potential benefits to creating low-contrast words that do not dilute the predictive power of high-contrast keypoints with similar appearance. Therefore, we also generate a set of low-contrast (Fuzzy) visual words that map to the same 64-dimensional feature space as corresponding high-contrast (Sharp) visual words. The number of SURF keypoints extracted from precipitate-negative and precipitate-positive

droplets are Poisson-distributed, with an average of 0.4 and 15.3 keypoints, respectively. The traditional BOVW model can be further extended by generating meta-features, such as number of total words per image, number of Sharp words, likely-precipitate words (based on the premise that precipitate is normally found near the center of the droplet), in addition to image statistics.

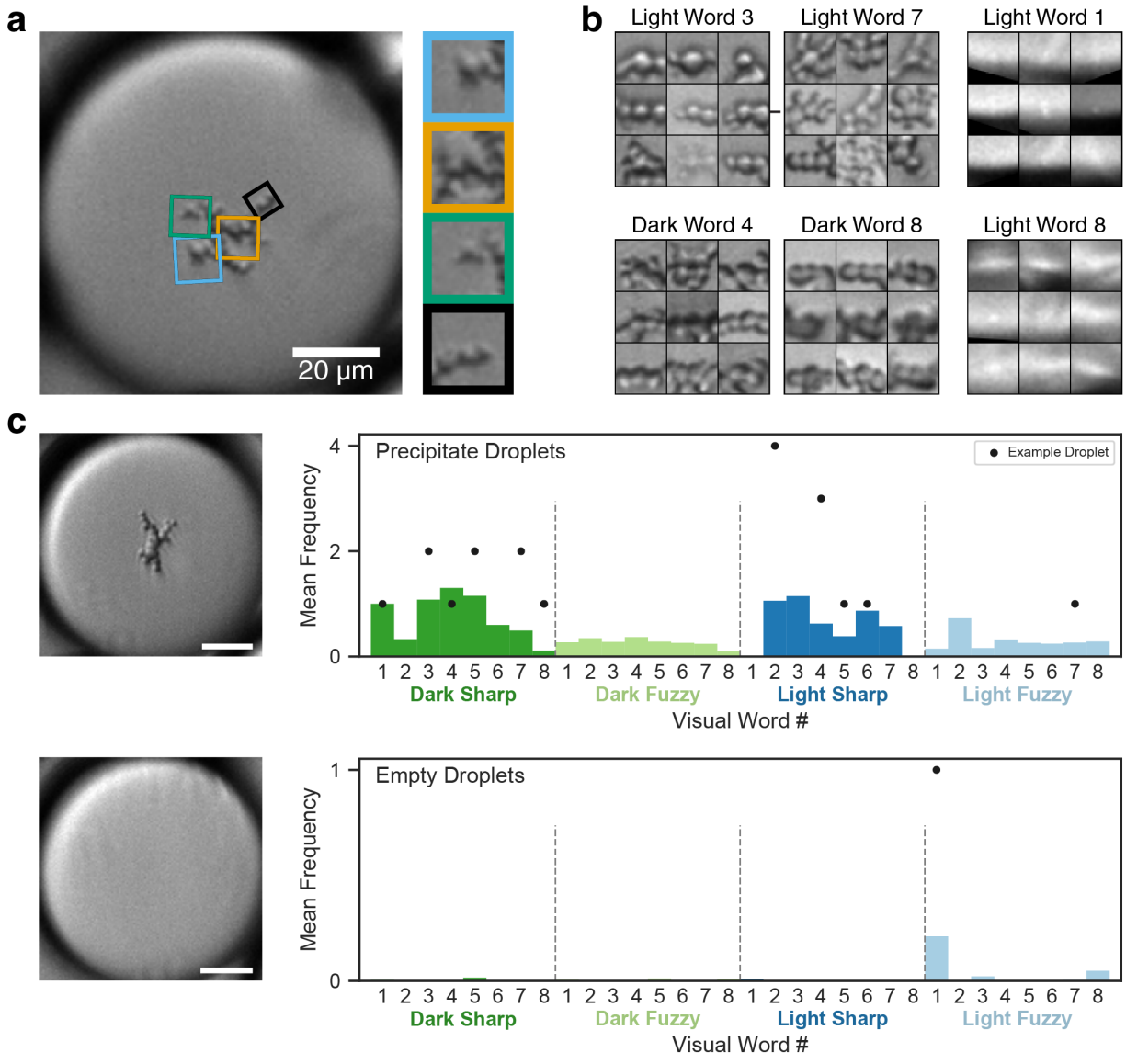

Figure 3.3: **Creation of Bag of Visual Words model from SURF keypoints.** (a) SURF keypoints, highlighted in colored boxes, are extracted from previously isolated images of droplets. SURF keypoints are scale and rotation invariant and are described with a

64-dimensional feature space. (**b**) The BOVW model is created by clustering SURF keypoints within their feature space to define words. Dark and Light words are clustered separately, according to the positive and negative Sign of Laplacian, respectively. SURF keypoints closest to the cluster centers are shown for some word examples. Words are further divided into Sharp and Fuzzy words, which overlap in the same feature space, but have different levels of contrast. (**c**) Example images of droplets with and without precipitate are processed in a BOVW model containing 32 words, with 8 words each of Dark/Sharp, Dark/Fuzzy, Light/Sharp, and Light/Fuzzy. The frequency of each type of word appearing in the images (circles), is compared to mean frequencies in the entire dataset (bars).

Several competing BOVW models are created that vary in the dictionary size, inclusion of low contrast keypoints, contrast cutoffs, meta-features, or image statistics. Each of these models is trained using a random forest classifier [33] using the set of Training droplet images, and compared against the Validation set. The ideal model has a high precision-recall Area Under the Curve (AUC), and receiver operating characteristic curve (ROC) AUC. The base selected BOVW model maximizes both measures and features 8 Dark words (and corresponding Fuzzy), 8 Light words (and corresponding Fuzzy) for a total of 32 words (Figure 3.3c, Figure 3.A.4). This model is augmented with BOVW meta-features and image statistics features. Feature importance calculation reveals that the tendency of a visual word to be found in the middle of the droplet ("Likely Precip Words"), droplet image sharpness (99^{th} percentile of the Laplacian of Gaussian), and total number of visual words in a droplet are most useful in classifying precipitate-positive droplets (see Figure 3.A.5 for the list of features, and relative importance via permutation importance [34]).

The augmented BOVW model achieves high levels of precision (positive predictive value) and recall (sensitivity) on the droplet Testing set. The default setting of the random forest classifier yields a precision of 0.988 and recall of 0.982 (Figure 3.A.6). The random forest classifier yields prediction scores of whether a droplet is a precipitate-positive droplet, which is shown for a set of droplets from the Training and Testing sets (Figure 3.4a, see

Figure 3.A.7 for representative droplet images across the range of prediction scores). Note that blurry/smaller precipitate with a lower prediction score are still classifiable.

At the default random forest setting, the classifier produces estimates for the average number of DNA molecules, λ, per sample that closely approaches the known values. There is a higher deviation from the known λ at the lowest concentration (on a logscale), due to a tendency towards false positives, as seen in the precision (Figure 3.4b, horizontal lines). Using the previously estimated inefficiency factor, ω, new Bayesian models generate posterior λ values for the Testing set ground truth and machine learning results as if the DNA concentration is unknown. The HPD intervals of the ground truth can recover linearity, but the HPD intervals of the machine learning results of the lowest DNA concentration are affected by false positives. This overestimation in λ would result in an overestimation of predicted bulk DNA concentrations. Overestimation for low numbers of precipitate-positive droplets could be mitigated by training a classifier that includes multiple classes, including one for droplets that may contain debris or image artifacts, which contribute to false positives.

Limits of detection are determined as a function of number of droplets and machine learning performance and can approach one copy per microliter with a million droplets. The average DNA per droplet (λ) for a given Poisson distribution can be more precisely estimated with a larger number of sampled droplets (Figure 3.A.8a). With the previously established linear relationship between λ and DNA concentration, we generate curves of required droplets to distinguish a sample from 0 DNA at 95% and 99% confidence levels (Figure 3.4c, see Bootstrapping performance boundary curves for more detail). In this study, 9,185 droplets are imaged for the lowest DNA concentration (57 copies DNA $\cdot$ μL^{-1}), which is less than the 15,617 droplets needed to differentiate from a 0 DNA sample with 95% confidence. Distinguishing a sample with 11.3 copies DNA $\cdot$ μL^{-1} would require 83,000 and 138,000 droplets to achieve 95% and 99% confidence, respectively. On average, approximately 2 times as many droplets are required to move from 95% to 99% confidence levels. Achieving this level of performance can be made more feasible by improving the machine learning model, or decreasing the droplet size, which would speed up imaging.

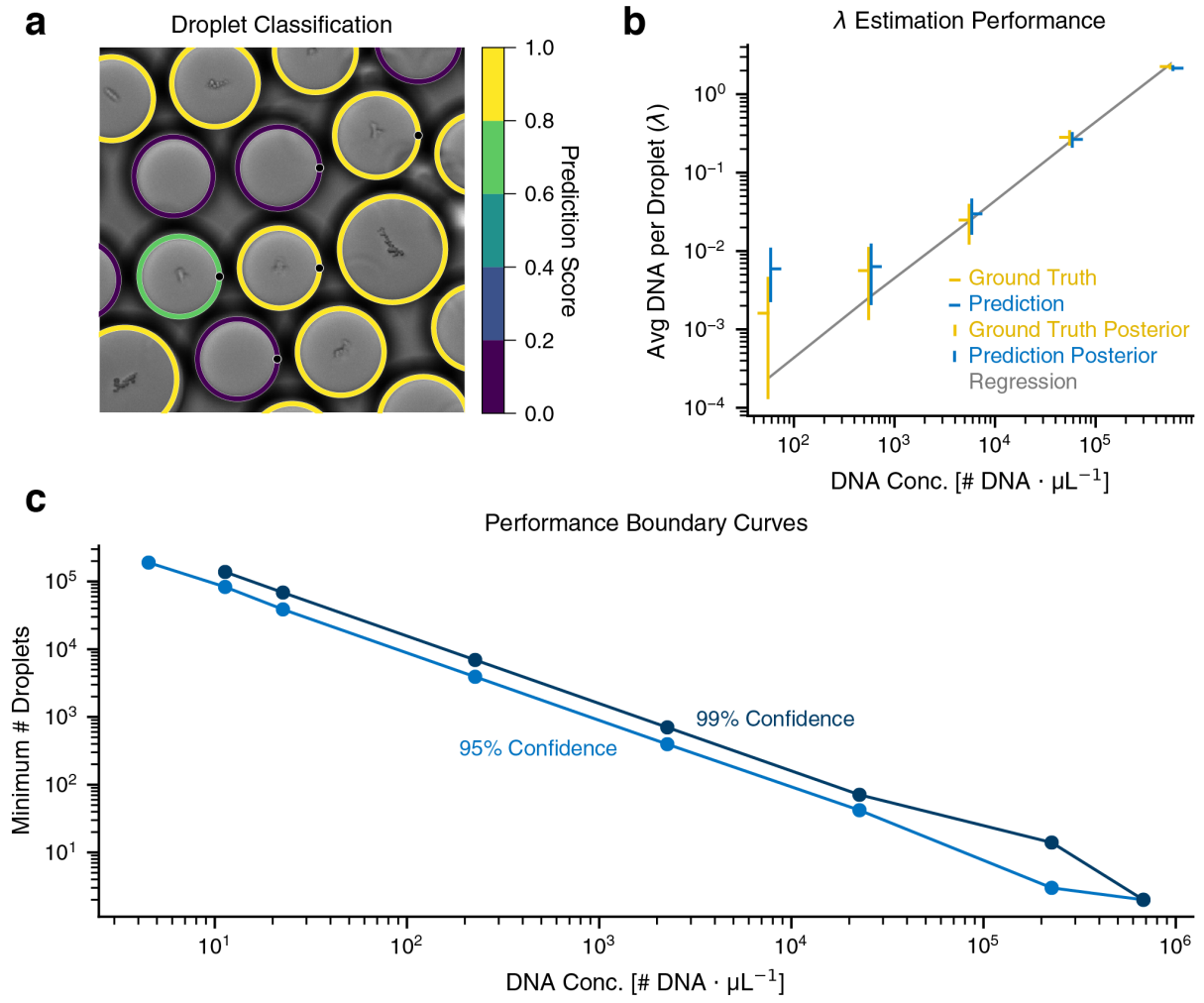

Figure 3.4: **Classification of droplets predicts Testing set λ, and DNA concentration.** (**a**) Random forest classification of droplets. Testing set droplets indicated with black circle markers, all others are from Training and Validation sets. Color on outlining circles indicate prediction score of a precipitate-positive droplet. The threshold to classify a droplet as precipitate-positive can be adjusted but is 0.5 by default. (**b**) λ values for droplet predictions (blue, horizontal) and ground truth (yellow, horizontal) are computed as before (with 0.5 threshold) and related to bulk DNA concentration. The predicted λs with this classifier score threshold are consistently higher than the ground truth, indicating a systematic propensity to classify false positives, and limitations of low droplet count. Bayesian estimates of the λ HPD intervals (vertical) illustrate the ability to recover valid ranges of

λ values for unknown DNA concentration but can be susceptible to false positives at low concentrations. (**c**) Bootstrapping across a range of λs and droplet sample sizes enables the calculation of the minimum number of droplets needed to distinguish a sample from 0 DNA at 95% or 99% confidence levels (Figure 3.A.8, see Bootstrapping performance boundary curves for more detail).

3.3 Discussion

In this paper we have presented Fractal-LAMP, a method to perform label-free DNA detection and quantification using a digital assay. Performing LAMP in droplets allows us to detect DNA amplification via magnesium pyrophosphate precipitate accumulation. This precipitate is visible in droplets in brightfield and is correlated to overall DNA intercalating dye fluorescence. We were able to develop an automated computer vision algorithm utilizing BOVW to accurately detect the presence of precipitate that varied in presentation. The practical limit of detection is affected by the performance of our computer vision algorithm, as well as the number of droplets imaged, however, high quantitative accuracy in predicting DNA concentration is achieved over at least 3 orders of magnitude.

Digital, label-free LAMP is an attractive method to detect low concentrations of DNA and quantify the amount of target DNA in a sample. A label-free approach eliminates the need for extra optical equipment and dyes to generate and read fluorescence. Brightfield microscopic imaging systems can be more cost-effective, larger field of view, and longer depth of field to fluorescence systems [35, 36]. Furthermore, by only requiring brightfield imaging, we can image droplets on cell phone imaging platforms, which are more portable than conventional microscopes. In addition, common intercalating dyes have been shown to delay the speed of DNA amplification and may be unstable [23]. We have previously observed the instability of EvaGreen fluorescence over time, with changing temperatures, and witnessed photobleaching in this paper. Independence from fluorescence dyes also obviates the need to determine fluorescence value cutoffs, as the presence or absence of precipitate is a clear binary state.

Droplets are an advantageous method to partition bulk solution for digital assays. Whether using serial generation with 3D printed devices [37], or massively parallelized implementations [38], droplet generators can quickly partition bulk solution into monodisperse volumes. Engineered carrier microparticles can even be used to emulsify a bulk solution into controlled volumes without the need for microfluidics or droplet generators for the end user. The imaging of static droplets in this paper can be accelerated using wide-field brightfield imagers based on consumer electronic devices, which have been previously demonstrated by us [39, 35, 36, 40] and others and may be compatible with this system.

While this paper imaged static droplets, there is the potential for droplets to also be imaged in continuous flow, enabling high-throughput potential, especially if detecting precipitate presence without the need for fluorescence analysis, which has been previously required [27, 41, 42]. The recent work by *Yelleswarapu et al.* demonstrates multichannel high throughput imaging of droplets in flow. Our droplets and fractal precipitate are likely compatible with this imaging setup and eliminate the need for fluorescence readout, which requires longer exposure time. In combination with the system detailed in *Yelleswarapu et al.*, extremely intense illumination and sub-microsecond exposure times could potentially eliminate the need for streak imaging. We anticipate measurement in flow is also possible using high-speed cameras that intrinsically have high sensitivity and short exposure times. For example we have used high-speed cameras with frame rates of hundreds of thousands of frames per second in previous work analyzing deformation of cells [43]. For droplets we expect that internal motion of precipitates in moving droplets in a channel could be frozen in space at sufficiently high frame rates, and therefore analyzed without motion blur. The localization of precipitate at the bottom of the droplet may be disturbed in this case unless clever design of the channels is used to minimize disturbing recirculating flows in droplets, which would be a concern for any method of imaging in flow. Nevertheless, imaging droplets in flow would be an exciting next step for analysis of precipitate-producing reactions in droplets, reducing practical limits of detection that our current imaging imposes.

Our computer vision algorithm excelled at detecting the magnesium pyrophosphate frac-

tal precipitate in droplets. This precipitate varied in both size, shape and focus, but with sufficiently high numbers of example images, our algorithm was able to learn to distinguish precipitate from debris or small incorporated oil drops. Precipitate detection from brightfield images could be improved by restricting the imaging chamber height, to reduce out-of-focus precipitate, and collecting more example images. Alternative algorithms such as convolutional neural nets [31] may also provide a boost in performance that allows us to achieve lower limits of detection while imaging fewer droplets. Imaging and computer vision algorithms may not be needed entirely if digital LAMP shows enhanced turbidity or light scattering for individual drops, and precise fiber optics can be aligned to detect alterations in light transmission.

There are several important future directions that can further enhance Fractal-LAMP as a label-free, digital assay. To start, there are some limitations in the amplification reporting signals. Neither the intercalating dyes nor magnesium pyrophosphate precipitate generated are sequence specific, which is a general limitation of LAMP. They can report that the amplification occurred, but not guarantee which DNA was amplified. That will rely on the DNA primers, which are also susceptible to self-amplification. Using brightfield imaging alone we also cannot chemically confirm that the identified particles are in fact magnesium pyrophosphate precipitate, which at low quantities can resemble debris. We have not investigated the long-term stability of the precipitate in droplets, but it is expected that precipitate will remain stable over longer periods of time than intercalating dyes, which can photobleach. Performing Fractal-LAMP without any intercalating dyes should also reduce reaction time. This hints at the exciting possibility to collect and run Fractal-LAMP continuously with low cost instrumentation but analyze results of several experiments at a future date at a central location with higher complexity instrumentation. If we maintain the use of images to observe precipitate, we can use more robust methods such as wide-field imaging or holographic imaging augmented by neural networks which would allow detecting precipitate on more planes of focus [44, 45] at extreme throughputs, leading to lower limits of detection and higher quantitative accuracy.

3.4 Materials and methods

3.4.1 LAMP/DNA mix

The LAMP reaction was performed as described in previous work [23], with a few key changes. The polymerase concentration was doubled, and the EvaGreen (Biotium) concentration used was 2.5 µm . Studies were performed by serially diluting bacteriophage lambda DNA (Thermo Fisher) to yield concentrations of 5.7×10^1 copies DNA $\cdot$ µL^{-1}, 5.7×10^2 copies DNA $\cdot$ µL^{-1}, 5.7×10^3 copies DNA $\cdot$ µL^{-1}, 5.7×10^4 copies DNA $\cdot$ µL^{-1}, and 5.7×10^5 copies DNA $\cdot$ µL^{-1}.

3.4.2 Droplet formation and incubation

The prepared LAMP solution and DNA was co-injected into a microfluidic 3D droplet generator [29] with FC-40 and RAN fluorosurfactant to produce 0.56 ± 0.1 nL (diameter: 102.03 ± 6.02 µm) droplets. Generating 1,000 droplets took approximately 1.12 seconds. The emulsified samples were transferred from the droplet generator via tubing into 0.5 mL microcentrifuge tubes and incubated at 67℃for 2 hours, followed by 2 minutes at 80℃.

3.4.3 Droplet imaging

After incubation, the droplets were transferred via pipette to a 120 µm slit chamber for brightfield and fluorescence (FITC [535/45 nm]) imaging at 10x magnification. Images of several fields of view are captured for each sample chamber. Imaging 1,000 took approximately 200 seconds.

3.4.4 Image processing

Brightfield microscopy images are processed by a MATLAB script that identifies droplets (n=30,138, captured over 31 imaging sessions on the same day) with diameters 65 – 96 µm using a circle Hough Transform [46]. Brightfield images of droplets and corresponding

fluorescence images are cropped and resized for each detected droplet. Fluorescence intensity is calculated by integrating total fluorescence intensity of the image. When comparing droplet fluorescence values, 7% of the field of views across all DNA concentrations are discarded due to droplet movement between acquiring brightfield and fluorescence images, photobleaching of the intercalating dye, or inconsistent illumination across the fluorescence images. This results in an 18% reduction to the total number of droplets considered (n=24,789) in our comparative analysis.

3.4.5 Dataset creation

All droplet images are manually inspected and marked for presence of precipitate. Droplet images are divided into Training, Validation, and Testing sets following a 64/16/20 split. Competing models are trained on the Training set and compared on the Validation set. Finally, the most performant model is run with the Testing set.

3.4.6 Bayesian regression

Bayesian inference is conducted with `PyMC3` [47] and No U-Turn MCMC Sampler [48] to perform a regression and calculate an inefficiency factor (slope) from which the observed λ deviates from the ideal λ. This is performed by creating a hierarchical Bayesian model where the likelihood for each j^{th} DNA concentration is a binomial distribution based on the number of precipitate-positive droplets n_j in its Training set N_j:

$$\sum_{i}^{N} 1\left\{X_i > 0\right\} = n_j \sim Binomial(N_j, \theta_j) \tag{3.1}$$

$$\theta_j = 1 - e^{-\lambda_j} \tag{3.2}$$

λ_j is distributed as a product of a gamma prior and inefficiency factor, ω, which is shared across all DNA concentrations:

$$\lambda_j \sim Gamma\left(\alpha_j,\ \beta\right) \cdot \frac{1}{\omega} \tag{3.3}$$

ω has a log-normal prior which is centered at 1, with 0.01 and 100 being equally as likely:

$$\omega \sim LogNormal\left(\mu = 0,\ \sigma = 4\right) \tag{3.4}$$

The gamma prior for each concentration is moderately informed by its ideal λ value, and the confidence we would have after measuring this λ value from 5,000 droplets:

$$\alpha_j = \lambda_{j,\ ideal} \cdot 5,000 \tag{3.5}$$

$$\beta = 5,000 \tag{3.6}$$

Three chains of 2,000 steps and 2,000 discarded tuning steps are used by the sampler (Figure 3.A.9).

3.4.7 Bag of visual words creation

A BOVW model is constructed from Training brightfield droplet images. Image patches of interest are identified via SURF keypoint extraction, which yields image patch centroids, orientation, and 64 wavelet responses. Visual words are created by clustering 64-dimensional wavelet features. SURF keypoints with negative (Light) and positive SoL (Dark) are clustered separately. SURF keypoints are further divided according to a sharpness metric (Fuzzy/Sharp), yielding 4 sets of visual words with 8 words each. The frequency of visual words appearing in droplet images is used to construct features used to classify images for presence of precipitate.

3.4.8 Random forest classification

BOVW features are combined with meta features and image statistics to create a final feature set. A random forest classifier uses this feature set to identify precipitate-positive droplets. Feature generation and classification per 1,000 droplets took approximately 13 seconds on a standard computer.

3.4.9 Bayesian inference of testing set

Two Bayesian models are constructed similarly to the previous model used on the Training set using either the Testing ground truth, or the predicted machine learning results. The posterior of the previously estimated ω is used instead of the relatively uninformed prior used before. In this case, we want to evaluate the models if the actual DNA concentration is unknown, so an uninformed gamma prior is used where $\alpha = 0.001,\ \beta = 0.001$ (Figure 3.A.10).

3.4.10 Limit of detection calculation

Repeated sampling of a specified number of droplets from a Poisson distribution can be used to generate a confidence interval for the estimate of λ. True positive and false positive rates from the machine learning algorithm is applied to simulated repeat sampling of droplets to generate confidence intervals for estimates of λ (Figure 3.A.8b). Confidence intervals for a given λ across a range of droplet sample sizes is compared to confidence intervals for $\lambda = 0$ (DNA concentration = 0). The point at which the confidence intervals for the two λs no longer overlap, tells us the minimum number of droplets needed to distinguish a sample from a 0 DNA condition (Figure 3.A.8c-d, see Bootstrapping performance boundary curves for more detail).

3.A Appendix

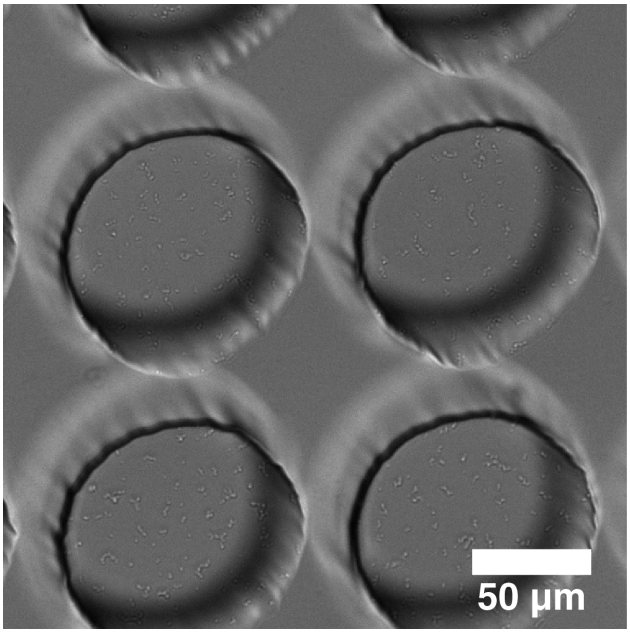

Figure 3.A.1: **LAMP precipitate presence in microwells.** LAMP performed in 100 µm wide microwells produces magnesium pyrophosphate precipitate that adheres to the surfaces.

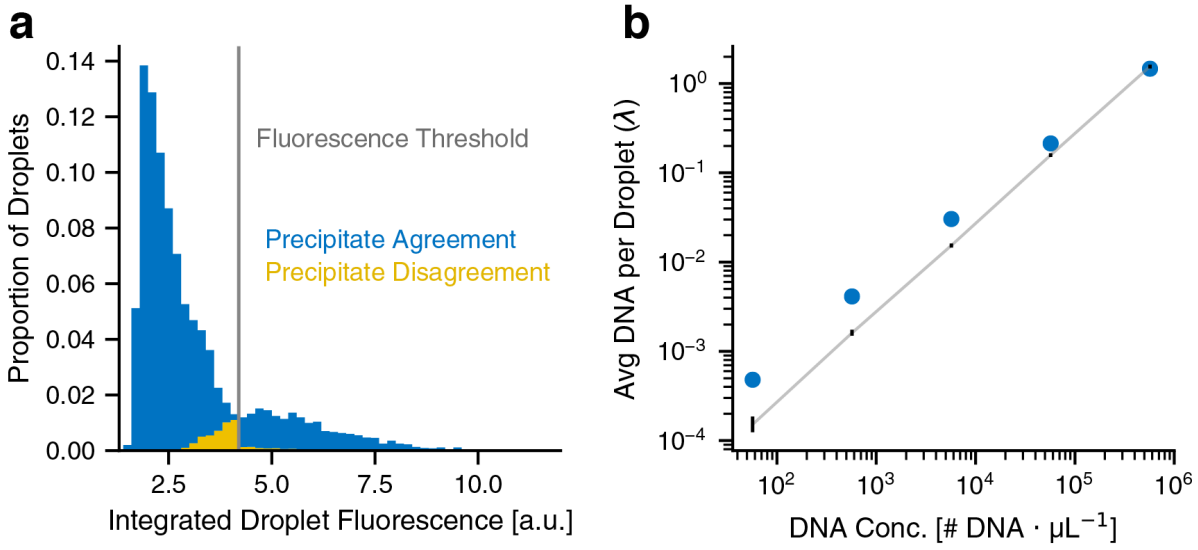

Figure 3.A.2: **Performance with fluorescence thresholding.** **(a)** Integrated droplet fluorescence is used to distinguish positive and negative droplets with a manually selected threshold (gray). Droplets with differing labels via precipitate and fluorescence thresholding are indicated in yellow. **(b)** Bayesian inference is performed with a fluorescence-thresholded ground truth. The naïve λ calculations (blue) are lower than that of the precipitate derived ground truth. Bayesian inference yields a median inefficiency factor ω of 204.48 and confidence interval (gray, 99% HPD), indicating that there is a $\sim$204x inefficiency factor when performing LAMP in droplets when reading out with fluorescence. Inference also yields 99% HPD intervals (black) for each sample's λ estimate that are drawn back to linearity.

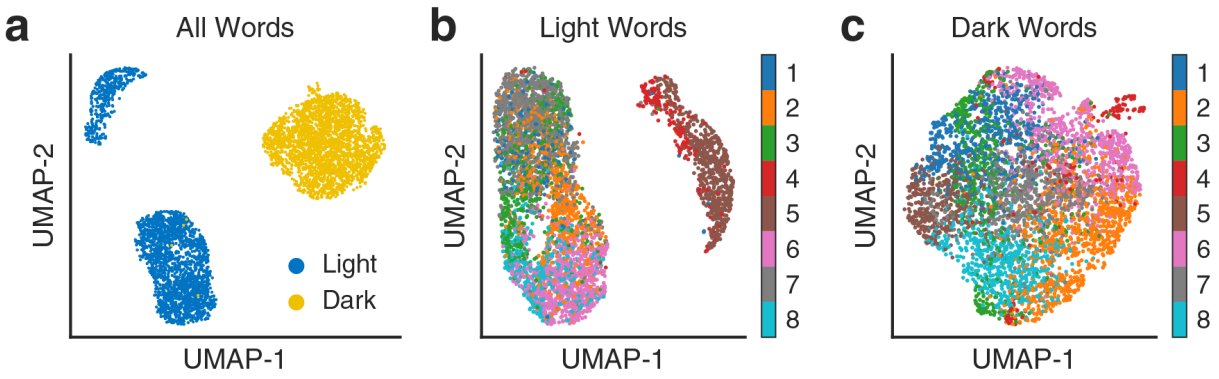

Figure 3.A.3: **Visualization of SURF clustering into visual words.** (**a**) The 64-dimensional feature space of Training set SURF keypoints are embedded in two dimensions via the U-MAP algorithm [49]. Keypoints are colored by Sign of Laplacian, which is embedded in the SURF feature-space, and is later used to separate Light (negative), and Dark (positive) words. (**b-c**) U-MAP dimensionality reductions performed separately on Light and Dark words demonstrates clustering of visual words. A random selection of 5,000 points are plotted after each dimensionality reduction.

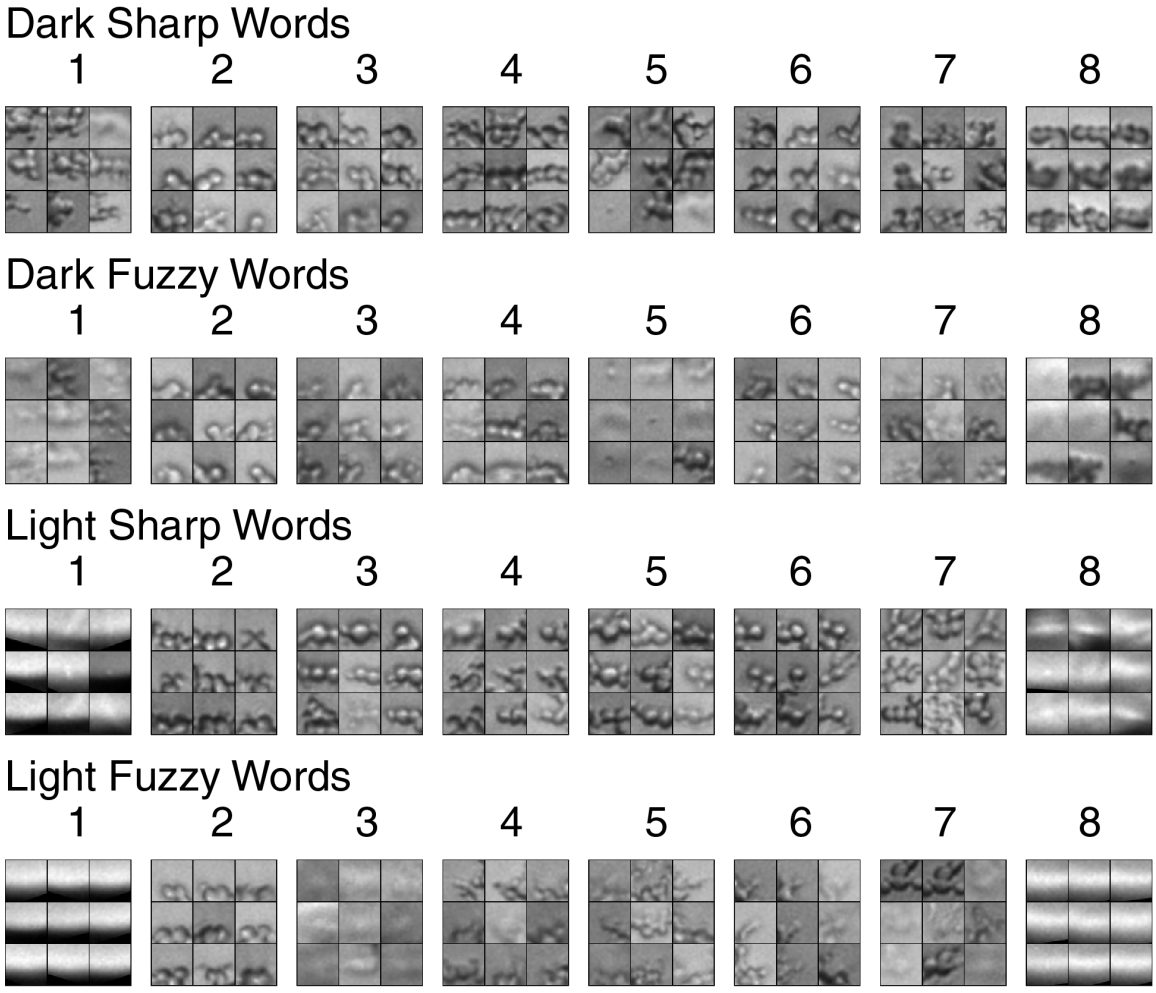

Figure 3.A.4: **Examples of visual words.** Members of visual words groups whose feature-space is closest to the centroid of the group. Sharp and Fuzzy words map onto the same feature-space of the corresponding Light and Dark words. Image patches are rotated based on initial extracted keypoints.

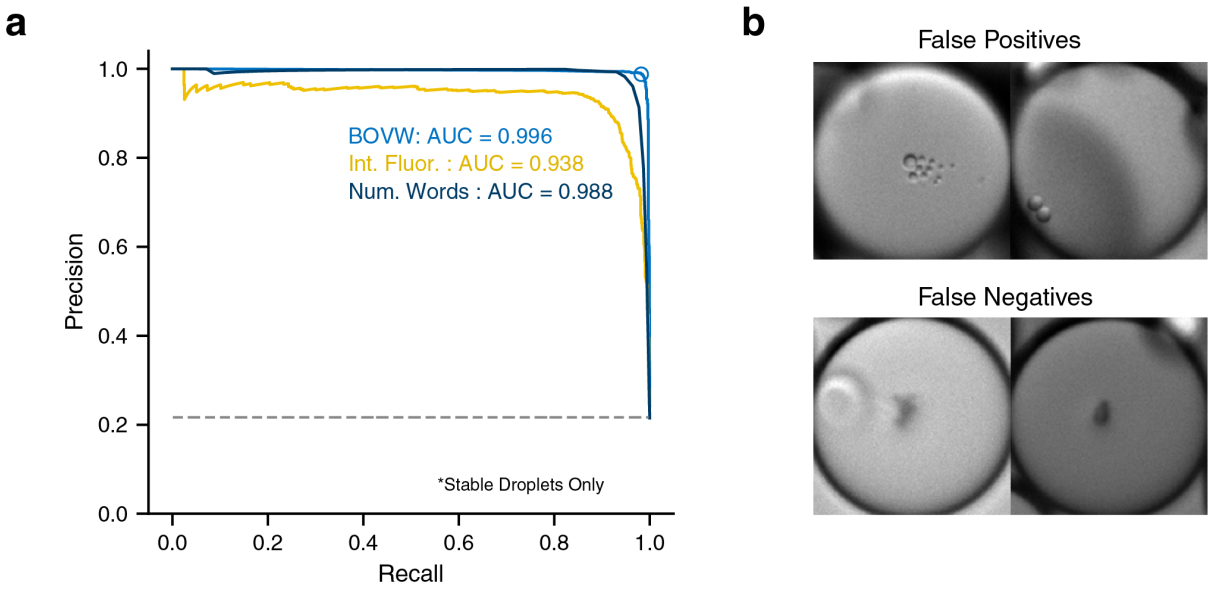

Figure 3.A.5: **Estimated importance of features in final random forest model.** Feature importance in a random forest model is calculated by permuting a feature's values and measuring a decrease in model performance. Features with lower performance may be unhelpful or may be redundant to other features higher on the list. Original BOVW features are shown in blue, meta-BOVW features are in dark blue, and image statistic features are in yellow.

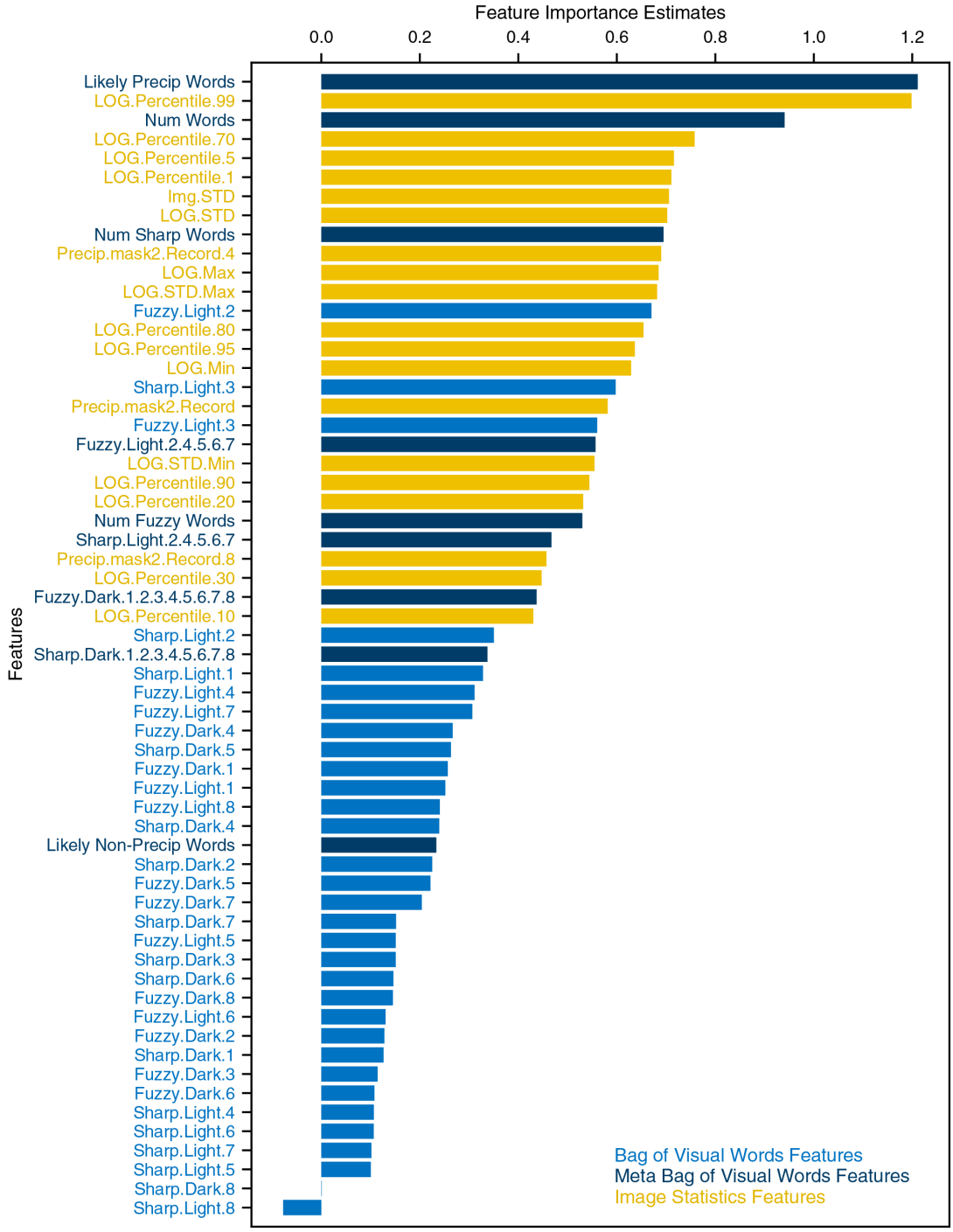

Figure 3.A.6: **Augmented BOVW model outperforms simpler models.** (a) A Precision-Recall (P-R) curve is used to assess the BOVW performance on the Testing set, due to the precipitate-empty droplet class balance (∼20:80). The P-R curve of the BOVW is

compared to simpler models, such as integrated fluorescence, and total number of words per image. These curves are summarized by the area under the curve (AUC). In order to compare the performance of the integrated fluorescence model, droplets are excluded that moved during imaging, or have fluorescence aberrations, as before. The unfilled circle indicates the default operating point of the BOVW (**b**) Examples of false positives from random forest classification, which has detected small oil droplets within the LAMP droplets. The model misses some precipitate that are out of focus, which are labeled as false negatives.

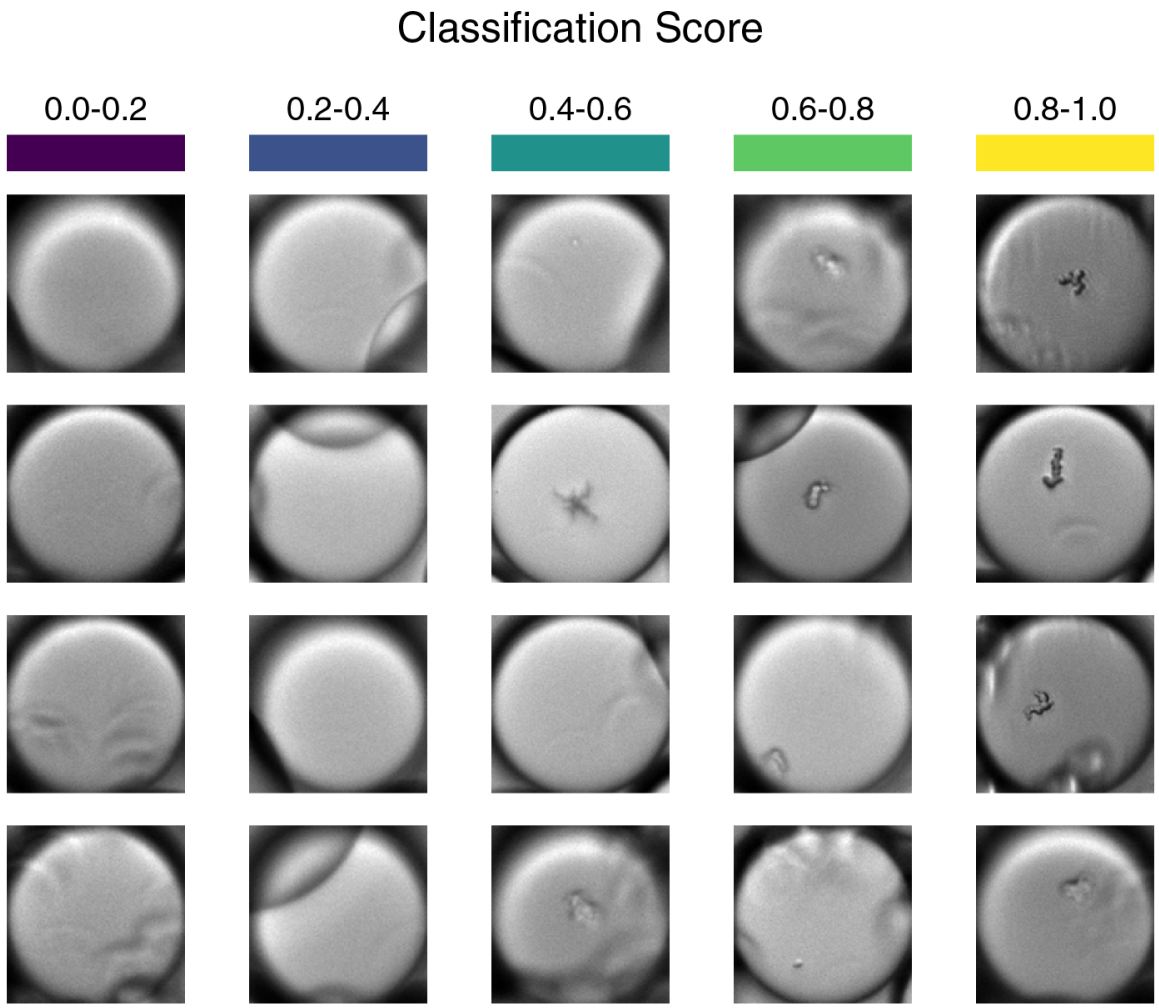

Figure 3.A.7: **Visual examples of random forest classifier scores.** Droplets randomly selected from 5 classifier score ranges (Figure 3.4) are shown. The middle range (0.4 – 0.6) includes droplets that will be classified as positive (≥ 0.5) and negative (< 0.5).

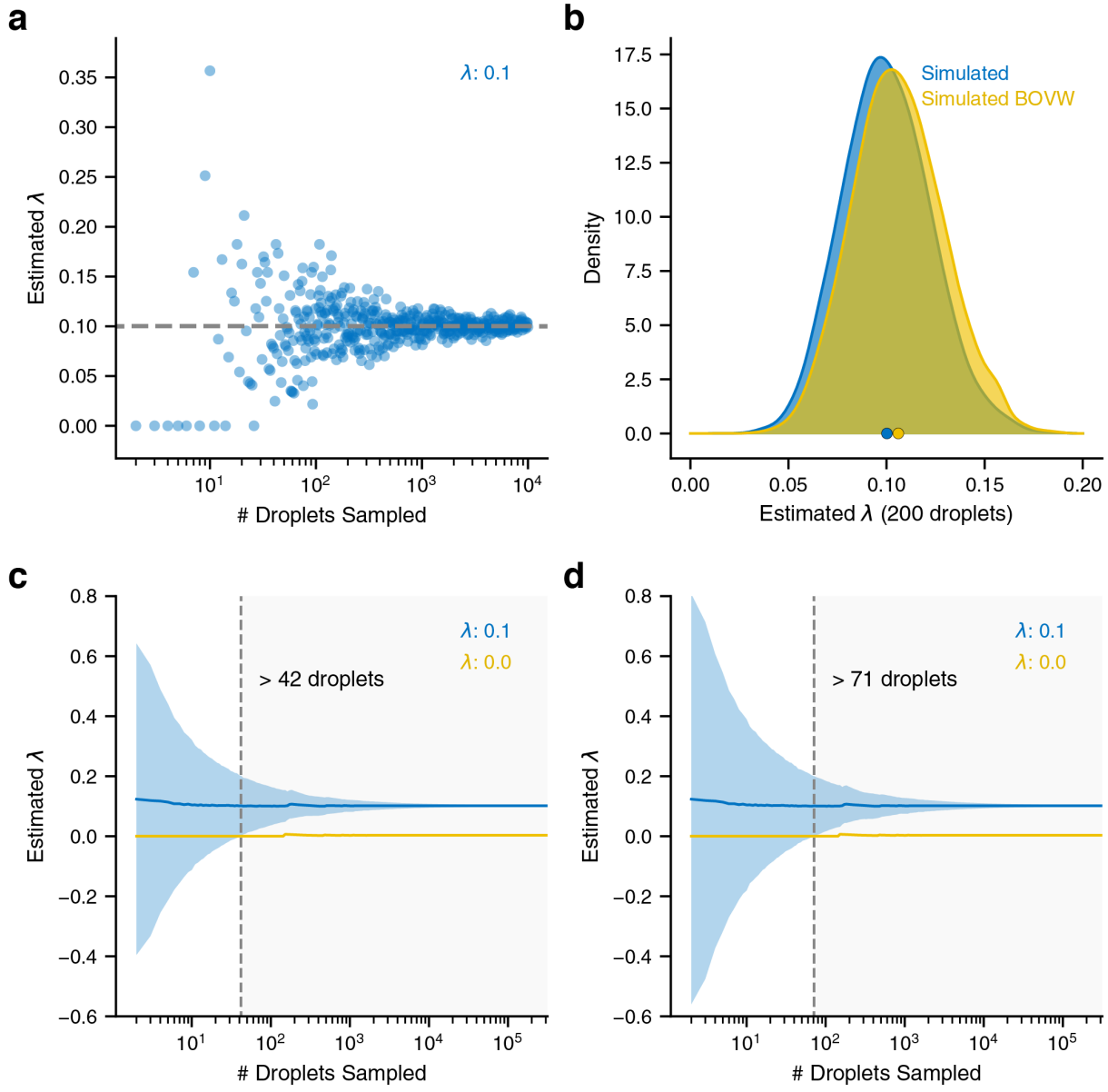

Figure 3.A.8: **Bootstrapping determines minimum number of droplets to sample for a given Poisson distribution and confidence interval.** (**a**) For a Poisson distribution of droplets with a known λ (0.1 DNA per droplet), the number of droplets sampled will affect the ability to estimate the true λ. As more droplets are sampled, the estimated λ converges on the true λ. (**b**) In addition to increasing the sample size of droplets to determine the true λ, repeat sampling (10,000 iterations) of a given sample size (200 droplets) will converge on the true λ, in the form of a normal distribution (blue). Our ability to estimate the

true λ is affected by the sensitivity (true positive rate) and specificity (true negative rate) of our BOVW system (yellow). Circles mark means of corresponding samples. (**c-d**) These simulations taking into account the performance of the machine learning system are run across a range of droplet sample sizes and λ ranges. For each simulation, an aribitrary confidence interval can be calculated, since it is normally distributed. For a given confidence level (95% in **c**, 99% in **d**), the point at which the confidence interval for a given λ (blue shaded region) separates from the confidence interval of $\lambda = 0$ (yellow shaded region), indicates how many sampled droplets are necessary to distinguish the two samples. After converting λ into bulk DNA concentrations ($Conc_{DNA} = \lambda \cdot \omega \cdot {Vol_{drop}}^{-1}$), we can determine the minimum number of droplets needed to distinguish a given concentration from 0 at confidence intervals of 95% or 99% (Figure 3.4c, see Bootstrapping performance boundary curves for more detail).

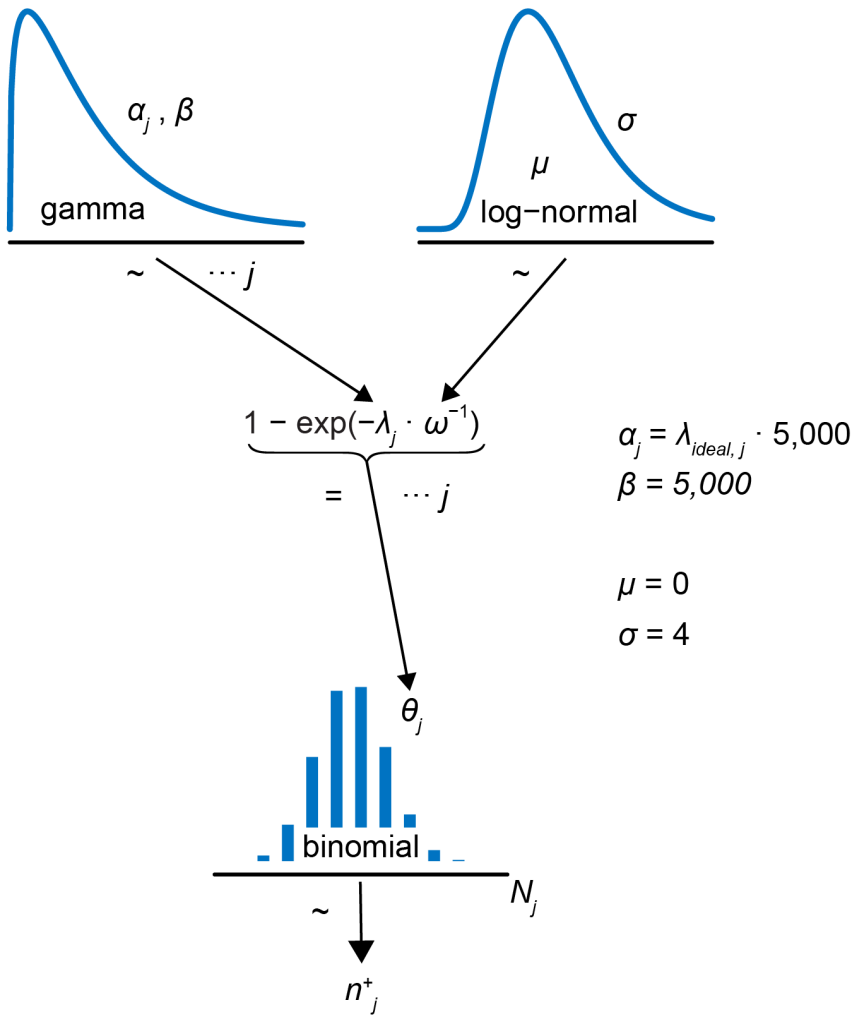

Figure 3.A.9: **Hierarchical Bayesian model for Training set.** A hierarchical Bayesian model is used to perform a regression and calculate an inefficiency factor ω from which the observed λ deviates from the ideal λ. The likelihood for each j^{th} sample is a binomial distribution ($\sum_i^N 1\{X_i > 0\} = n_j^+ \sim Binomial(N_j,\ \theta_j)$ based on the number of precipitate–positive droplets n_j^+ in its Training set N_j, and $\theta_j = 1 - e^{-\lambda_j}$. λ_j is distributed as a product of a gamma prior and inefficiency factor ω, which is assumed to be shared across all samples ($\lambda_j \sim Gamma\,(\alpha_j,\ \beta) \cdot \frac{1}{\omega}$). ω has a log-normal prior ($\omega \sim LogNormal\,(\mu = 0,\ \sigma = 4)$) which is centered at 1. The gamma prior for each concentration is moderately informed by its ideal λ value ($\alpha_j = \lambda_j,\ ideal \cdot 5{,}000; \beta = 5{,}000$).

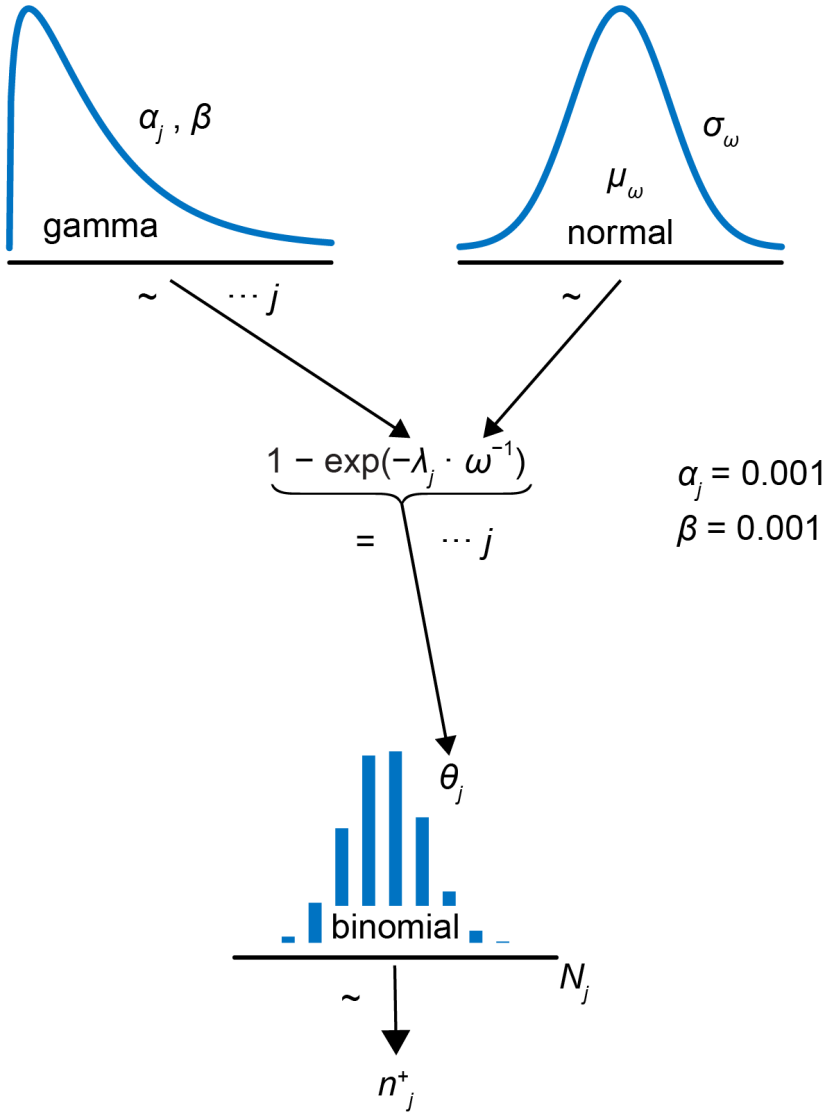

Figure 3.A.10: **Hierarchical Bayesian model for Testing set.** A Bayesian model is constructed similarly to the previous model used on the Training set using either the Testing ground truth, or the predicted machine learning results. The posterior of the previously estimated ω is used by fitting a normal distribution to ω. When evaluating unknown DNA concentrations an uninformed gamma prior is used where $\alpha = 0.001,\ \beta = 0.001$.

3.A.1 Bootstrapping performance boundary curves

We use a bootstrapping method to assess our ability to measure a given Poisson distribution from a specified sample size. In this style of digital assay, we are not able to determine the number of original DNA copies loaded into each droplet and fit the Poisson distribution. Rather, we must estimate λ by counting the number of positive droplets n^+ in a sample of N droplets:

$$X_i \sim Poisson(\lambda, N) \tag{3.A.1}$$

$$n^+ = \sum_i^N 1\{X_i > 0\} \tag{3.A.2}$$

$$\lambda = -\ln\left(1 - \frac{n^+}{N}\right) \tag{3.A.3}$$

Our ability to measure a Poisson distribution accurately is dependent on the random sampling of droplets from a population and the number of droplets. Sampling a larger number of droplets allows us to more consistently approach the true λ of a Poisson distribution (Figure 3.A.8a). With a defined sample size, repeatedly drawing new random samples from a distribution will have some variation in estimating λ. By estimating λ of many (10,000) random samples of fixed size from the same distribution, we can create a distribution that illustrates the likelihood of estimating the true λ (Figure 3.A.8b).

In our method, we are not only sampling droplets, but also applying a machine learning algorithm to classify them. When using an algorithm with imperfect sensitivity and specificity, negative and positive droplets will be misclassified according to the False Positive Rate (FPR) and False Negative Rate (FNR), resulting in a modified number of positive droplets observed, n^{+*}:

$$n^{+*} = n^+ \cdot FNR + (N - n^+) \cdot FPR \tag{3.A.4}$$

By repeatedly sampling as before but applying the FPR and FNR to each sample simulates how the machine learning algorithm would estimate λ ("Simulated BOVW"). This affects our calculated λ for a sample, including a sample drawn from a λ=0 distribution, which could have a non-zero estimate due to the FPR. Recovering the true λ is important, but we may not always be able to do so, especially as λ approaches zero. However, we can still predict whether a particular sample would have a λ distinguishable from λ=0. Given how our machine learning algorithm can affect positive droplet counts, we want to distinguish samples from a λ=0 sample to understand our limit of detection. We can approximate the λ distributions as normal, allowing us to calculate 95% and 99% confidence intervals from the standard deviations. If confidence intervals of a particular λ and λ=0 do not overlap, we can distinguish the given Poisson distribution from λ=0, at the given confidence level. For a range of λ, we generate distributions across a range of sample sizes, and determine where they no longer overlap with λ=0 at 95% and 99% confidence intervals (Figure 3.A.8d). Finally, the sampled λ values are converted into concentration according to:

$$Conc_{DNA} = \lambda \cdot \omega \cdot {Vol_{drop}}^{-1} \tag{3.A.5}$$

Bibliography

[1] L. Benesova, B. Belsanova, S. Suchanek, M. Kopeckova, P. Minarikova, L. Lipska, M. Levy, V. Visokai, M. Zavoral, and M. Minarik. Mutation-based detection and monitoring of cell-free tumor DNA in peripheral blood of cancer patients. *Analytical Biochemistry*, 433(2):227–234, Feb 2013.

[2] John G Tate, Sally Bamford, Harry C Jubb, Zbyslaw Sondka, David M Beare, Nidhi Bindal, Harry Boutselakis, Charlotte G Cole, Celestino Creatore, Elisabeth Dawson, Peter Fish, Bhavana Harsha, Charlie Hathaway, Steve C Jupe, Chai Yin Kok, Kate Noble, Laura Ponting, Christopher C Ramshaw, Claire E Rye, Helen E Speedy, Ray Stefancsik, Sam L Thompson, Shicai Wang, Sari Ward, Peter J Campbell, and Simon A Forbes. COSMIC: the Catalogue Of Somatic Mutations In Cancer. *Nucleic Acids Research*, 47(D1):D941–D947, Jan 2019.

[3] Angelika Niemz, Tanya M. Ferguson, and David S. Boyle. Point-of-care nucleic acid testing for infectious diseases. *Trends in Biotechnology*, 29(5):240–250, May 2011.

[4] Roland Martzy, Claudia Kolm, Rudolf Krska, Robert L. Mach, Andreas H. Farnleitner, and Georg H. Reischer. Challenges and perspectives in the application of isothermal DNA amplification methods for food and water analysis. *Analytical and Bioanalytical Chemistry*, 411(9):1695–1702, Mar 2019.

[5] Lu Zhang, Baozhi Ding, Qinghua Chen, Qiang Feng, Ling Lin, and Jiashu Sun. Point-of-care-testing of nucleic acids by microfluidics. *TrAC Trends in Analytical Chemistry*, 94:106–116, Sep 2017.

[6] Lilit Garibyan and Nidhi Avashia. Polymerase Chain Reaction. *Journal of Investigative Dermatology*, 133(3):1–4, Mar 2013.

[7] M. Monsur Ali, Feng Li, Zhiqing Zhang, Kaixiang Zhang, Dong-Ku Kang, James A. Ankrum, X. Chris Le, and Weian Zhao. Rolling circle amplification: a versatile tool for chemical biology, materials science and medicine. *Chemical Society Reviews*, 43(10):3324, Apr 2014.

[8] Yasuyoshi Mori, Kentaro Nagamine, Norihiro Tomita, and Tsugunori Notomi. Detection of Loop-Mediated Isothermal Amplification Reaction by Turbidity Derived from Magnesium Pyrophosphate Formation. *Biochemical and Biophysical Research Communications*, 289(1):150–154, 2001.

[9] Carlos Duarte-Guevara, Vikhram V. Swaminathan, Bobby Reddy, Jui-Cheng Huang, Yi-Shao Liu, and Rashid Bashir. On-chip electrical detection of parallel loop-mediated isothermal amplification with DG-BioFETs for the detection of foodborne bacterial pathogens. *RSC Advances*, 6(106):103872–103887, Nov 2016.

[10] Eric Salm, Yu Zhong, Bobby Reddy, Carlos Duarte-Guevara, Vikhram Swaminathan, Yi-Shao Liu, and Rashid Bashir. Electrical Detection of Nucleic Acid Amplification

Using an On-Chip Quasi-Reference Electrode and a PVC REFET. *Analytical Chemistry*, 86(14):6968–6975, Jul 2014.

[11] Miyuki Tabata, Yurika Katayama, Fahmida Mannan, Ayaka Seichi, Koji Suzuki, Tatsuro Goda, Akira Matsumoto, and Yuji Miyahara. Label-free and Electrochemical Detection of Nucleic Acids Based on Isothermal Amplification in Combination with Solid-state pH Sensor. *Procedia Engineering*, 168:419–422, Jan 2016.

[12] Amar S Basu. Digital Assays Part II: Digital Protein and Cell Assays. *SLAS TECHNOLOGY: Translating Life Sciences Innovation*, 22(4):387–405, Aug 2017.

[13] Weili Chen, Hojeong Yu, Fu Sun, Akid Ornob, Ryan Brisbin, Anurup Ganguli, Vinay Vemuri, Piotr Strzebonski, Guangzhe Cui, Karen J. Allen, Smit A. Desai, Weiran Lin, David M. Nash, David L. Hirschberg, Ian Brooks, Rashid Bashir, and Brian T. Cunningham. Mobile Platform for Multiplexed Detection and Differentiation of Disease-Specific Nucleic Acid Sequences, Using Microfluidic Loop-Mediated Isothermal Amplification and Smartphone Detection. *Analytical Chemistry*, 89(21):11219–11226, Nov 2017.

[14] Aydogan Ozcan. Mobile phones democratize and cultivate next-generation imaging, diagnostics and measurement tools. *Lab Chip*, 14(17):3187–3194, Jul 2014.

[15] Sandeep Kumar Vashist, Onur Mudanyali, E. Marion Schneider, Roland Zengerle, and Aydogan Ozcan. Cellphone-based devices for bioanalytical sciences. *Analytical and Bioanalytical Chemistry*, 406(14):3263–3277, May 2014.

[16] Manmohan Parida, Santhosh Sannarangaiah, Paban Kumar Dash, P. V. L. Rao, and Kouichi Morita. Loop mediated isothermal amplification (LAMP): a new generation of innovative gene amplification technique; perspectives in clinical diagnosis of infectious diseases. *Reviews in Medical Virology*, 18(6):407–421, Nov 2008.

[17] Stephen W. Morton, Zhou J. Deng, Young Hoon Roh, Kevin E. Shopsowitz, and Paula T. Hammond. RNAi-Microsponges Form through Self-Assembly of the Organic and Inorganic Products of Transcription. *Small*, 10(8):1623–1633, 2013.

[18] Shoichi Takagi, Yuki Takahashi, Kanako Sugimura, Makiya Nishikawa, and Yoshinobu Takakura. Application of Magnesium Pyrophosphate-Based Sponge-Like Microparticles to Enhance the Delivery Efficiency and Adjuvant Effects of Polyriboinosinic-Polyribocytidylic Acid in Immune Cells. *Journal of Pharmaceutical Sciences*, 105(2):766–772, 2016.

[19] Haukur Gudnason, Martin Dufva, D.D. Bang, and Anders Wolff. Comparison of multiple DNA dyes for real-time PCR: effects of dye concentration and sequence composition on DNA amplification and melting temperature. *Nucleic Acids Research*, 35(19):e127, Oct 2007.

[20] Fei Mao, Wai-Yee Leung, and Xing Xin. Characterization of EvaGreen and the implication of its physicochemical properties for qPCR applications. *BMC Biotechnology*, 7(1):76, Nov 2007.

[21] Paul T. Monis, Steven Giglio, and Christopher P. Saint. Comparison of SYTO9 and SYBR Green I for real-time polymerase chain reaction and investigation of the effect of dye concentration on amplification and DNA melting curve analysis. *Analytical Biochemistry*, 340(1):24–34, May 2005.

[22] Kamalendu Nath, Joseph W Sarosy, Joyce Hahn, and Charles J Di Como. Effects of ethidium bromide and SYBR® Green I on different polymerase chain reaction systems. *Journal of Biochemical and Biophysical Methods*, 42(1-2):15–29, Jan 2000.

[23] Janay E. Kong, Qingshan Wei, Derek Tseng, Jingzi Zhang, Eric Pan, Michael Lewinski, Omai B. Garner, Aydogan Ozcan, and Dino Di Carlo. Highly Stable and Sensitive Nucleic Acid Amplification and Cell-Phone-Based Readout. *ACS Nano*, 11(3):2934–2943, 2017.

[24] Morteza Azizi, Meisam Zaferani, Soon Hon Cheong, and Alireza Abbaspourrad. Pathogenic Bacteria Detection Using RNA-Based Loop-Mediated Isothermal-Amplification-Assisted Nucleic Acid Amplification via Droplet Microfluidics. *ACS Sensors*, 4(4):841–848, 2019.

[25] Yi Hu, Peng Xu, Jing Luo, Hongxuan He, and Wenbin Du. Absolute Quantification of H5-Subtype Avian Influenza Viruses Using Droplet Digital Loop-Mediated Isothermal Amplification. *Analytical Chemistry*, 89(1):745–750, 2017.

[26] Xingyu Lin, Xiao Huang, Katharina Urmann, Xing Xie, and Michael R. Hoffmann. Digital Loop-Mediated Isothermal Amplification on a Commercial Membrane. *ACS Sensors*, 4(1):242–249, 2019.

[27] Tushar D Rane, Liben Chen, Helena C Zec, and Tza-huei Wang. Microfluidic continuous flow digital loop-mediated isothermal amplification (LAMP). *Lab on a Chip*, 15(3):776–782, 2015.

[28] Gabriella Csurka, Christopher R. Dance, Lixin Fan, Jutta Willamowski, and Cédric Bray. Visual categorization with bags of keypoints. In *In Workshop on Statistical Learning in Computer Vision, ECCV*, pages 1–22, 2004.

[29] Carson T. Riche, Emily J. Roberts, Malancha Gupta, Richard L. Brutchey, and Noah Malmstadt. Flow invariant droplet formation for stable parallel microreactors. *Nature Communications*, 7:1–7, 2016.

[30] John K. Kruschke. *Doing Bayesian data analysis : a tutorial with R, JAGS, and Stan*. Academic Press, 2nd edition, 2014.

[31] Alex Krizhevsky, Ilya Sutskever, and Geoffrey E. Hinton. ImageNet Classification with Deep Convolutional Neural Networks. In *NIPS*, pages 1097–1105, 2012.

[32] Herbert Bay, Andreas Ess, Tinne Tuytelaars, and Luc Van Gool. Speeded-Up Robust Features (SURF). *Computer Vision and Image Understanding*, 110(3):346–359, 2008.

[33] Leo Breiman. Random forests. *Machine Learning*, 45(1):5–32, 2001.

[34] Carolin Strobl, Anne-Laure Boulesteix, Thomas Kneib, Thomas Augustin, and Achim Zeileis. Conditional variable importance for random forests. *BMC Bioinformatics*, 9(1):307, Dec 2008.

[35] Alon Greenbaum, Wei Luo, Ting-Wei Su, Zoltán Göröcs, Liang Xue, Serhan O Isikman, Ahmet F Coskun, Onur Mudanyali, and Aydogan Ozcan. Imaging without lenses: achievements and remaining challenges of wide-field on-chip microscopy. *Nature Methods*, 9(9):889–895, Sep 2012.

[36] Alon Greenbaum, Yibo Zhang, Alborz Feizi, P.-L. Chung, Wei Luo, Shivani R. Kandukuri, and Aydogan Ozcan. Wide-field computational imaging of pathology slides using lens-free on-chip microscopy. *Science Translational Medicine*, 6(267):267ra175–267ra175, Dec 2014.

[37] Ming Li, Mark van Zee, Carson T. Riche, Bobby Tofig, Sean D. Gallaher, Sabeeha S. Merchant, Robert Damoiseaux, Keisuke Goda, and Dino Di Carlo. A Gelatin Microdroplet Platform for High-Throughput Sorting of Hyperproducing Single-Cell-Derived Microalgal Clones. *Small*, 14(44):1803315, Nov 2018.

[38] Joseph Michael de Rutte, Jaekyung Koh, and Dino Di Carlo. Scalable High-Throughput Production of Modular Microgels for In Situ Assembly of Microporous Tissue Scaffolds. *Advanced Functional Materials*, 29(25):1900071, Mar 2019.

[39] Tomas Aidukas, Regina Eckert, Andrew R. Harvey, Laura Waller, and Pavan C. Konda. Low-cost, sub-micron resolution, wide-field computational microscopy using opensource hardware. *Scientific Reports*, 9(1), Dec 2019.

[40] Alon Greenbaum, Uzair Sikora, and Aydogan Ozcan. Field-portable wide-field microscopy of dense samples using multi-height pixel super-resolution based lensfree imaging. *Lab on a Chip*, 12(7):1242–5, Apr 2012.

[41] Venkata Yelleswarapu, Joshua R. Buser, Margalit Haber, Jonathan Baron, Eshwar Inapuri, and David Issadore. Mobile platform for rapid sub–picogram-per-milliliter, multiplexed, digital droplet detection of proteins. *Proceedings of the National Academy of Sciences of the United States of America*, 116(10):4489–4495, 2019.

[42] Venkata R. Yelleswarapu, Heon-Ho Jeong, Sagar Yadavali, and David Issadore. Ultra-high throughput detection (1 million droplets per second) of fluorescent droplets using a cell phone camera and time domain encoded optofluidics. *Lab on a Chip*, 17(6):1083–1094, Mar 2017.

[43] D. R. Gossett, H. T. K. Tse, S. a. Lee, Y. Ying, a. G. Lindgren, O. O. Yang, J. Rao, a. T. Clark, and D. Di Carlo. Hydrodynamic stretching of single cells for large population mechanical phenotyping. *Proceedings of the National Academy of Sciences*, 109(20):7630–7635, 2012.

[44] Yichen Wu, Yair Rivenson, Yibo Zhang, Zhensong Wei, Harun Günaydin, Xing Lin, and Aydogan Ozcan. Extended depth-of-field in holographic imaging using deep-learning-based autofocusing and phase recovery. *Optica*, 5(6):704, Jun 2018.

[45] Yichen Wu, Yilin Luo, Gunvant Chaudhari, Yair Rivenson, Ayfer Calis, Kevin de Haan, and Aydogan Ozcan. Bright-field holography: cross-modality deep learning enables snapshot 3D imaging with bright-field contrast using a single hologram. *Light: Science & Applications*, 8(1):25, Dec 2019.

[46] T.J. Atherton and D.J. Kerbyson. Size invariant circle detection. *Image and Vision Computing*, 17(11):795–803, Sep 1999.

[47] John Salvatier, Thomas V. Wiecki, and Christopher Fonnesbeck. Probabilistic programming in Python using PyMC3. *PeerJ Computer Science*, 2:e55, Apr 2016.

[48] Matthew D. Hoffman and Andrew Gelman. The no-U-turn sampler: Adaptively setting path lengths in Hamiltonian Monte Carlo. *Journal of Machine Learning Research*, 15:1593–1623, 2014.

[49] Leland McInnes and John Healy. UMAP: Uniform Manifold Approximation and Projection for Dimension Reduction. pages 1–18, 2018.

CHAPTER 4

A comparison of microfluidic methods for high throughput cell deformability measurements

4.1 Introduction

Cell mechanical phenotype is a valuable indicator of changes in internal cell structure and is tightly associated with cell state and function [1, 2, 3]. Alterations in the mechanical properties of cells have been linked to many processes including cell cycle progression [4], cancer malignancy [5, 6, 7, 8], leukocyte activation [9, 10, 11, 12, 13], and stem cell differentiation [14, 11, 15, 16]. Measurements of cell mechanics circumvent the need of extrinsic labels, such as fluorescent dyes, and therefore constitute an attractive, non invasive biomarker for cell identification. Furthermore, as cell mechanics determines the magnitude of the mechanical response of cells to environmental forces, it can provide a biophysical perspective on cellular processes such as vascular circulation or migration in development and metastasis [17, 18].

Traditionally, methods such as atomic force microscopy [19], micropipette aspiration [20], optical stretching [21], and parallel-plate rheology [22] are used to quantify deformation of single cells under exposure to external stresses (compared in detail with a broader range of methods in a recent publication [23]). These methods evaluate time resolved responses to force and enable extraction of physical properties such as elastic modulus or viscosity. They suffer, however, from technically demanding and time consuming procedures that limit measurement throughput and their extendibility beyond specialized laboratories. Microfluidic based approaches developed in recent years constitute an attractive alternative [2]. They allow for robust, high throughput assessment of the ability of cells to change shape under

applied forces—their deformability—and enable thorough characterization of homogeneous and heterogeneous cell populations. Moreover, due to the ease of handling, these approaches have the potential to be implemented in biological laboratories and clinical settings.

The currently available microfluidic-based methods vary in type and magnitude of applied stress, the rate at which cells are deformed, and the way deformability is parametrized. One major class, constriction-based deformability cytometry (cDC), relies on driving cells through a constriction smaller than their diameter and measuring the time cells need to pass through the constriction [24, 5, 25, 26, 12]. The translocating cells are detected by means of optical imaging [25, 26, 12], electrical resistance measurements [24], or mechanical frequency changes of a suspended microchannel resonator (SMR) [5]. The deformability of cells is typically directly deduced from their passage time; however, in some variations of the method, additional image-based evaluation of cell deformation over time is performed and viscoelastic cell properties are extracted [25, 26]. The remaining classes of deformability cytometry employ hydrodynamic flow to induce cell deformation in a contactless manner and infer cell deformability from image-based evaluation of cell shape. One class of such contactless methods, shear flow deformability cytometry (sDC), employs shear stress and pressure gradients in a long, narrow channel to deform cells into a bullet-like shape within a few milliseconds. A prominent example of this class constitutes real-time deformability cytometry (RT-DC) [4] operating at strain rates on the order of 0.1 kHz. Another class of contactless methods, extensional flow deformability cytometry (xDC), uses an extensional flow usually associated with a cross slot microfluidic architecture. A well-established representative of this class is deformability cytometry (DC) [11], typically operating at high strain rates on the order of 10 kHz. By increasing the viscosity of the measuring buffer and lowering flow rates, xDC can be adjusted to operate at lower strain rates (<2 kHz) [27, 28]. Variabilities in the mode and timescales of operation, types of samples analyzed, and preparation conditions render it challenging to compare the published results obtained with the different deformability cytometry methods. Despite substantial work on identifying cellular structures that contribute to deformability changes with the individual methods [5, 29, 11, 15, 4], a direct comparison

of their performance is still missing.

To close this gap, we performed a highly-standardized cross-laboratory study comparing representatives of the three deformability cytometry classes: (*i*) an SMR-based cDC variant [5], (*ii*) RT-DC [4] as an example of sDC, and (*iii*) DC [11] as an example of xDC. With these methods, we evaluated deformability of human promyelocytic leukemia (HL60) cells—from the same source and passage number—in two standardized assays subjecting the cells to osmotic changes and to latrunculin B-induced actin disassembly. Our results show that the deformability is altered by osmotic changes in all presented methods. In contrast, the deformability increase due to actin disassembly is detectable with cDC and sDC, but not with the xDC method implemented in this study. The direct comparison presented here provides context for interpretation of deformability measurements performed with the different high-throughput microfluidic-based techniques for measuring cell mechanics that operate at different strain rates and stress magnitudes.

4.2 Results

4.2.1 Microfluidic-based methods to assess cell deformability

In this work we employ three representatives of the major classes of microfluidic-based techniques for measuring cell deformability—cDC, sDC, and xDC. cDC refers here to an SMR-based variant utilizing a fluidic microchannel embedded in a silicon microcantilever [5]. Close to the cantilever apex, the microchannel features a constriction smaller than the cell size (6 µm wide, 15 µm high, and 50 µm long; Figure 4.1a). Cells are driven through this constriction by a constant pressure of 1 kPa, and deform upon contact with the channel walls. The time taken by the cell to enter and pass through the constriction is assessed using changes in the resonance frequency of the microcantilever (Figure 4.1a). In cDC, cell deformability, D, is defined as the inverse of cell passage time (Figure 4.1a). The characteristic passage time of untreated HL60 cells is 23 ms (Figure 4.A.1), entailing a throughput of a few cells per second and a strain rate of 0.04 kHz.

sDC and xDC (here referring to RT-DC [4] and DC [11], respectively) both rely on hydrodynamic flow to deform cells in a contactless manner, and on high speed imaging to assess the ensuing cell deformation. Yet they operate using different channel geometries, and more importantly, different probing timescales and Reynolds numbers (see Table 4.1). The dimensionless Reynolds number ($Re = \rho v L/\eta$, where ρ is the fluid density, v the mean flow velocity, L the characteristic length of the flow system, and η the dynamic viscosity of the fluid) expresses the relative importance of inertial versus viscous forces and is equal to 0.4 for sDC and 150 for xDC. The very low Re in case of sDC ($\ll 1$) indicates a dominance of viscous forces, characteristic for the type of laminar flow called Stokes flow. xDC, in turn, operates in an inertial flow regime, where inertial forces cannot be neglected and can lead to useful effects such as cell focusing(Dino Di Carlo 2009).

In sDC, cells are driven into a funnel like constriction in a microfluidic channel where they are deformed by shear forces and pressure gradients [30, 4]) into a bullet like shape (Figure 4.1b). At the end of the ∼300 µm long channel, the steady-state cell deformation, defined as 1-circularity (Figure 4.1b), is evaluated, and constitutes cell deformability, D. Cells take a few milliseconds to travel through the channel and the strain is induced at a rate of 0.2 kHz. Typically, over 100 cells per second can be analyzed. For HL60 cells, chips with a square channel cross-section of 20 × 20 µm were used; which, together with hydrodynamic focusing implemented upstream of the deformation channel, assures that cells are not in contact with the channel walls. The stress acting on the cells during sDC measurements reaches values on the order of 1 kPa (see Estimation of stress and strain).

In xDC, cells are stretched by an extensional flow in a cross junction of a microfluidic chip (Figure 4.1c). The cells are delivered to the cross junction at several meters per second, where they are fully decelerated and deformed via inertial forces within a few microseconds. This allows for analysis rates of over 1,000 cells per second. Cell size is determined from images recorded before the cell extension, and deformability, D, is defined as the maximal aspect ratio observed in the extensional flow region. The channels of the xDC chip have a rectangular cross-section of 60 × 30 µm . Before entry to the analysis region, cells are

aligned via inertial focusing, and do not interact with the channel walls. Compared to sDC and cDC, xDC applies several-fold higher stress to the cells, and reaches a relatively high strain rate of 20 kHz (See Table 4.1 and Estimation of stress and strain Section 4.2).

The raw data obtained with all three methods is typically displayed on a scatter plot of deformability versus cell diameter (Figure 4.1). Hallmark parameters of the operation of cDC, sDC, and xDC are summarized in Table 4.1.

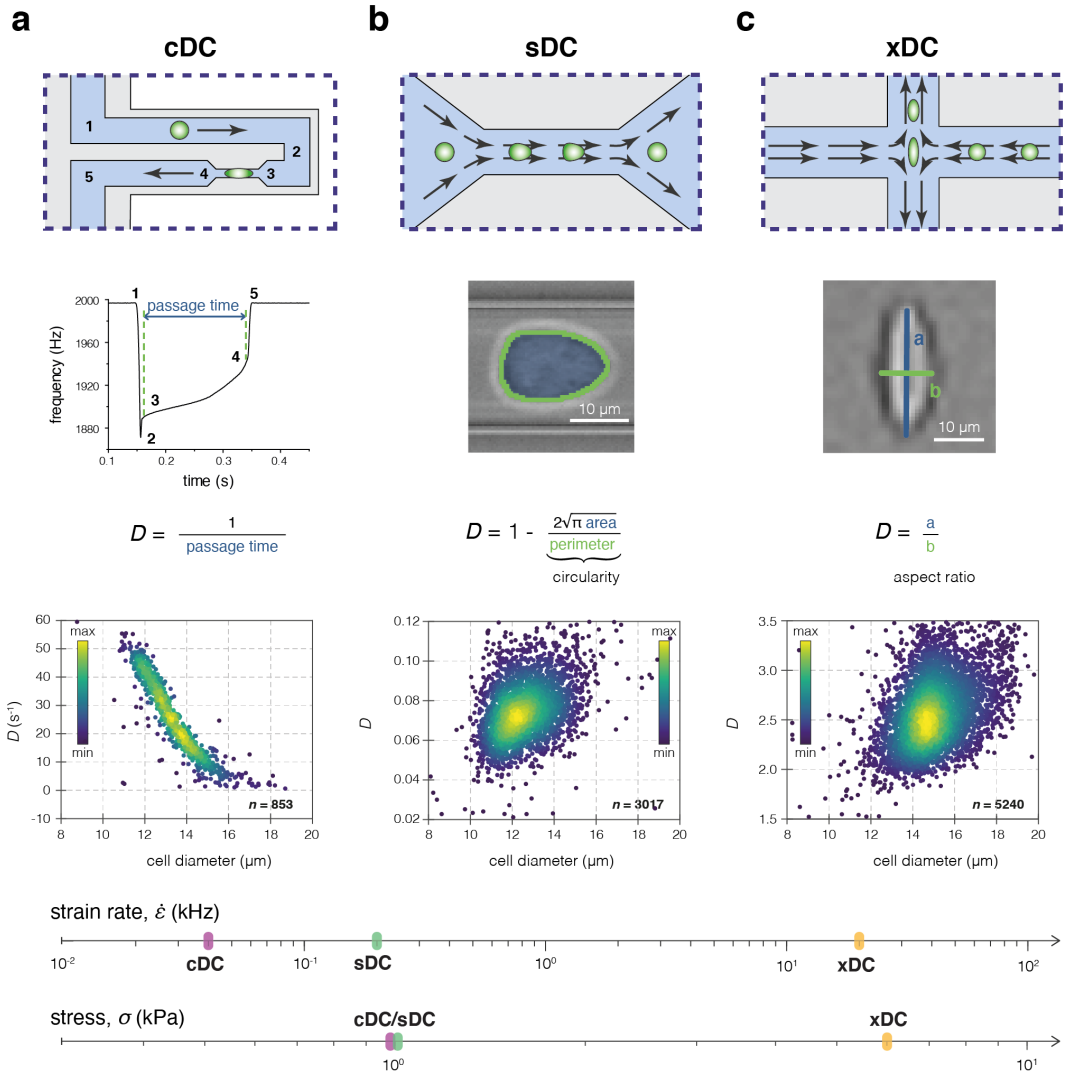

Figure 4.1: Comparison of the microfluidic-based approaches for the determination of cell deformability used in this study. (**a-c**) Operation principle of cDC (**a**), sDC

(**b**) and xDC (**c**). The upper row of each panel illustrates a schematic representation of the chip geometry used in the respective method. The middle row provides an overview of how the deformability, D, is defined for each method. The numbers 1-5 in the plot of frequency vs time correspond to the cell positions in the cDC microchannel indicated in the scheme above. In the lower row, typical scatter plots of D versus cell diameter from the respective measurements are presented. The color map corresponds to event density. The strain rate and stress applied to the cells in cDC, sDC and xDC are indicated on the corresponding axes at the bottom of the panel.

Table 4.1: Operation parameters of cDC, sDC, and xDC.

	cDC	**sDC**	**xDC**
deformability measure	passage time^{-1}	1-circularity	aspect ratio
detection	frequency shift	imaging	imaging
analysis	offline	real-time	offline
throughput (cells $\cdot$ s^{-1})	1	100	1,000
timescale of cell deformation, τ (ms)	10	1	0.01
cell contact with channel walls	yes	no	no
channel width $\times$ height (µm)	6 $\times$ 15	20 $\times$ 20	60 $\times$ 30
mean flow velocity, v (m $\cdot$ s^{-1})	0.01	0.1	3.5
viscosity of measuring buffer, η (mPa $\cdot$ s)	1	5.7	1
Re number in the measuring channel	0.1	0.4	150
mean absolute strain, $\bar{\varepsilon}$	37%	17%	24%
strain rate, $\dot{\varepsilon}$ (kHz)	0.04	0.2	20
applied stress, σ (kPa)	~ 1	~ 1	~ 6

4.2.2 Osmotic shock-induced deformability changes are detectable consistently across methods

To compare the deformability measurements among cDC, sDC, and xDC, we first performed a series of osmotic shock experiments on HL60 cells. In hyperosmotic solutions water is driven out of cells (Figure 4.2a), leading to a decrease in cell size and increased molecular crowding inside the cell, which has been linked to elevated cell stiffness [31, 32, 33, 34]. On the contrary, in hypoosmotic conditions water enters the cells to compensate for the osmolyte concentration difference, leading to cell swelling and dilution of intracellular material (Figure 4.2a), and a decrease in cell stiffness [31, 33].

To induce an osmotic shock response, the buffer's osmolarity was altered with respect to the HL60 physiological osmolarity of 300 mOsm. Hyperosmotic solutions with osmolarities ranging from 400 to 700 mOsm were prepared by adding mannitol to the measurement buffer. Hypoosmotic solutions with osmolarities of 250 and 200 mOsm were prepared by diluting the measurement buffer with water. To minimize biological batch-to-batch variability in cell properties, we shared an HL60 cell subline (HL60/S4) between the three participating laboratories at the same passage number. Cells were exposed to altered osmolarity for 10 minutes before measuring. Consistently across the methods, we observed that the hyperosmotic conditions caused a decrease in cell size and deformability, while hypoosmotic conditions caused an increase of both parameters (Figure 4.2b-d, Figures 4.A.2 and 4.A.3). Since the observed deformability response to hypoosmotic shock shows non-monotonic evolution over time (Figure 4.A.4), we excluded the hypoosmotic conditions from further analysis.

To facilitate the comparison of deformabilities measured with the individual methods, we introduced relative deformability, RD, calculated with respect to the control condition (see Online Methods and Figure 4.3). The relationships between RD and the normalized extracellular osmolarity upon hyperosmotic shock for each method were fit with an exponential curve (Figure 4.2e, Table 4.A.1) with the following formula: $RD = e^{\lambda(1-Osm/Osm_{iso})}$, where λ is the decay constant that describes the sensitivity of RD to the change in the osmolarity, Osm, normalized to the isosmotic condition, Osm_{iso}. The exponential fits provide the best

description of the obtained results, as compared to linear and power law fits (Figure 4.A.5).

Although all three methods follow the same exponential trend of decreasing RD with increasing osmolarity, the decay constants λ differ. This is confirmed by the results of pairwise F-tests, which show that there is a significant difference between the cDC and xDC curves ($F_{1,35} = 70.6$, $p = 6.5 \times 10^{-10}$), cDC and sDC curves ($F_{1,35} = 29.8$, $p = 3.9 \times 10^{-6}$), as well as between sDC and xDC curves ($F_{1,38} = 89.6$, $p = 1.5 \times 10^{-11}$). The sensitivity of the exponential decay, λ, is highest for cDC, reaching values that are 1.5 and 3 times higher than those obtained for sDC and xDC, respectively (Table 4.A.1).

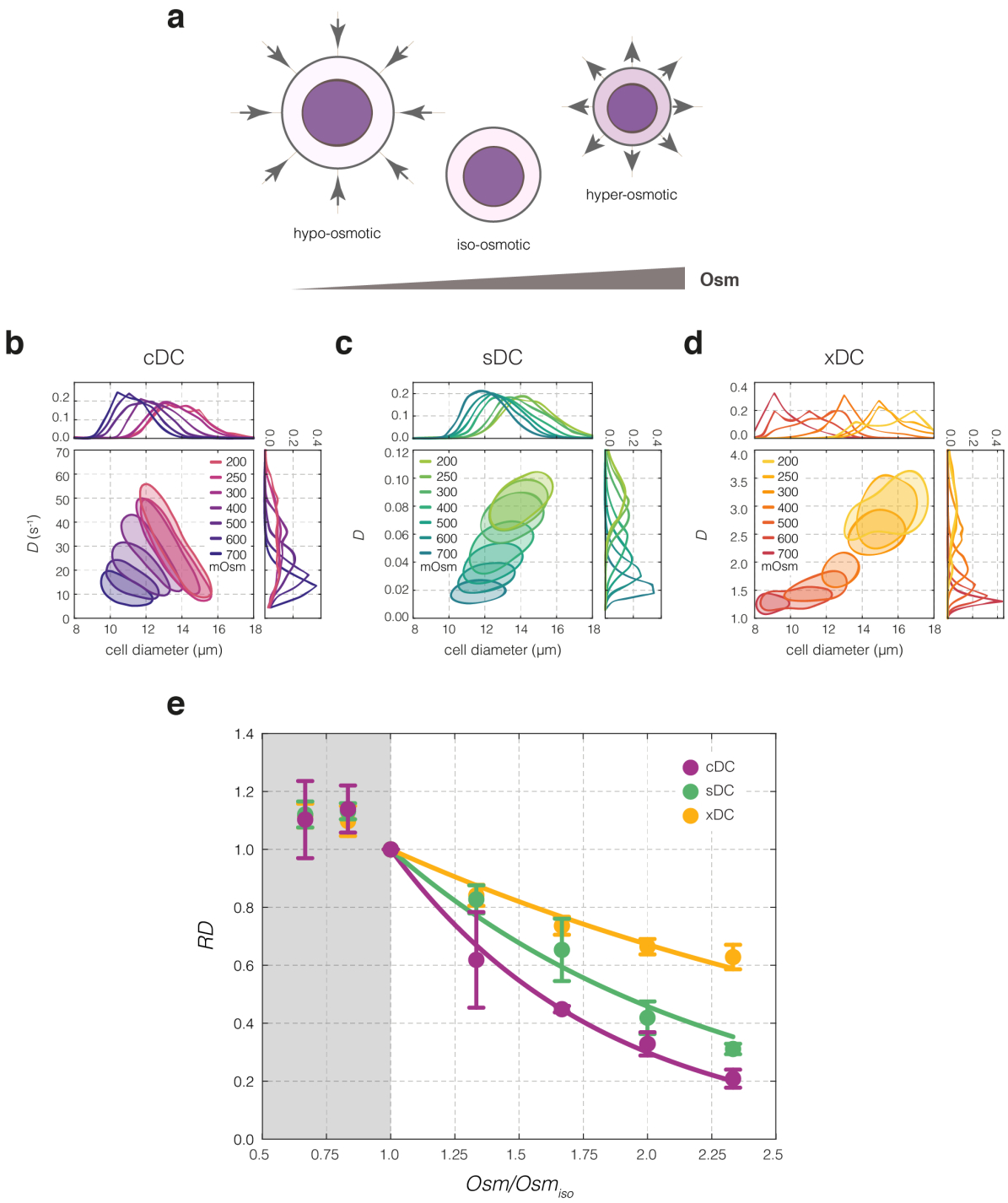

Figure 4.2: **Effects of osmolarity changes on cell deformability.** (**a**) Extracellular osmolarity when decreased beyond physiological (isoosmotic) conditions causes cell swelling and dilution of intracellular material, whereas an increase of extracellular osmolarity results

in cell shrinkage and an increase in macromolecular crowding inside the cell. Arrows indicate the direction of water flow. (**b**–**d**) Deformability changes upon osmolarity treatment observed in exemplary cDC (**b**), sDC (**c**) and xDC (**d**) experiments. 50%-density contour plots of deformability, D, versus cell diameter for HL60 cells treated with increasing osmolarity is accompanied by deformability and cell diameter histograms. (**e**) Relative deformability, RD, as a function of normalized osmolarity, Osm/Osm_{iso}, for cDC (purple), sDC (green) and xDC (yellow) measurements. Data points represent means of medians of multiple experimental replicates (n = 3, 4, and 4, for cDC, sDC, and xDC, respectively), and error bars represent standard deviation. Lines represent exponential fits to data. Hypoosmotic shock data excluded from the fitting procedure is shaded in gray.

4.2.3 Sensitivity to actin disassembly is method-dependent

To further interrogate the differences in deformability measurements between cDC, sDC, and xDC, we compared their performance in detecting actin disassembly induced by latrunculin B (LatB). The actin cytoskeleton is recognized as a prominent contributor to cell mechanics at low strains, and its destabilization with chemical agents is known to reduce cell stiffness [27, 29, 28, 26, 35]. In suspended cells, actin filaments are predominantly organized into an actin cortex—a thin, crosslinked network underlaying the plasma membrane [36]. LatB binds free actin monomers (G-actin) thereby inhibiting actin polymerization and destabilizing filamentous actin structures (F-actin), such as the actin cortex, in a dose-dependent manner [37, 38](Figure 4.3a).

We treated HL60 cells with a range of LatB concentrations (1-100 ng $\cdot$ mL^{-1}, corresponding to 2.53-253 nM), along with a DMSO vehicle control, and performed deformability measurements with cDC, sDC, and xDC (Figure 4.3b-d). As revealed by analysis of variance (ANOVA), LatB treatment had a significant effect on the cell deformability as measured with cDC ($F_{6,16} = 17.2$, $p = 3.6 \times 10^{-6}$) and sDC ($F_{6,28} = 34.3$, , $p = 1.2 \times 10^{-11}$). In contrast, the xDC measurements did not reveal significant deformability changes upon LatB treat-

ment ($F_{6,21} = 0.38$, $p = 0.89$), though a subtle deformability decrease at the highest LatB concentration (100 ng $\cdot$ mL^{-1}) was observed (Figure 4.3d-e, and Figure 4.A.6). Interestingly, when an increased flow rate was used in sDC, cell deformability reached its maximum at 50 ng $\cdot$ mL^{-1} LatB concentration and showed a decline at 100 ng $\cdot$ mL^{-1} (Figure 4.A.7a). Additionally, with increased flow rate the overall magnitude of the *RD* response showed a decrease (Figure 4.A.7b). Increase of LatB concentration beyond 100 ng $\cdot$ mL^{-1} caused decrease of deformability as observed with cDC and sDC (Figure 4.A.8), consistent with the trend observed previously with xDC [11]. For all three methods, cell size remained fairly constant at low LatB concentrations. However, at LatB concentrations of 50 ng $\cdot$ mL^{-1} (cDC) and 100 ng $\cdot$ mL^{-1} (all three methods) the determined cell size decreased slightly (Figure 4.A.9).

The change of *RD* in response to increasing LatB concentration exhibited a sigmoidal dose-response trend for cDC and sDC, while xDC results did not yield a significant fit (Figure 4.3e, Table 4.A.2). The half-maximal effective concentration, EC_{50}, reached 11.9 ng $\cdot$ mL^{-1} for cDC and 14.9 ng $\cdot$ mL^{-1} for sDC. The upper *RD* response limit was also similar for these two methods, reaching 1.46 for cDC and 1.52 for sDC. Concurrently, there was no significant difference between the obtained cDC and sDC fits ($F_{4,50} = 0.6$, $p = 0.69$), whereas significant differences were found between separate cDC and xDC curves ($F_{4,43} = 44.3$, $p = 1.0 \times 10^{-14}$), as well as between sDC and xDC curves ($F_{4,55} = 63.7$, $p = 5.3 \times 10^{-20}$).

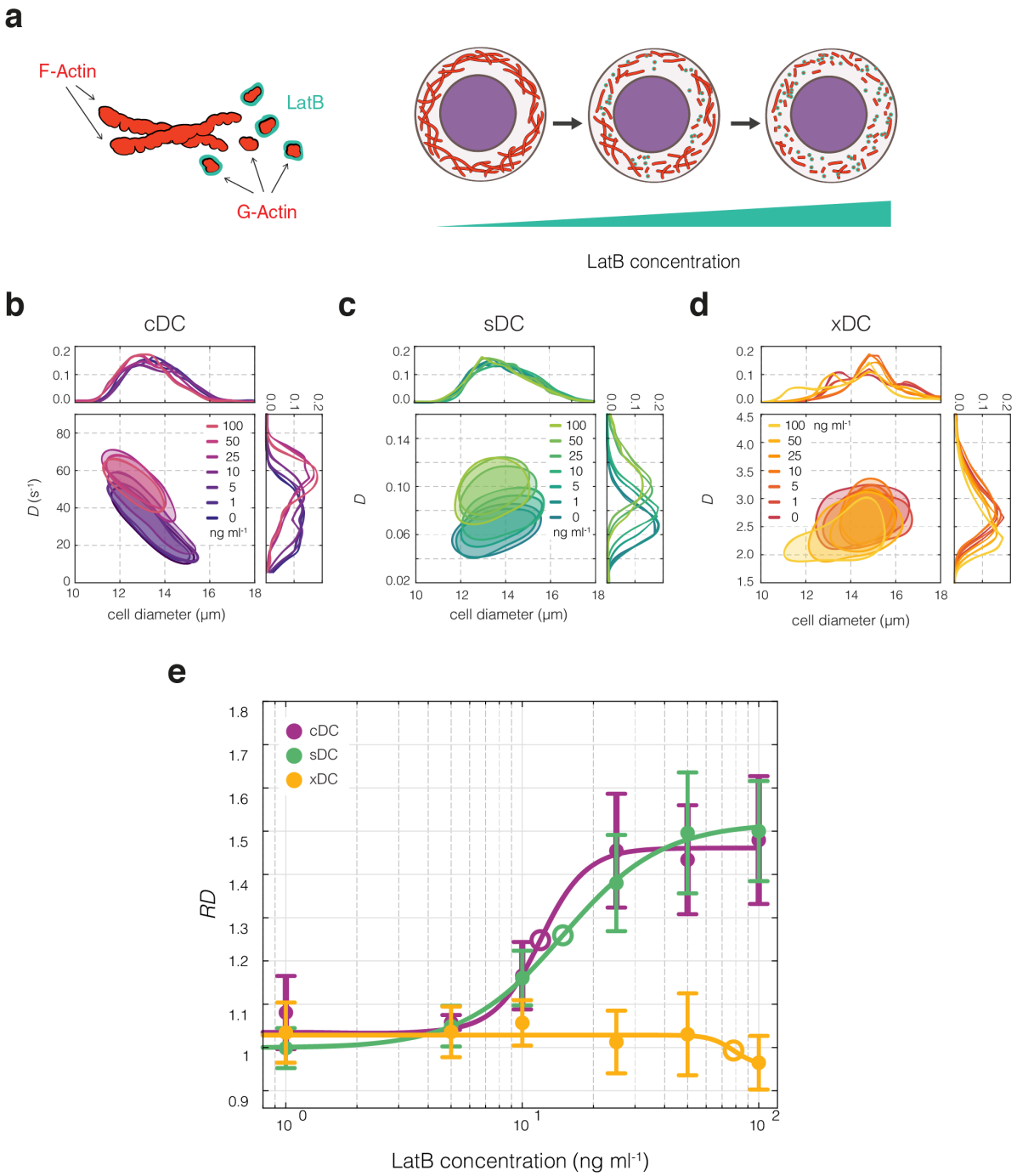

Figure 4.3: **Effects of LatB-induced actin disassembly on cell deformability.** (**a**) LatB causes dose-dependent disassembly of actin cytoskeleton by scavenging actin monomers. (**b**–**d**) Deformability changes of HL60 cells upon LatB treatment observed in exemplary cDC (**b**), sDC (**c**), and xDC (**d**) experiments. 50%-density contour plots of deformability, D,

versus cell diameter for HL60 cells treated with increasing dose of LatB are accompanied by deformability and cell diameter histograms. (**e**) Relative deformability, RD, as a function of LatB dose for cDC (purple), sDC (green) and xDC (yellow) measurements (closed circles). Data points represent means of medians of multiple experiment replicates (n = 3, 5, and 4, for cDC, sDC, and xDC, respectively), and error bars represent standard deviation. Lines are four-parameter log-logistic fits, with LatB half maximal effective concentration, EC_{50}, indicated with open circles.

4.3 Discussion

Integrating mechanical characterization into the current view of cellular behavior is paving the way towards a more comprehensive understanding of many physiological and pathological processes [17, 18] with potential clinical diagnostic value [1, 39, 3, 13, 8]). Establishment and validation of methods measuring the mechanical properties of cells is providing grounds for further developments in the field. In a recent publication [23], elastic and viscous moduli of a standardized cell line were measured with several traditional techniques, revealing a spread of obtained values over several orders of magnitude. This variability was attributed to the magnitude of applied stress and strain rate, probe size, probing length scale, and whether the cells were attached or in suspension. Here we complemented this analysis by performing a cross laboratory comparison of three widely used microfluidic cell deformability measurement techniques, cDC, sDC, and xDC. While applying different strain rates and stresses (see Table 4.1), all three methods probe whole cell deformation in a suspended cell state which reduces potential sources of variability.

All three techniques consistently measured an exponential decrease of deformability with increasing osmolarity, albeit with varying sensitivity (see Figure 4.2 and Table 4.A.1). The change in cell volume induced by osmotic shock leads to a multifaceted change in the internal structure not only within the cytoplasm, but also in the cell nucleus [40]. Although

the osmotic response can trigger changes in the relative F-actin content [41] and actin cytoskeleton structure [31], the overall changes in mechanical properties were shown to be actin-independent and attributed mostly to macromolecular crowding inside the cell [34]. We therefore conclude that the density of packing of the colloidal fraction inside the cell induces deformability changes detectable across all tested methods.

Deformability measured with cDC and sDC increased with increasing dose of the actin destabilizing drug LatB, while xDC measurements yielded no significant change in deformability upon treatment. This discrepancy can likely be attributed to the difference in applied strain rates. cDC and sDC induce strain at the rate of 0.04 and 0.2 kHz, respectively, and show an almost identical change in the measured deformabilities upon LatB treatment (see Figure 4.3 and Table 4.A.2). xDC, on the other hand, applies strain at a rate of 20 kHz, and has been previously reported to not measure significant responses to actin cytoskeletal perturbations [11], presumably due to fluidization of actin networks observed at high strains magnitudes and strain rates [42, 43]. This is further supported by the fact that adapting xDC to operate at lower strain rates enables detection of deformability changes upon disruption of actin cytoskeleton in cells [27, 28] and by the decreased dynamic range of relative deformability response when using increased flow rates in sDC (Figure 4.A.7). At high doses of LatB, corresponding to drug-induced substrate detachment observed for adherent cells [11, 38], the cells exhibit a reduction of deformability (Figure 4.A.8 and previously published xDC measurements [11]), indicating a biphasic nature of the cell mechanical response to LatB-induced actin disassembly.

In addition to measuring cell deformability, each of the presented methods features a set of distinct functionalities that expand the dimensionality of performed measurements. The SMR-based cDC provides additional parameters describing cell passage through the constriction such as entry and transit velocities, and enables a highly sensitive readout of cell buoyant mass [44, 5]. sDC stands out with its real time data processing that renders the method compatible with active sorting downstream of deformability analysis [45]. Moreover, for sDC an integrated FACS-like readout of cell and cell compartment fluorescence is available

[46], as well as a theoretical framework allowing for the extraction of Young's moduli from deformability data [30, 47]. Recently developed dynamic RT-DC enables assignment of viscosity to measured cells by analyzing the time evolution of cell deformation in the channel [48]. xDC surpasses cDC and sDC with its immense throughput. Finally, in all techniques bright-field cell images are collected and can be used for extraction of additional image-based features for further cell characterization.

In the light of our results, the use of cDC or sDC is recommended when probing cellular changes involving the actin cytoskeleton, and all three methods are equally recommended when changes in cytoplasmic packing are at play. Since cDC is the only method which involves physical contact of cells with the channel walls, it is recommend for studies in which cell friction or retention in processes such as microcirculation is of interest. xDC, in turn, was previously shown to provide a good readout of changes in structures localized deeper in the cells, such as the nucleus [11]. For further reference, a comprehensive overview of studies performed using these deformability cytometry classes is presented in Table 4.A.3.

Taken together, the comparison study presented here aids the understanding of the strengths and limitations of existing deformability cytometry methodologies, provides context for interpreting deformability measurements across various platforms, and fosters cell deformability as a powerful metric for mechanophenotyping at throughputs that mark a new era of measuring cell mechanics [49].

4.4 Methods

4.4.1 Cell culture

Cell culture. The HL60/S4 cell subline (RRID: CVCL_II77; received from Donald E. Olins and Ada L. Olins, Department of Biology, Bowdoin College, Brunswick, Maine, 04101, USA) was cultured in ATCC-modified RPMI 1640 medium (Gibco) with 1% penicillin/streptomycin (Gibco) and 10% heat-inactivated FBS (Gibco). Cells were grown at 37℃, with 5% CO_2, at densities between 10^5 and 10^6 cells $\cdot$ mL^{-1} with subculturing every second day. The cell line

stocks were shared between the three participating laboratories at the same initial passage number and were used within 10 passages upon receipt.

4.4.2 Osmotic shock

The measured osmolarity of the cell culture media and measurement buffers was 300 mOsm (Fiske 210 Micro-Sample Osmometer, Advanced Instruments, Nordwood, MA). Hyperosmotic media was prepared by adding 18.22, 36.43, 54.65, and 72.86 mg of D-Mannitol (MW: 182.172 g $\cdot$ mol^{-1}, Sigma Aldrich, St. Louis, MO) per 10 mL of the appropriate measurement buffer to obtain solutions of 400, 500, 600, and 700 mOsm, respectively. Hypoosmotic media was prepared by adding 1 part of DI H_2O to 2 or 5 parts of the measurement buffer to obtain a solution of 200 or 250 mOsm, respectively. HL60 cells at a density between 0.5–1.0 $\times$ 10^6 $\cdot$ mL^{-1} were centrifuged at 180g for 5 minutes and resuspended in osmolarity-adjusted measurement buffer. Cells were then incubated for 10 minutes at 37℃, 5% CO_2 before measurement. The subsequent deformability measurements were conducted at room temperature (22-24℃).

4.4.3 LatB treatment

Latrunculin B (MW 395.5 g mol^{-1}, Sigma Aldrich, St. Louis, MO) stock solution was prepared by dissolving the powder in DMSO at a concentration of 1 mg $\cdot$ mL^{-1} and the same stock solution was shared between the participating laboratories. The stock solution was further diluted in DMSO to 10,000x the desired concentration, to achieve equal DMSO concentration in all treatments (0.01 % v/v). Subsequently, LatB was diluted 10,000x in the appropriate measurement buffer to final LatB concentrations of 1, 5, 10, 25, 50 and 100 ng $\cdot$ mL^{-1}. HL60 cells at a density between 0.5–1.0 $\times$ 10^6 $\cdot$ mL^{-1} were harvested by centrifugation at 180g for 5 minutes, resuspended in LatB-containing solution, and incubated for 30 minutes at 37℃, 5% CO_2 prior to measurement. The subsequent deformability measurements were conducted at room temperature (22-24℃).

4.4.4 cDC measurements

The suspended microchannel resonator (SMR) utilized in this manuscript consisted of a 6 µm wide, 50 µm long, and 15 µm deep constricted fluidic channel. Device dimensions and fabrication were similar to those described previously [5]. However, the device used in this study (fabricated by CEA-Leti, France) operated via piezoceramic actuation and had a piezoresistive readout system to monitor cantilever vibration frequency, similar to other types of SMR devices published previously [50, 51]. Prior to each experiment, channel walls were passivated with 1 mg $\cdot$ mL^{-1} polyethylene glycol (PLL(20)-g[3.5]-PEG(2), SuSoS, Switzerland). The applied pressure differential driving the fluid flow through the system remained constant at 1.0 kPa for each experiment. Single cell buoyant mass and passage time were determined from changes in the resonant frequency of the microcantilever. Individual cell diameters were determined by assuming a spherical shape for each cell, with its volume obtained by combining SMR buoyant mass measurements with Coulter counter volume measurements (Multisizer 4, Beckman Coulter, Brea, CA) as described previously [5].

4.4.5 sDC measurements

The production of the polydimethylsiloxane (PDMS) chip used for sDC measurements was performed according to previously described procedures [52, 4]. The experimental procedure for sDC measurements is described in detail elsewhere [16]. In brief, cells were suspended in a viscosity-adjusted measurement buffer [phosphate saline buffer without Mg^{2+} and Ca^{2+} (PBS-) containing 0.5% (w/v) methylcellulose; adjusted in HAAKE Falling Ball Viscometer type C (Thermo Fisher Scientific, Waltham, MA) using ball number 3 to a viscosity of 15 mPa $\cdot$ s, which corresponds to a viscosity of 5.7 mPa $\cdot$ s at the measurement conditions [53]] and introduced to the device via a syringe pump. The overall flow rate during the experiments was equal to 0.04 µL $\cdot$ s^{-1} (0.01 µL $\cdot$ s^{-1} sample flow together with 0.03 µL $\cdot$ s^{-1} focusing sheath flow) unless indicated otherwise. The imaging was performed at the end of a $\sim$300 µm long channel with a 20 $\times$ 20 µm square cross-section with a high-speed camera at 2,000 frames $\cdot$ s^{-1}, and stroboscopic illumination with pulse duration $<$ 3 µs to avoid motion

blurring. The cell area and deformation were determined from cell contours in real-time by an image processing algorithm developed in house [4]. Cell diameter was calculated during offline analysis from measured surface area and defined as for a circle with an equivalent surface area. To discard events with rough or incomplete contours, the results were filtered for an area ratio between 1.00 and 1.05. Area ratio is the ratio between the area enclosed by the convex hull of the cell contour and the raw area enclosed by the contour.

4.4.6 xDC measurements

The xDC microfluidic device has been previously described [11]. Conventional soft lithography was used to fabricate the PDMS devices which were then bonded to glass slides. Cell suspensions were injected via a syringe pump at 750 µL $\cdot$ min^{-1} into the microfluidic device with the channel dimensions of 60 $\times$ 30 µm . The region surrounding the cross-slot channel was imaged with a high-speed bright-field camera at approximately 500,000 frames $\cdot$ s^{-1}, with sub-microsecond exposure time. Videos were automatically analyzed by a `MATLAB` program that measures cell diameter before deformation, and cell aspect ratio while deforming the cells. Cell diameter is defined as the minimum cell diameter in the direction perpendicular to flow $\pm$ 30° prior to the cell arrival at the cross-slot junction.

4.4.7 Relative deformability calculation

Relative deformability, RD, expresses the deformability of the treated cells, D_t, normalized to the median deformability of cells in the control condition for a given experimental series, $\widetilde{D}_{ctrl}$, according to the following formula: $RD{=}D_t/\widetilde{D}_{ctrl}$. Since the magnitude of deformability can be influenced by the cell size, RD calculations were based only on cells contained within the same 1 µm wide diameter bin most represented among all treatment and control samples for a given experimental set (see Figures 4.A.3 and 4.A.6). This procedure facilitates the assessment of the effects of a treatment on deformability, independent of the effect on cell size. The influence of the bin selection on the observed trends is illustrated in Figures 4.A.10 and 4.A.11.

4.4.8 Osmolarity data curve fitting

The response of cells to an osmotic shock is a dynamic process and, after initial cell swelling or shrinking, cells are known to undergo a regulatory volume response [54]. Using sDC, we observed the response of cells between 2 and 30 minutes after exposure to osmotic shock. In the case of the hyperosmotic shock, the deformability and cell size decrease saturated in the first few minutes, whereas for the hypoosmotic shock, deformability and cell size values initially increased, but then began to slowly return to their original values (Figure 4.A.4). Therefore, the values obtained for hypoosmotic shock at the fixed 10 minute measurement time were not included in the fitting procedure. The effect of normalized osmolarity, Osm/Osm_{iso}, on relative deformability, RD, for hypertonic conditions was fit with: (*i*) exponential, (*ii*) power law, and (*iii*) linear functions, adjusted to pass through a fixed point (1,1) representing control measurement at the isotonic osmolarity, Osm_{iso}. The fitting was performed using the nonlinear least-square `nls` function from the `stats` package in `R` (R Development Core Team). The goodness of different fits was assessed by evaluating their mean absolute residuals and Bayesian information criterion, BIC (`BIC` function in `stats` package in `R`). Exponential fit curves were compared in pairs via the F-test in `R` [55]. To account for multiple pairwise comparison across the three datasets, Bonferroni adjusted p values were calculated by multiplying p values by three [56].

4.4.9 LatB dose–response curve fitting

RD values calculated with respect to DMSO vehicle control for different LatB concentrations were used to fit a four parameter log-logistic regression curve with the following formula [57]:

$$RD([LatB],(b,c,d,e)) = \frac{d-c}{1+\exp(b(\log([LatB])-\log(e)))} \tag{4.1}$$

where $[LatB]$ is the concentration of the drug, and b, c, d, e are the fit parameters, denoting: b – the steepness of the dose-response curve, c, d – the lower and upper limits of the response, and e – the effective does EC_{50} at which half-maximum response is obtained.

The fitting was performed using `drm` function in `drc` package [57] in `R` (R Development Core Team). Fit curves were compared in pairs via the F-test in `R` [55]. To account for multiple pairwise comparison across the three datasets, Bonferroni adjusted p values were calculated by multiplying p values by three [56].

4.A Appendix

Table 4.A.1: **LatB curve fitting** The decay constants, λ, for the exponential curve fit to the relative deformability versus normalized osmolarity data for hyperosmotic shock obtained with cDC, sDC, and xDC. Fits were performed on medians from $n = 3$, 4, and 4 independent experiments, for cDC, sDC, and xDC, respectively. The fitted λ values are reported together with 95 % confidence intervals, CI, and associated p-values from two-sided t-tests for this parameter

	cDC	**sDC**	**xDC**
λ	1.206 95% CI [1.065, 1.366], $t(16) = 17.26$, $p = 9.14 \times 10^{-12}$	0.780 95% CI [0.695, 0.873], $t(19) = 18.14$, $p = 1.86 \times 10^{-13}$	0.397 95% CI [0.363, 0.433], $t(19) = 24.02$, $p = 1.12 \times 10^{-15}$

Table 4.A.2: **Osmolarity curve fitting** Fit parameters for the four-parameter log-logistic regression fit to the relative deformability versus LatB concentration data obtained with cDC, sDC, and xDC. Fits were performed on medians from $n = 3$, 5, and 4 independent experiments, for cDC, sDC, and xDC, respectively. The fitted values are reported together with 95% confidence intervals, CI, and associated p-values from two-sided t-tests for each parameter.

	cDC	**sDC**	**xDC**
b (slope)	-4.47 mL $\cdot$ ng^{-1} 95% CI [-14.13, 5.18] $t(19) = -0.97$ $p = 0.34$	-2.06 mL $\cdot$ ng^{-1} 95% CI [-3.20, -0.94] $t(31) = -3.74$ $p < 2.20 \times 10^{-16}$	8.71 mL $\cdot$ ng^{-1} 95% CI [-72.57, 89.99] $t(24) = 0.22$ $p = 9.03 \times 10^{-5}$
c (lower limit)	1.04 95% CI [0.97, 1.10] $t(19) = 35.31$ $p < 2.20 \times 10^{-16}$	1.00 95% CI [0.95, 1.05] $t(31) = 38.13$ $p < 2.20 \times 10^{-16}$	0.96 95% CI [0.54, 1.38] $t(24) = 4.69$ $p = 9.03 \times 10^{-5}$
d (upper limit)	1.46 95% CI [1.38, 1.53] $t(19) = 39.71$ $p < 2.20 \times 10^{-16}$	1.52 95% CI [1.44, 1.60] $t(31) = 37.73$ $p < 2.20 \times 10^{-16}$	1.03 95% CI [1.00, 1.06] $t(24) = 77.72$ $p < 2.20 \times 10^{-16}$
e ($\mathbf{EC_{50}}$)	11.92 ng $\cdot$ mL^{-1} 95% CI [6.82, 17.01] $t(19) = 4.90$ $p = 9.93 \times 10^{-5}$	14.85 ng $\cdot$ mL^{-1} 95% CI [9.62, 20.07] $t(31) = 5.80$ $p < 2.20 \times 10^{-16}$	78.24 ng $\cdot$ mL^{-1} 95% CI [-273.0, 430] $t(24) = 0.46$ $p = 0.65$

Table 4.A.3: **Deformability cytometry demonstrations** Demonstrated applications of deformability cytometry methodologies. Summary of studies employing different types of deformability cytometry to investigate various processes in cell lines and in primary tissue samples.

method	demonstrated biological applications
cDC	cytoskeleton perturbations [24, 5, 58, 25, 26, 12], chromatin reorganization [25], nuclear envelope alteration [25, 59], inflammation mediation [12], leukostasis [12], cancer cell discrimination [26, 60], cancer cell invasion potential [60], endothelial-mesenchymal transition [61], osmotic stress [58], protein synthesis inhibition [58], cell cycle progression [58], neutrophil differentiation [59], oxidative damage of erythrocytes [62], circulating tumor cells and blood cells discrimination [63, 61]
sDC	cytoskeleton perturbations [64, 29, 4], cell cycle progression [4, 46], blood cell type discrimination [48, 4, 13], cancer malignancy [64, 65], erythrocyte pathologies [66, 13], leukocyte activation [9, 67, 13], leukemia subtypes discrimination [13], stem cell differentiation [68, 16, 69], characterization of hematopoietic stem and progenitor cells [70], characterization of rod photoreceptors [71], yeast dormancy [72], viral infection of a human cell line [68], ability to pass through microcirculation [73]
xDC	cytoskeleton perturbation (at low probing rates) [27, 28], chromatin reorganization [74], nuclear envelope alteration [74], stem cell differentiation [11, 15, 74], characterization of blood cells [61] and cells in pleural fluids [11, 8], cancer malignancy [8], leukocyte activation [75, 11], heat-treated erythrocytes [76]

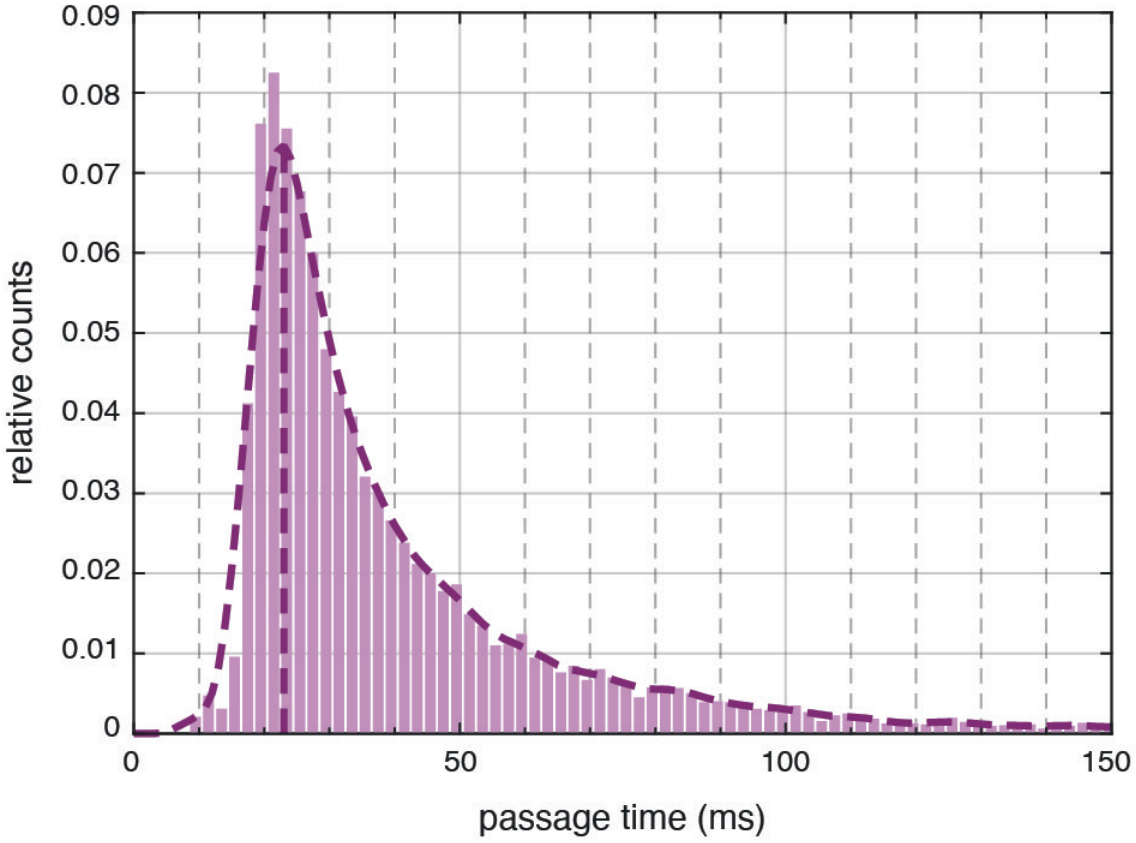

Figure 4.A.1: **Distribution of passage times measured with cDC for untreated HL60 cells.** Bars represent binned data of control HL60 cells pulled from 10 experiments (total cell number, n = 9,734). Dashed curve represents Kernel density estimation (KDE) of probability distribution with vertical line at the most represented value equal to 23 ms.

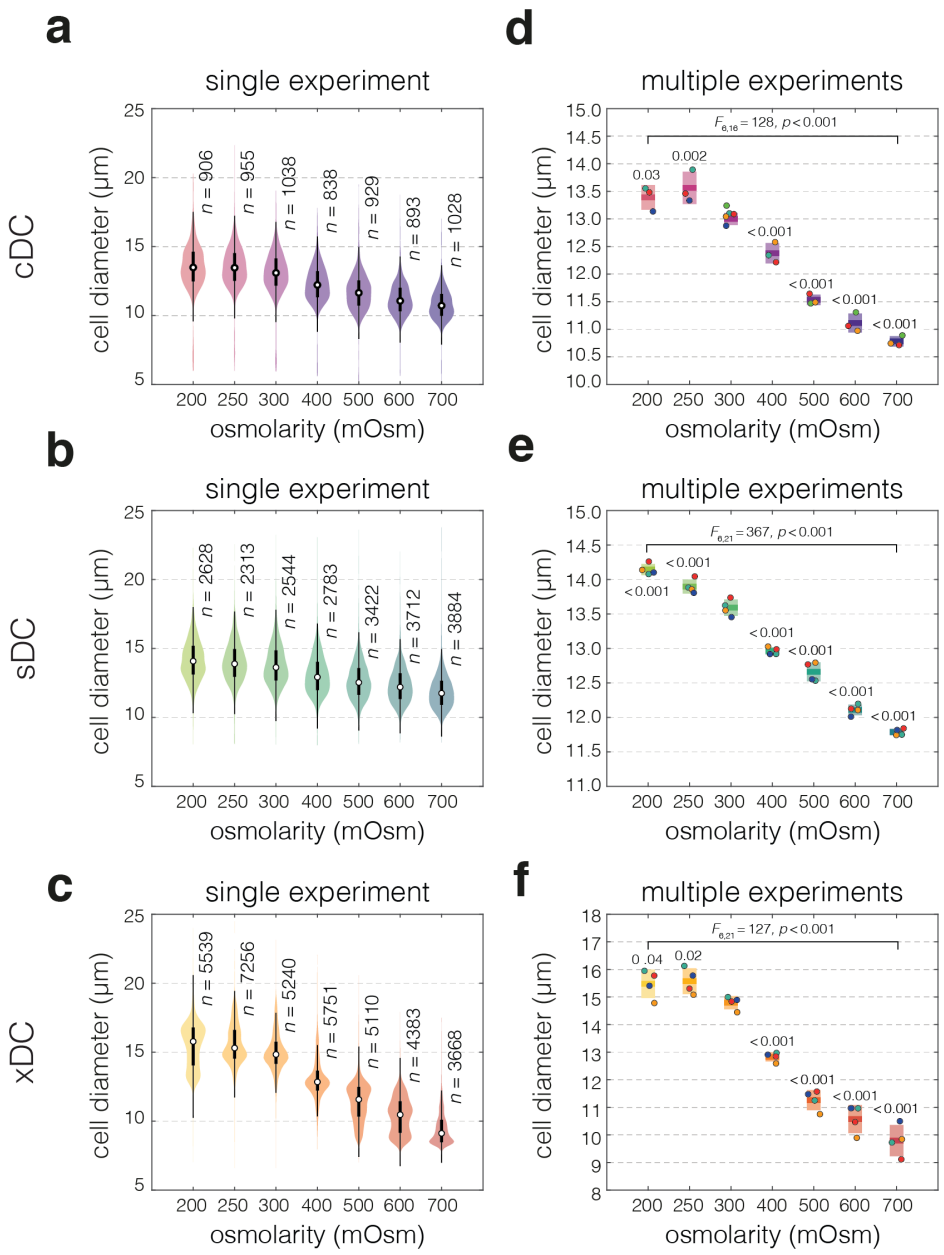

Figure 4.A.2: **Cell diameter of HL60 cells exposed to different osmotic shock conditions.** (**a**–**c**) Violin plots of cell diameter in a single experiment as measured by cDC (**a**), sDC (**b**) and xDC (**c**). Black boxes extend from 25$^{\text{th}}$ to 75$^{\text{th}}$ percentiles, with a dot at the median, whiskers indicate 1.5x IQR (interquartile range). (**d**–**f**) Summary of median cell diameter values obtained in all experiment series with cDC (**d**), sDC (**e**) and xDC (**f**). Data points correspond to medians of individual experiments (n = 3, 4 and 4, for cDC, sDC and

xDC, respectively). Conditions measured in the same experimental series are color-coded. Boxes span 2x standard deviation with a line at the mean of all medians. In (**d**–**f**) statistical significance of overall differences among mean cell sizes at different osmolarities was tested using analysis of variance (ANOVA) and its result is shown on top of the horizontal line overarching all conditions. The p-values reported above each box come from comparison of the given treatment to the control condition (300 mOsm) obtained through post hoc analysis using two-sided pairwise t tests for multiple comparison with Benjamin-Hochberg p-value adjustment.

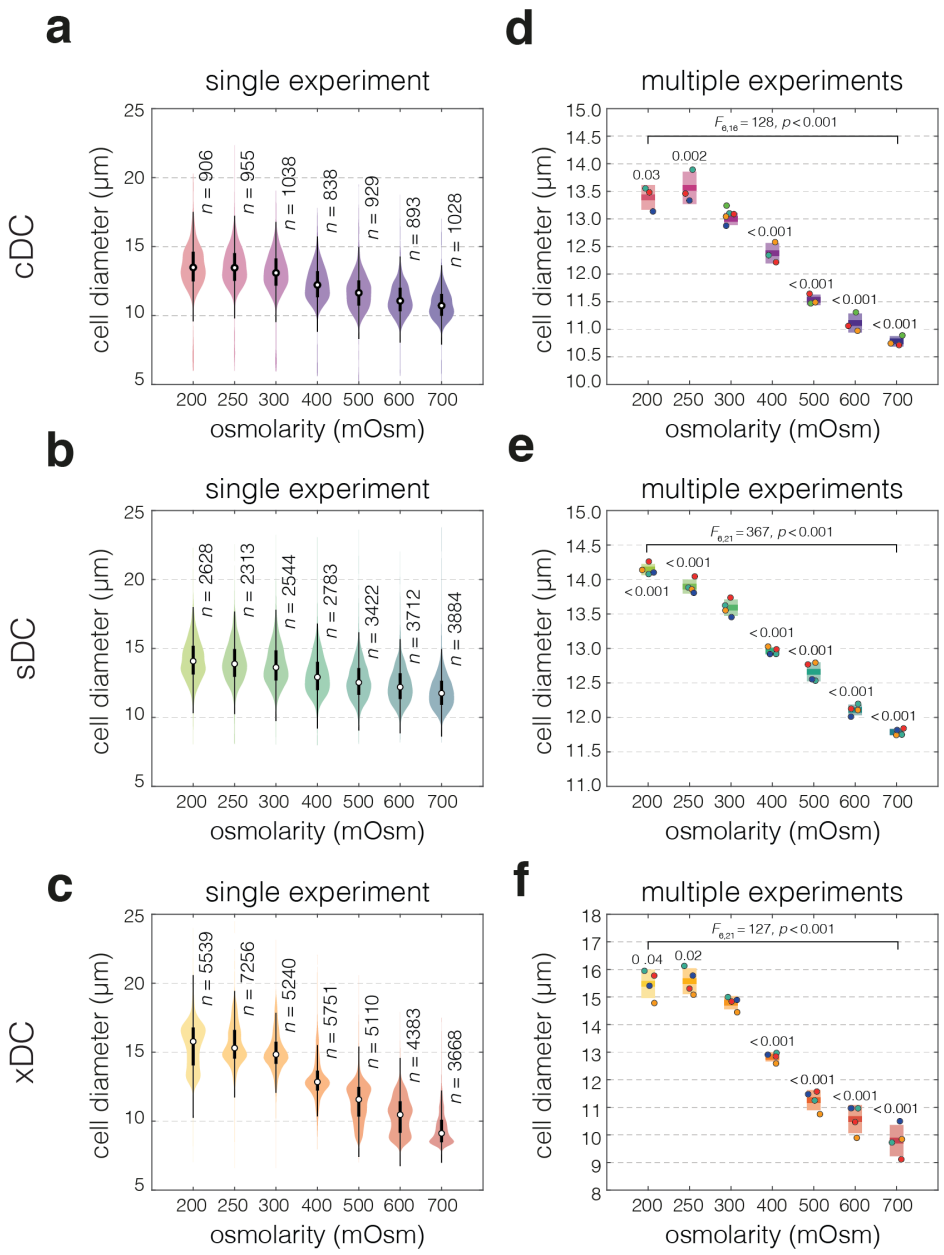

Figure 4.A.3: **Visualization of bin selection and data processing for osmolarity experiments.** (**a**–**c**) 50%-density contour plots of deformability vs cell diameter for an exemplary experiment on HL60 cells subjected to different osmolarity conditions. The contour plots are accompanied by deformability and cell diameter histograms for cDC (**a**), sDC (**b**), and xDC (**c**). The most represented 1-µm wide diameter bins used for relative deformability, *RD*, calculations and and the corresponding deformability histograms are outlined in grey.

(**d**–**f**) Jitter plots showing distribution of *RD* from cDC (**d**), sDC (**e**), and xDC (**f**) measurements for a single experiment. Boxes extend from 25^{th} to 75^{th} percentiles, with a dot at the median, whiskers indicate 1.5× IQR (interquartile range) and each data point corresponds to an individual cell. (**g**–**i**) Summary of *RD* values obtained in all experimental series with cDC (**g**), sDC (**h**) and xDC (**i**). Data points correspond to medians of every experiment and conditions measured in same experimental series are color-coded. Boxes span 2× standard deviation with a line at the mean of all medians. (**j**) Number of events in the selected 1-µm wide diameter bin for each condition and method. (**k**) Events selected within the 1-µm wide diameter as a percentage of all events measured. In **j** and **k**, the boxes span 2× standard deviation with a line at the mean. In **g-k**, the statistics have been calculated for $n = 3$, 4 and 4 independent measurement replicates, for cDC, sDC and xDC, respectively.

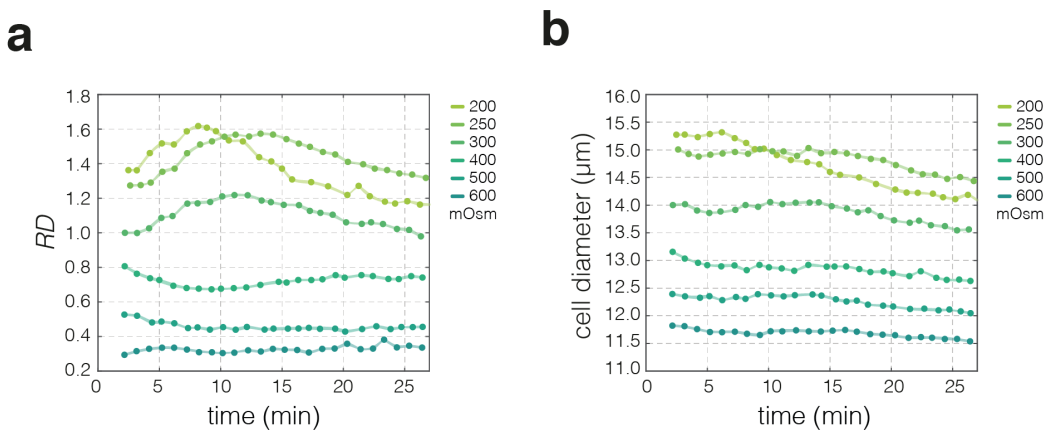

Figure 4.A.4: **Time-resolved effect of osmotic shock on HL60 deformability and size as measured by sDC. (a–c)** The changes in HL60 deformability, D (**a**), and cell diameter (**b**) over time after exposure to medium with altered osmolarity as measured by sDC. The experiments were performed in 30 × 30 µm channels at a flowrate of 0.16 µL · s^{-1}. Data points represent medians of consecutive measurements taken at different times after the exposure to altered osmolarity medium. On average 3,000 events (and not less than 1,800) are analyzed for each data point.

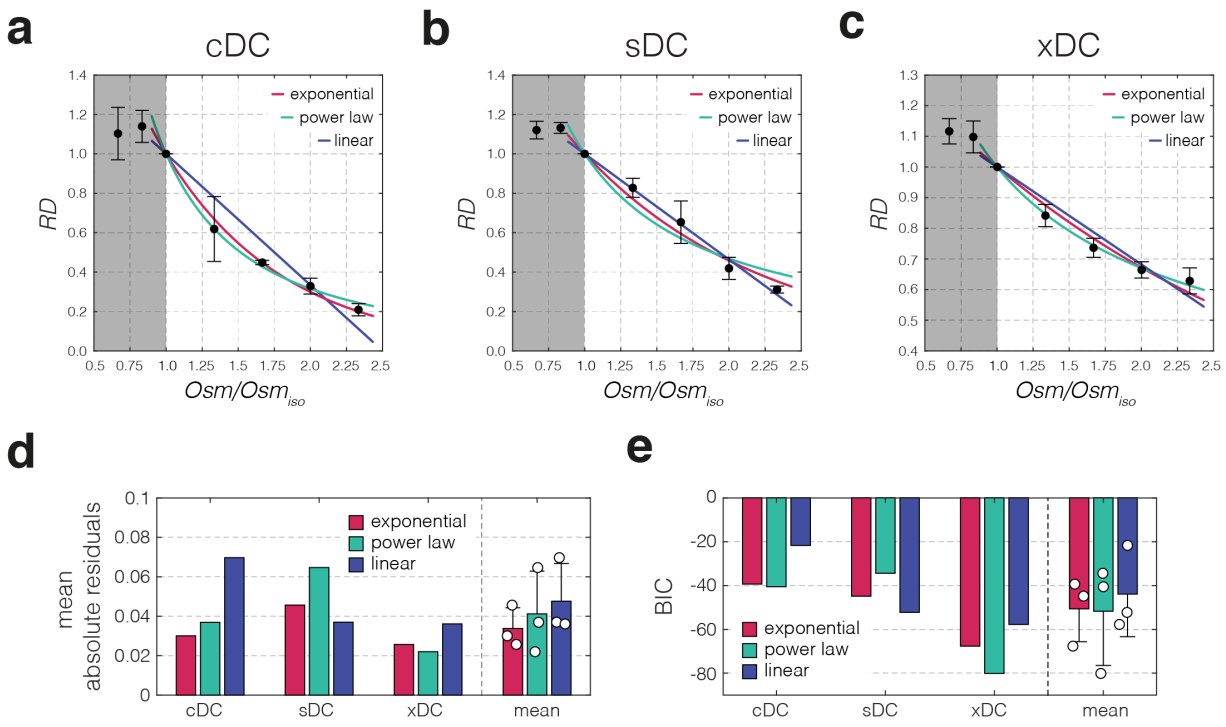

Figure 4.A.5: **Fitting of the relation between osmolarity and relative deformability for hyperosmotic shock data.** (**a-c**) Exponential (red), power law (green) and linear (blue) fits to relative deformability, RD, vs osmolarity data obtained with cDC (**a**), sDC (**b**) and xDC (**c**). Data points in **a-c** represent means of medians of multiple experimental replicates (n = 3, 4, and 4, for cDC, sDC, and xDC, respectively), error bars represent standard deviation. (**d-e**) Bar graphs of mean absolute residuals (**d**) and Bayesian information criterion (BIC) (**e**), that assess the quality of different fits. Values estimated for each method, as well as mean of values for all methods (n = 3) for given fit function, are presented. The error bars on the mean plots represent standard deviation. Mean absolute residuals give an information on how much the values predicted by the fitted function deviate from the experimental data. Lower values of residuals indicate better agreement of experimental data with proposed function. In case of BIC, lower values indicate a better fit.

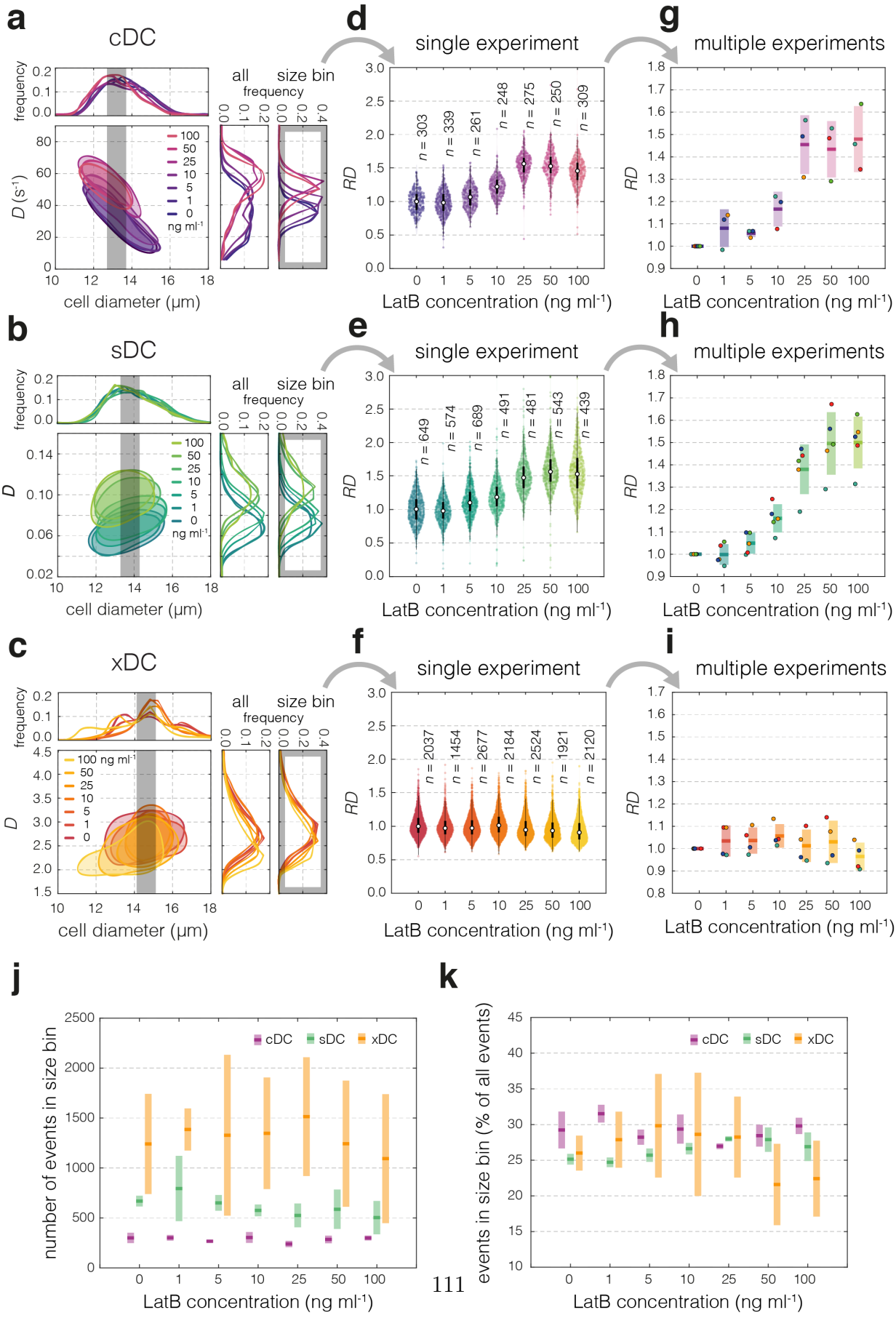
a
cDC
frequency
all
size bin
frequency
D (s⁻¹)
100
50
25
10
5
1
0
ng ml⁻¹
cell diameter (µm)
b
sDC
D
cell diameter (µm)
c
xDC
100 ng ml⁻¹
cell diameter (µm)
d
single experiment
RD
n = 303
n = 339
n = 261
n = 248
n = 275
n = 250
n = 309
LatB concentration (ng ml⁻¹)
e
single experiment
n = 649
n = 574
n = 689
n = 491
n = 481
n = 543
n = 439
LatB concentration (ng ml⁻¹)
f
single experiment
n = 2037
n = 1454
n = 2677
n = 2184
n = 2524
n = 1921
n = 2120
LatB concentration (ng ml⁻¹)
g
multiple experiments
LatB concentration (ng ml⁻¹)
h
multiple experiments
LatB concentration (ng ml⁻¹)
i
multiple experiments
LatB concentration (ng ml⁻¹)
j
number of events in size bin
cDC
sDC
xDC
LatB concentration (ng ml⁻¹)
k
events in size bin (% of all events)
cDC
sDC
xDC
LatB concentration (ng ml⁻¹)

Figure 4.A.6: **Visualization of bin selection and data processing for LatB treatment experiments.** (**a**–**c**) 50%-density contour plots of deformability vs cell diameter for an exemplary experiment on HL60 cells treated with increasing concentration of LatB. The contour plots are accompanied by deformability and cell diameter histograms for cDC (**a**), sDC (**b**), and xDC (**c**). The most represented 1 µm wide diameter bins used for relative deformability, RD, calculations and the corresponding deformability histograms are outlined in grey. (**d**–**f**), Jitter plots showing distribution of RD from cDC (**d**), sDC (**e**), and xDC (**f**) measurements for a single experiment. Boxes extend from 25^{th} to 75^{th} percentiles, with a dot at the median, whiskers indicate 1.5x IQR (interquartile range) and each data point corresponds to an individual cell. (**g**–**i**), Summary of RD values obtained in all experimental series with cDC (**g**), sDC (**h**) and xDC (**i**). Data points correspond to medians of every experiment and conditions measured in the same experimental series are color-coded. Boxes span 2x standard deviation with a line at the mean of all medians. (**j**) Number of events in the selected 1 µm wide diameter bin for each condition and method. (**k**) Events selected within the 1 µm wide diameter as a percentage of all events measured. In (**j**) and (**k**) the boxes span 2x standard deviation with a line at the mean. In (**g-k**), the statistics have been calculated for $n = 3$, 5 and 4 independent measurement replicates, for cDC, sDC and xDC, respectively.

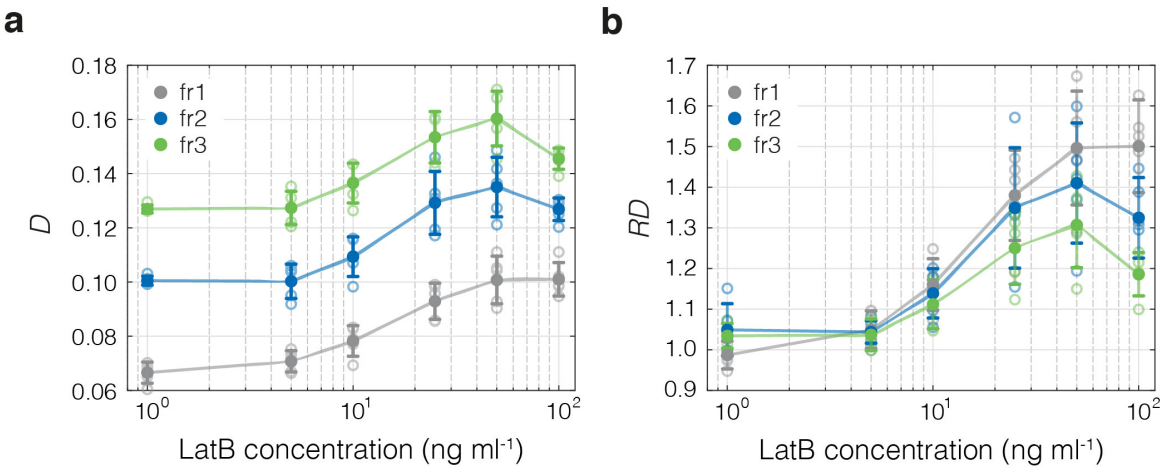

Figure 4.A.7: **Dose-response to LatB treatment measured with sDC at three different flow rates.** Deformability, D (**a**), and relative deformability, RD (**b**), as a function of LatB concentration at three different flowrates (fr1 = 2.4 µL · min^{-1}, fr2 = 4.8 µL · min^{-1}, and fr3 = 7.2 µL · min^{-1}). The different flowrates are color-coded as indicated in the figure legend (fr1 – gray, fr2 – blue, fr3 – green). Open circles indicate medians of individual measurements, lines connect means of measurement replicates for each flowrate ($n = 5$), error bars correspond to standard deviation of the mean distributions. Bin-selected data was used.

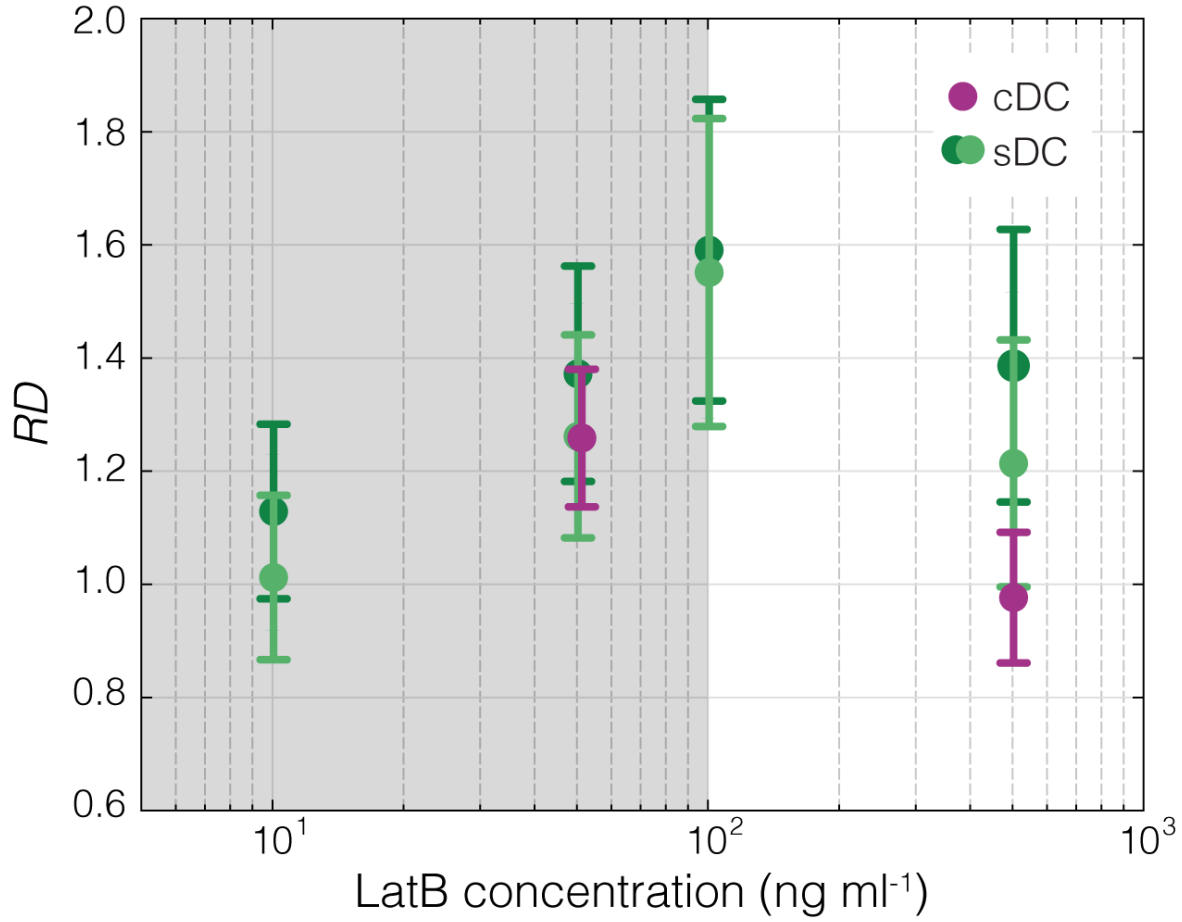

Figure 4.A.8: **Response to high LatB concentrations measured with cDC and sDC.** The graph shows relative deformability, RD, as a function of LatB concentration. Dots represent medians of individual measurements. Error bars represent median absolute deviation. Bin-selected data was used. One measurement series was performed using cDC (purple, from left to right $n = 296$ and 271 analyzed cells in the selected size bin per data point) and two measurement series were performed using sDC (bright and dark green, from left to right $n = 656$, 537, 420, 550, and $n = 734$, 615, 336, 541 analyzed cells in the selected size bin, for bright and dark green data points, respectively). The concentration range used for main analysis is shaded in gray.

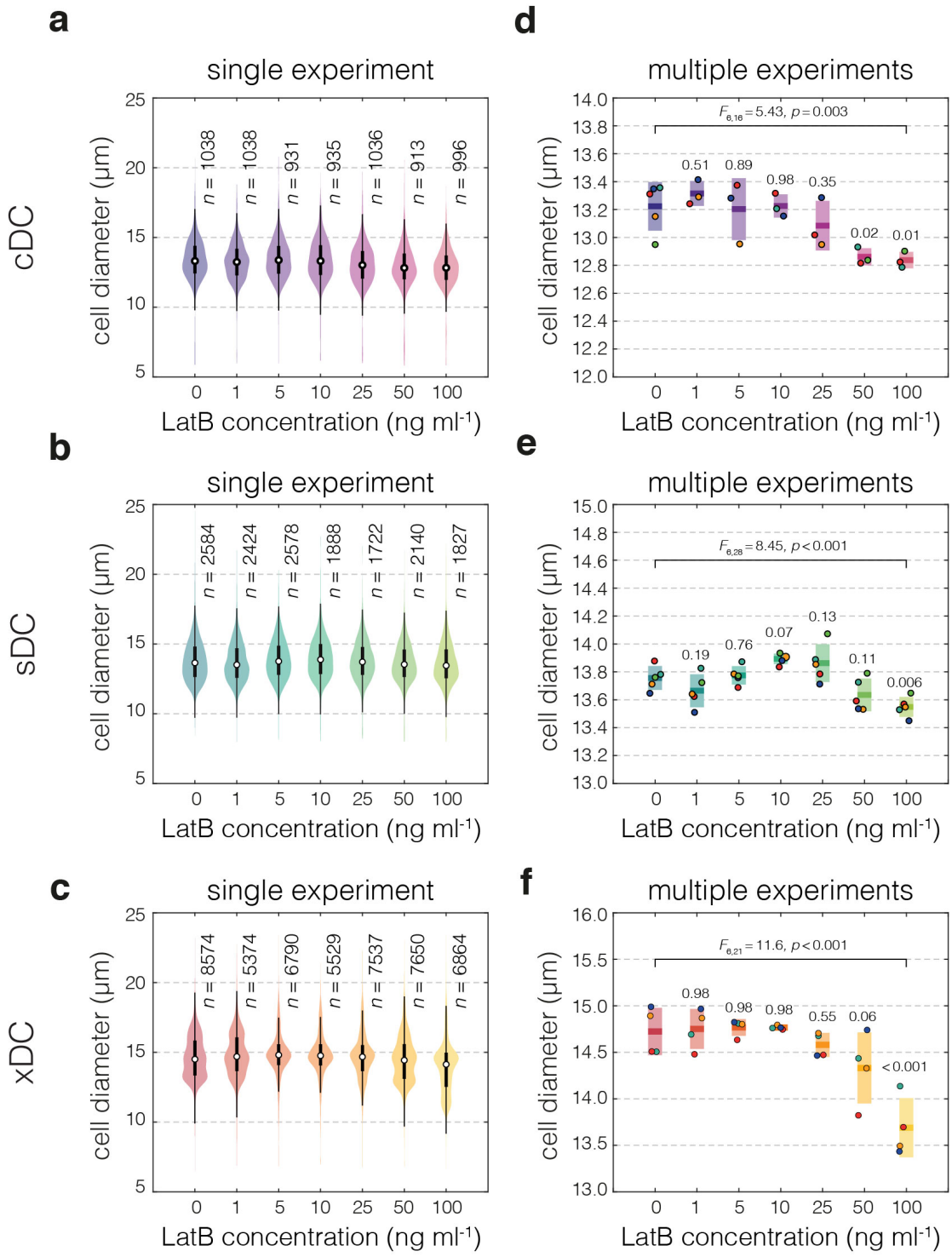

Figure 4.A.9: **Cell diameter of HL60 cells treated with different concentrations of LatB. (a–c)** Violin plots of cell diameter in a single experiment as measured by cDC

(**a**), sDC (**b**) and xDC (**c**). Black boxes extend from 25^{th} to 75^{th} percentiles, with a dot at the median, whiskers indicate 1.5x IQR (interquartile range). (**d**–**f**) Summary of median cell diameter values obtained in all experiment series with cDC (**d**), sDC (**e**) and xDC (**f**). Data points correspond to medians of individual experiments (n = 3, 5 and 4, for cDC, sDC and xDC, respectively). Conditions measured in same experimental series are color-coded. Boxes span 2x standard deviation with a line at the mean of all medians. In (**d**–**f**) statistical significance of overall differences among mean cell sizes at different concentrations was tested using analysis of variance (ANOVA) and its result is shown on top of the horizontal line overarching all conditions. The p-values reported above each box come from comparison of the given treatment to the control condition obtained through post hoc analysis using pairwise two-sided t-tests for multiple comparisons with Benjamin-Hochberg p-value adjustment.

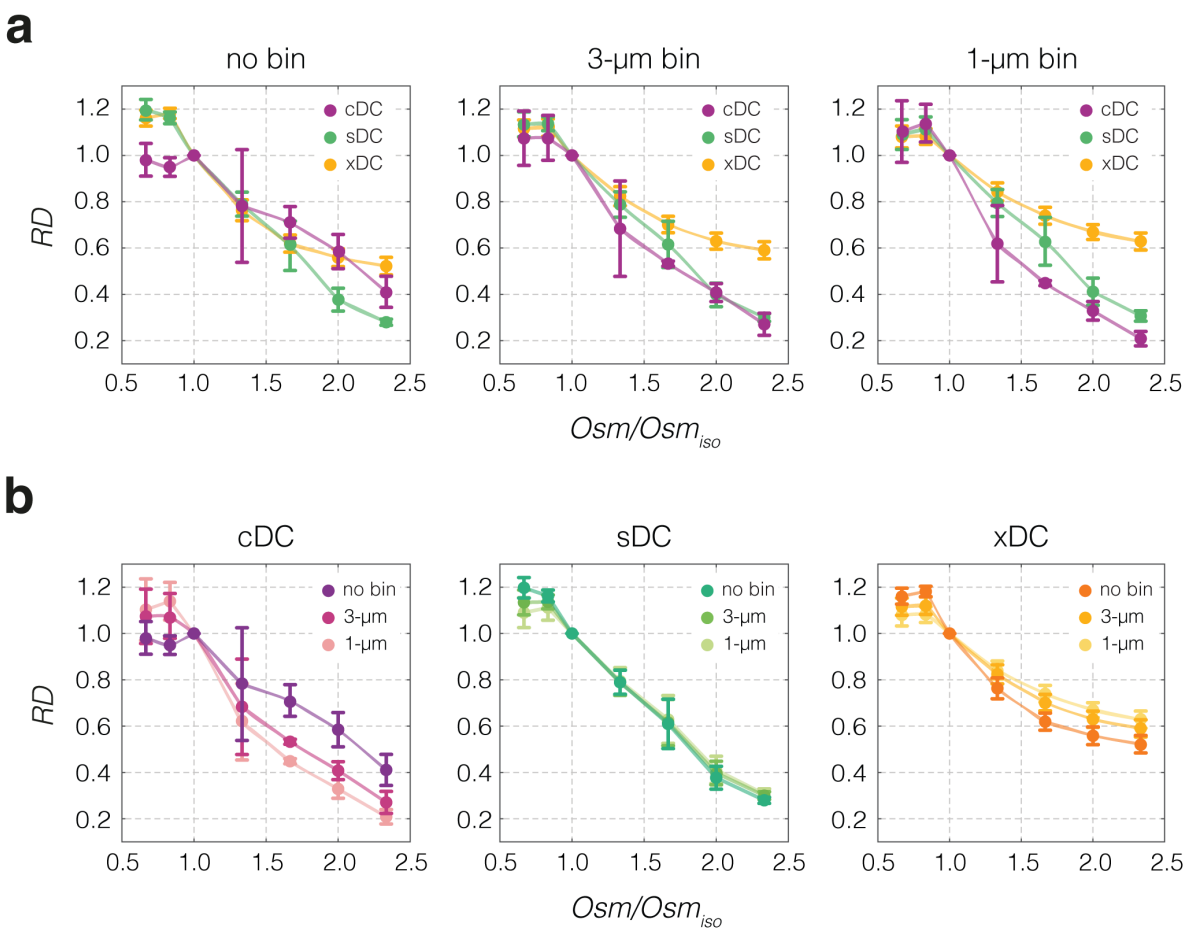

Figure 4.A.10: **The influence of size bin selection on relative deformability response to osmotic shock.** For all three methods *RD* was calculated for either all data, 3-µm wide cell diameter bin or 1-µm wide cell diameter bin. For the ease of comparison, the data is grouped based on binning strategy and all three methods are plotted together (**a**), or the data is grouped by method and all binning strategies are compared (**b**). The lines connect the data points representing means of medians from measurement replicates ($n = 3$, 4, and 4, for cDC, sDC, and xDC, respectively). Error bars present the standard deviation of the medians.

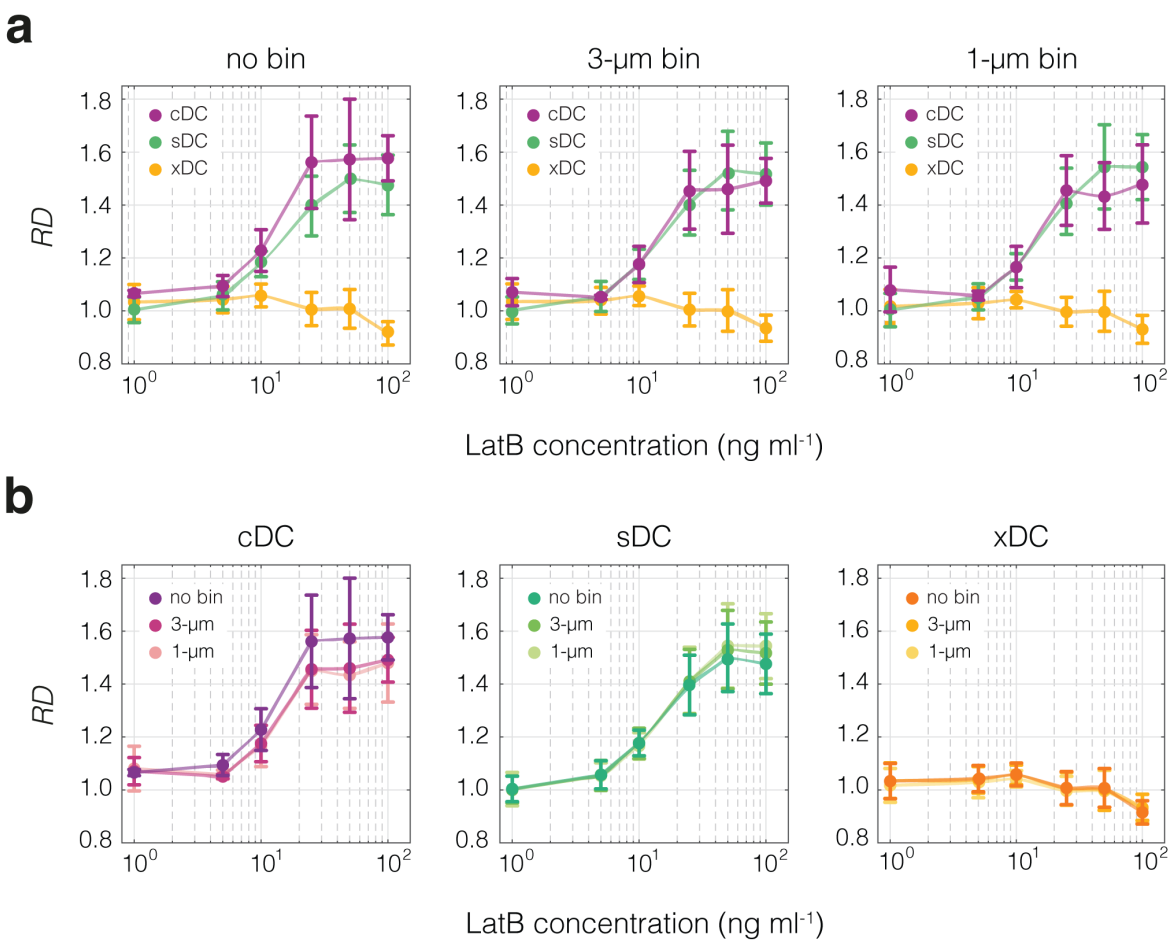

Figure 4.A.11: **The influence of size bin selection on relative deformability response to LatB treatment.** For all three methods *RD* was calculated for either all data, 3-µm wide cell diameter bin or 1-µm wide cell diameter bin. For the ease of comparison, the data is grouped based on binning strategy and all three methods are plotted together (**a**), or the data is grouped by method and all binning strategies are compared (b). The lines connect the data points representing means of medians from measurement replicates ($n = 3$, 5, and 4, for cDC, sDC, and xDC, respectively). Error bars present the standard deviation of the medians.

4.A.1 Estimation of stress and strain

4.A.1.1 Rotational symmetry of deformed cells

During a microfluidic deformation experiment, a spherical cell adapts a three-dimensional deformed shape: a prolate ellipsoid in case of cDC and xDC, and a bullet-like shape in case of sDC (Figure 4.A.12). Depending on the geometry of the microfluidic system used, the obtained shape can be rotationally symmetric with respect to the angle ϕ about the rotation axis x aligned with the longest shape dimension, or rotationally asymmetric. In case of cDC, the measurement channels used were 6 µm wide and 15 µm high which resulted in a deformation into a rotationally asymmetric ellipsoid (Figure 4.A.12a). sDC channels had a square cross-section of 20 µm × 20 µm resulting in a rotationally symmetric bullet-like shape (Figure 4.A.12b). In xDC, the channels were 60 µm wide and 30 µm high. The extensional flow comes from both sides along the y-axis and exits the cross-junction towards the x-direction causing the cells to compress in y, and extend in x and z in an asymmetric way. This resulted in an ellipsoid that was not rotationally symmetric about the x axis (Figure 4.A.12c).

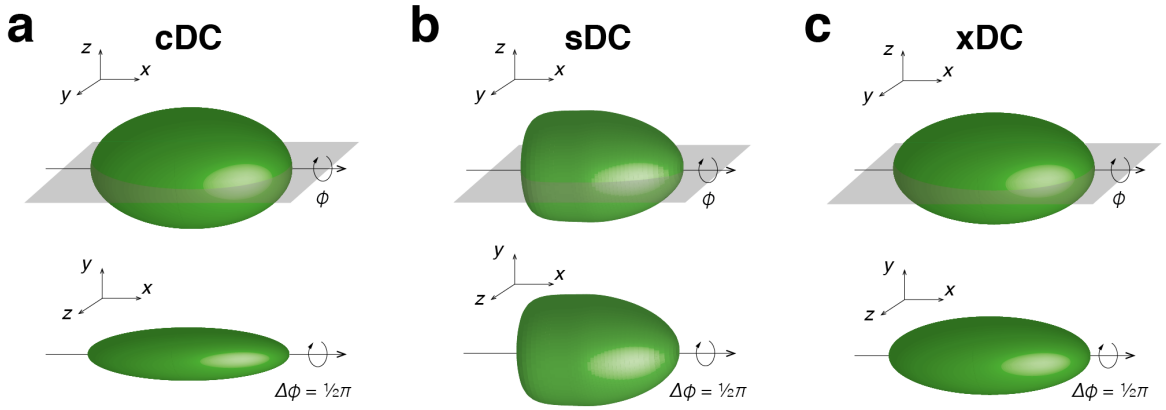

Figure 4.A.12: **The 3D shapes obtained during microfluidic deformation of spherical objects and their rotational views.** (**a-c**) 3D projections of shapes obtained during cDC (**a**), sDC (**b**) and xDC (**c**) measurements presented from two rotational angles ϕ. The xyz-directions are given for reference in the upper left corner of each image. The gray

transparencies in the upper row indicate xy-plane.

4.A.1.2 Strain estimation

We define strain, ε, experienced by the cell as a deviation of the local cell radius, r, from the radius of an undeformed cell, r_0, along the polar angle θ within a plane of interest at a given rotation angle ϕ about the rotation axis x aligned with the longest shape dimension (as depicted in Figure 4.A.12):

$$\varepsilon(\theta, \phi) = \frac{r(\theta, \phi) - r_0}{r_0} \tag{4.A.1}$$

The local strains in xy-plane, ε_{xy}, and xz-plane, ε_{xz}, can be formalized as follows

$$\varepsilon_{xy}(\theta) = \varepsilon(\theta, 0) \tag{4.A.2}$$

$$\varepsilon_{xz}(\theta) = \varepsilon(\theta, \frac{\pi}{2}) \tag{4.A.3}$$

The maximum absolute strain experienced by the cell, $\varepsilon_{\max}$, is defined as

$$\varepsilon_{\max} = \max(|\varepsilon(\theta, \phi)|) \tag{4.A.4}$$

while the mean absolute strain, $\overline{\varepsilon}$, experienced over all polar angles $\theta \in (-\pi,\ \pi)$ at every rotation angle $\phi \in (-\pi,\ \pi)$ can be denoted as

$$\overline{\varepsilon} = \langle|\varepsilon(\theta, \phi)|\rangle \tag{4.A.5}$$

For cDC, r_0 is estimated for each cell from the measured cell volume as described in Methods section, and $r(\theta, \phi)$ is calculated assuming volume conservation and a deformation into an ellipsoid with the maximum principal axes length in y and z determined by the width (6 µm) and height (15 µm) of the microconstriction, respectively. The graphical representation of the cell deformation in xy-plane together with the mean local strain estimates in

xy- and in xz-planes are presented in Figure 4.A.13a. The maximum absolute strain, ε_{max}, for an cDC measurement on untreated HL60 cells was located at the ellipse tip along the major axis and amounted to 92%, while the average absolute strain, $\overline{\varepsilon}$, amounted to 37%.

For sDC, r_0 is estimated for each cell assuming a sphere of volume equivalent to the volume calculated by rotating a bullet-shaped contour of deformed cell around its symmetry axis. $r(\theta, \phi)$ represents the distance of the fitted contour to the shape's center of mass. The graphical representation of the cell deformation in the imaging plane xy as well as mean local strain estimates $\varepsilon_{xy}(\theta)$ and $\varepsilon_{xz}(\theta)$ are presented in Figure 4.A.13b. The maximum absolute strain, ε_{max}, for an sDC measurement on untreated HL60 cells is located at the tip of bullet-like shape and amounted to 47%, while the mean absolute strain, $\overline{\varepsilon}$, amounted to 17%.

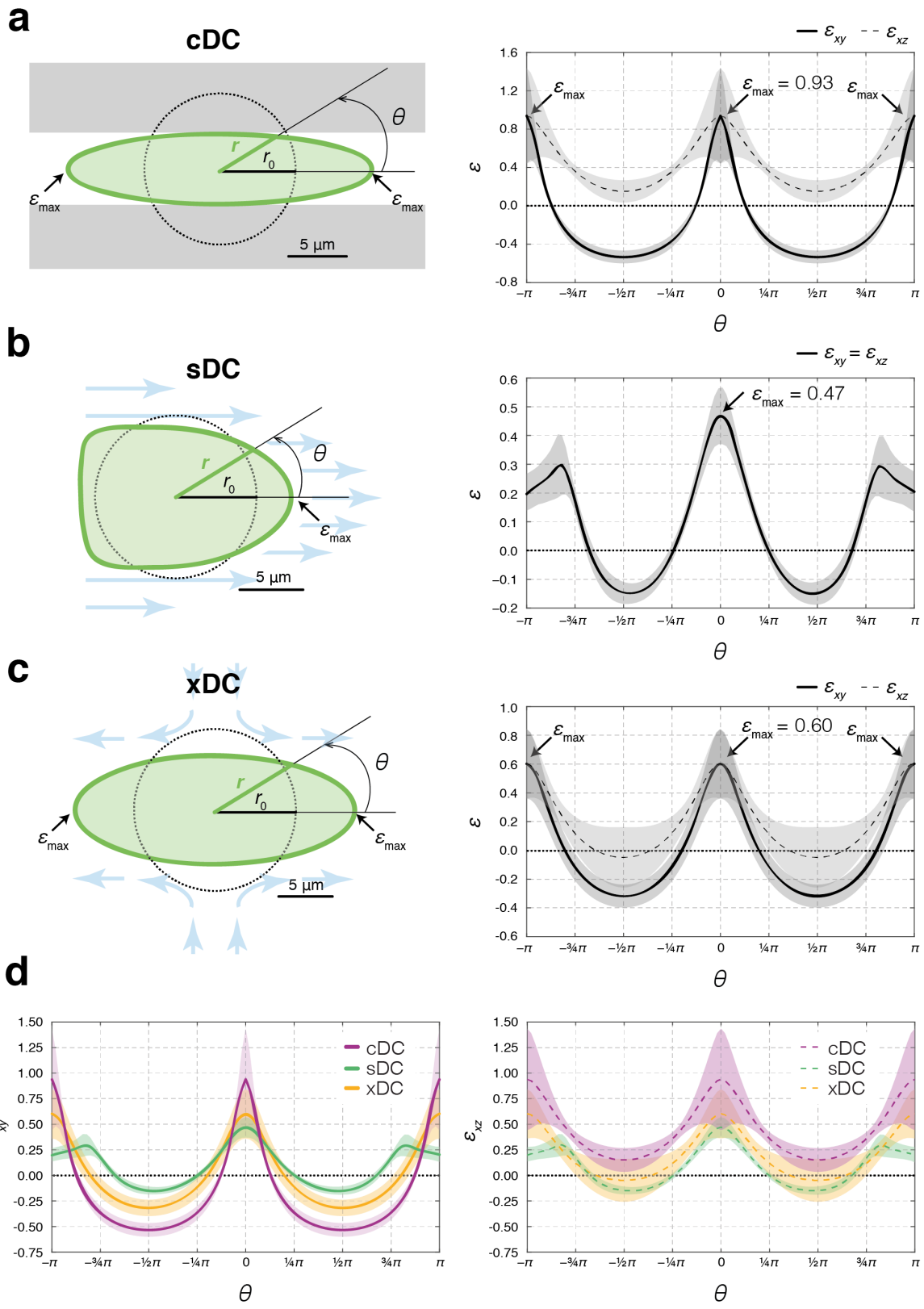
a
cDC
θ
r
r0
εmax
εmax
5 μm
εxy
εxz
1.6
1.2
0.8
0.4
0.0
-0.4
-0.8
εmax
εmax = 0.93
εmax
ε
−π
−¾π
−½π
−¼π
0
¼π
½π
¾π
π
θ
b
sDC
θ
r
r0
εmax
5 μm
εxy = εxz
0.6
0.5
0.4
0.3
0.2
0.1
0.0
−0.1
−0.2
εmax = 0.47
ε
θ
c
xDC
θ
r
r0
εmax
εmax
5 μm
εxy
εxz
1.0
0.8
0.6
0.4
0.2
0.0
-0.2
-0.4
-0.6
εmax
εmax = 0.60
εmax
ε
θ
d
1.50
1.25
1.00
0.75
0.50
0.25
0.00
-0.25
-0.50
-0.75
cDC
sDC
xDC
εxy
−π
−¾π
−½π
−¼π
0
¼π
½π
¾π
π
θ
1.50
1.25
1.00
0.75
0.50
0.25
0.00
-0.25
-0.50
-0.75
cDC
sDC
xDC
εxz
−π
−¾π
−½π
−¼π
0
¼π
½π
¾π
π
θ

Figure 4.A.13: **Radial representation of local strain experienced by untreated HL60 cells during microfluidic deformation experiments.** (**a-c**) A graphical representation of undeformed and deformed sphere cross-section in the xy-plane together with local strain estimate in xy- and xz-planes along the polar angle θ for cDC (**a**), sDC (**b**), and xDC (**c**). (**d**) An overlay of local strain in xy- (left-hand side) and xz-planes (right-hand side) for all three methods. For all plots, lines represent means over n = 1,428, 928, and 6,157 events for cDC, sDC and xDC, respectively, gathered in one representative experiment on untreated HL60 cells. Shaded areas represent standard deviations.

For xDC, r_0 is specified for each cell based on the cell diameter estimated from undeformed cell images, and $r(\theta, \phi)$ is calculated assuming volume conservation and a deformation into an ellipsoid with the experimentally determined major and minor axes in the xy-plane (a and b in Figure 4.1c, respectively). The graphical representation of the cell deformation in the imaging plane xy as well as mean local strain estimates $\varepsilon_{xy}(\theta)$ and $\varepsilon_{xz}(\theta)$ are presented in Figure 4.A.13c. The maximum absolute strain, ε_{max}, for a xDC measurement on untreated HL60 cells was located at the ellipse tip along the major axis and amounted to 60%, while the mean absolute strain, $\overline{\varepsilon}$, amounted to 24%.

An overlay of $\varepsilon_{xy}(\theta)$ and $\varepsilon_{xz}(\theta)$ for all three methods is depicted in Figure 4.A.13d.

4.A.1.3 Strain rate estimation

The strain rate is calculated for the individual methods according to the formula

$$\dot{\varepsilon} = \frac{d\varepsilon}{dt} = \frac{\overline{\varepsilon}}{\tau} \tag{4.A.6}$$

where $\overline{\varepsilon}$ is the mean absolute strain defined in Equation (4.A.5) and τ is the characteristic timescale of the measurement or, in other words, the time in which the cell is deformed, and is specified for each method in Table 4.1.

4.A.1.4 Stress estimation

The stress applied to cells passing through the microconstriction in an cDC measurement can reach a maximal value corresponding to the total applied pressure differential that drives the fluid flow in the system set to 1 kPa. This stress is applied providing that the cell fills the entire cross-section of the constriction. In reality, there are gaps between the cell and channel walls. The expected total applied stress is therefore close to, but below, 1 kPa.

There are two types of stresses acting on a cell during an sDC experiment: hydrodynamic shear stress, σ_{sh}, arising from velocity gradient inside the channel and acting tangentially on the cell surface, and hydrodynamic pressure, σ_p, which arises from pressure gradients and acts in the direction perpendicular to the cell surface. The magnitude of these stresses can be derived analytically for a case of a channel with circular cross-section using a flow-field calculated with stream function approach as previously described [30]. The calculations for the channel with circular cross-section were shown to deliver a good approximation of the stresses acting on the cell in a square channel of corresponding dimensions [30]. The results of the estimations for the parameters used during sDC experiments in our study are show in Figure 4.A.14. The peak shear stress acting on the cell surface amounts to roughly 0.43 kPa, and the peak hydrodynamic pressure to 0.78 kPa. Therefore, we can conclude that the deformation-relevant peak stresses in sDC are on the order of 1 kPa.

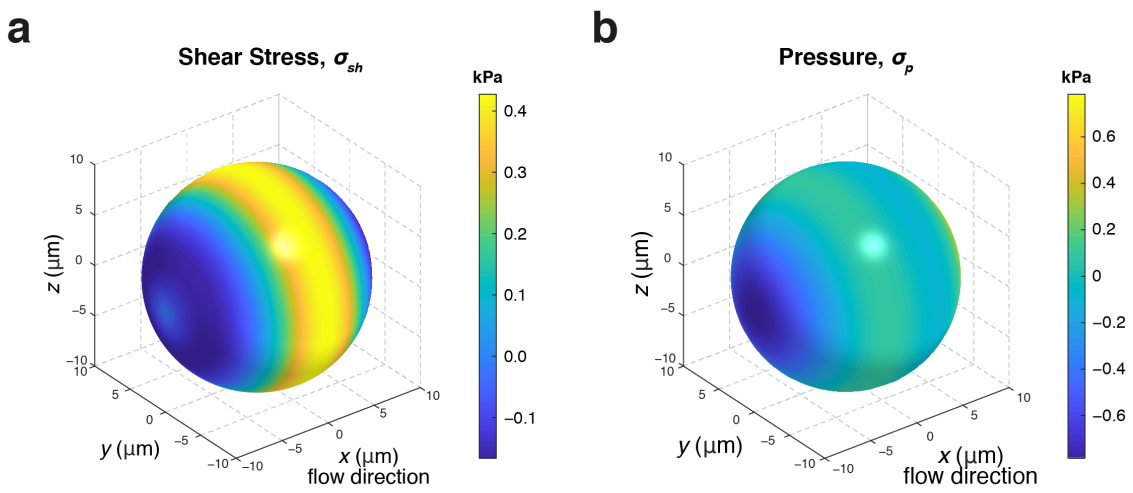

Figure 4.A.14: **Analytical estimation of surface stresses acting on an undeformed sphere passing through a circular channel approximating an sDC experiment.** A map of hydrodynamic shear stress (a) and hydrodynamic pressure (b) on a surface of a sphere of radius 6.5 µm passing through a cylindrical channel with a diameter of 20 µm at a flowrate of 0.04 µL · s^{-1} and medium viscosity of 5.7 mPa · s, corresponding to the shear-adjusted viscosity of the used measurement buffer [53].

In xDC, there are two type of forces acting on a cell in the extensional-flow region, the drag force and the shear force, with the drag force being three order of magnitudes bigger than the shear force [11]. The drag force acting on a cell is estimated to exceed 1 µN [11], therefore the corresponding estimated stress acting on a cell with a diameter of 15 µm would amount to values exceeding 5.7 kPa.

Bibliography

[1] D. Di Carlo. A Mechanical Biomarker of Cell State in Medicine. *Journal of Laboratory Automation*, 17(1):32–42, 2012.

[2] Eric M. Darling and Dino Di Carlo. High-Throughput Assessment of Cellular Mechanical Properties. *Annual Review of Biomedical Engineering*, 17(1):35–62, 2015.

[3] Yasaman Nematbakhsh and Chwee Teck Lim. Cell biomechanics and its applications in human disease diagnosis. *Acta Mechanica Sinica*, 31(2):268–273, 2015.

[4] Oliver Otto, Philipp Rosendahl, Alexander Mietke, Stefan Golfier, Christoph Herold, Daniel Klaue, Salvatore Girardo, Stefano Pagliara, Andrew Ekpenyong, Angela Jacobi, Manja Wobus, Nicole Töpfner, Ulrich F Keyser, Jörg Mansfeld, Elisabeth Fischer-Friedrich, and Jochen Guck. Real-time deformability cytometry: on-the-fly cell mechanical phenotyping. *Nature Methods*, 12(3):199–202, 2015.

[5] Sangwon Byun, Sungmin Son, Dario Amodei, Nathan Cermak, Josephine Shaw, Joon Ho Kang, Vivian C Hecht, Monte M Winslow, Tyler Jacks, Parag Mallick, and Scott R Manalis. Characterizing deformability and surface friction of cancer cells. *Proceedings of the National Academy of Sciences of the United States of America*, 110(19):7580–5, 2013.

[6] Jochen Guck, Stefan Schinkinger, Bryan Lincoln, Falk Wottawah, Susanne Ebert, Maren Romeyke, Dominik Lenz, Harold M Erickson, Revathi Ananthakrishnan, Daniel Mitchell, Josef Käs, Sydney Ulvick, and Curt Bilby. Optical deformability as an inherent cell marker for testing malignant transformation and metastatic competence. *Biophysical journal*, 88(5):3689–3698, 2005.

[7] Vinay Swaminathan, Karthikeyan Mythreye, E. Tim O'Brien, Andrew Berchuck, Gerard C. Blobe, and Richard Superfine. Mechanical Stiffness grades metastatic potential in patient tumor cells and in cancer cell lines. *Cancer Research*, 71(15):5075–5080, 2011.

[8] Henry T K Tse, Daniel R Gossett, Yo Sup Moon, Mahdokht Masaeli, Marie Sohsman, Yong Ying, Kimberly Mislick, Ryan P Adams, Jianyu Rao, and Dino Di Carlo. Quantitative diagnosis of malignant pleural effusions by single-cell mechanophenotyping. *Science translational medicine*, 5(212):212ra163, 2013.

[9] Kathleen R. Bashant, Arlette Vassallo, Christoph Herold, Reinhard Berner, Leonhard Menschner, Julien Subburayalu, Mariana J. Kaplan, Charlotte Summers, Jochen Guck, Edwin R. Chilvers, and Nicole Toepfner. Real-time deformability cytometry reveals sequential contraction and expansion during neutrophil priming. *Journal of Leukocyte Biology*, 105(6):1143–1153, jun 2019.

[10] Nathalie Bufi, Michael Saitakis, Stéphanie Dogniaux, Oscar Buschinger, Armelle Bohineust, Alain Richert, Mathieu Maurin, Claire Hivroz, and Atef Asnacios. Human primary immune cells exhibit distinct mechanical properties that are modified by inflammation. *Biophysical Journal*, 108(9):2181–2190, 2015.

[11] D. R. Gossett, H. T. K. Tse, S. a. Lee, Y. Ying, a. G. Lindgren, O. O. Yang, J. Rao, a. T. Clark, and D. Di Carlo. Hydrodynamic stretching of single cells for large population mechanical phenotyping. *Proceedings of the National Academy of Sciences*, 109(20):7630–7635, 2012.

[12] Michael J. Rosenbluth, Wilbur A. Lam, and Daniel A. Fletcher. Analyzing cell mechanics in hematologic diseases with microfluidic biophysical flow cytometry. *Lab on a Chip*, 8(7):1062–1070, 2008.

[13] Nicole Toepfner, Christoph Herold, Oliver Otto, Philipp Rosendahl, Angela Jacobi, Martin Kräter, Julia Stächele, Leonard Menschner, Maik Herbig, Laura Ciuffreda, Lisa Ranford-Cartwright, Michal Grzybek, Ünal Coskun, Elisabeth Reithuber, Genevieve Garriss, Peter Mellroth, Birgitta Henriques Normark, Nicola Tregay, Meinolf Suttorp, Martin Bornhäuser, Edwin R Chilvers, Reinhard Berner, and Jochen Guck. Detection of human disease conditions by single-cell morpho-rheological phenotyping of blood. *eLife*, 7:e29213, 2018.

[14] Andrew E. Ekpenyong, Graeme Whyte, Kevin Chalut, Stefano Pagliara, Franziska Lautenschläger, Christine Fiddler, Stephan Paschke, Ulrich F. Keyser, Edwin R. Chilvers, and Jochen Guck. Viscoelastic Properties of Differentiating Blood Cells Are Fate- and Function-Dependent. *PLoS ONE*, 7(9):e45237, 2012.

[15] Jonathan Lin, Donghyuk Kim, Henry T. Tse, Peter Tseng, Lillian Peng, Manjima Dhar, Saravanan Karumbayaram, and Dino Di Carlo. High-throughput physical phenotyping of cell differentiation. *Microsystems & Nanoengineering*, 3:17013, May 2017.

[16] Marta Urbanska, Maria Winzi, Katrin Neumann, Shada Abuhattum, Philipp Rosendahl, Paul Müller, Anna Taubenberger, Konstantinos Anastassiadis, and Jochen Guck. Single-cell mechanical phenotype is an intrinsic marker of reprogramming and differentiation along the mouse neural lineage. *Development*, pages 4313–4321, 2017.

[17] Chii J. Chan, Carl Philipp Heisenberg, and Takashi Hiiragi. Coordination of Morphogenesis and Cell-Fate Specification in Development. *Current Biology*, 27(18):R1024–R1035, 2017.

[18] Tadanori Mammoto and Donald E Ingber. Mechanical control of tissue and organ development. *Development (Cambridge, England)*, 137(9):1407–20, 2010.

[19] Manfred Radmacher. Studying the Mechanics of Cellular Processes by Atomic Force Microscopy. *Methods in Cell Biology*, 83(07):347–372, 2007.

[20] Robert M. Hochmuth. Micropipette aspiration of living cells. *Journal of Biomechanics*, 33(1):15–22, 2000.

[21] J Guck, R Ananthakrishnan, H Mahmood, T J Moon, C C Cunningham, and J Käs. The optical stretcher: a novel laser tool to micromanipulate cells. *Biophysical journal*, 81(2):767–784, 2001.

[22] Olivier Thoumine, Albrecht Ott, Olivier Cardoso, and Jean-Jacques Meister. Microplates: a new tool for manipulation and mechanical perturbation of individual cells. *Journal of Biochemical and Biophysical Methods*, 39(1-2):47–62, Feb 1999.

[23] Pei Hsun Wu, Dikla Raz Ben Aroush, Atef Asnacios, Wei Chiang Chen, Maxim E. Dokukin, Bryant L. Doss, Pauline Durand-Smet, Andrew Ekpenyong, Jochen Guck, Nataliia V. Guz, Paul A. Janmey, Jerry S.H. Lee, Nicole M. Moore, Albrecht Ott, Yeh Chuin Poh, Robert Ros, Mathias Sander, Igor Sokolov, Jack R. Staunton, Ning Wang, Graeme Whyte, and Denis Wirtz. A comparison of methods to assess cell mechanical properties. *Nature Methods*, pages 1–8, 2018.

[24] Andrea Adamo, Armon Sharei, Luigi Adamo, Byungkun Lee, Shirley Mao, and Klavs F. Jensen. Microfluidics-based assessment of cell deformability. *Analytical Chemistry*, 84(15):6438–6443, 2012.

[25] Janina R. Lange, Julian Steinwachs, Thorsten Kolb, Lena A. Lautscham, Irina Harder, Graeme Whyte, and Ben Fabry. Microconstriction Arrays for High-Throughput Quantitative Measurements of Cell Mechanical Properties. *Biophysical Journal*, 109(1):26–34, 2015.

[26] Kendra D. Nyberg, Kenneth H. Hu, Sara H. Kleinman, Damir B. Khismatullin, Manish J. Butte, and Amy C. Rowat. Quantitative Deformability Cytometry: Rapid, Calibrated Measurements of Cell Mechanical Properties. *Biophysical Journal*, 113(7):1574–1584, 2017.

[27] Fern J. Armistead, Julia Gala De Pablo, Hermes Gadêlha, Sally A. Peyman, and Stephen D. Evans. Cells Under Stress: An Inertial-Shear Microfluidic Determination Of Cell Behaviour. *Biophysical Journal*, 2019.

[28] Lionel Guillou, Joanna B Dahl, Jung-Ming G Lin, AbduI I Barakat, Julien Husson, Susan J Muller, and Sanjay Kumar. Measuring Cell Viscoelastic Properties Using a Microfluidic Extensional Flow Device. *Biophysical journal*, 111(9):2039–2050, Nov 2016.

[29] Stefan Golfier, Philipp Rosendahl, Alexander Mietke, Maik Herbig, Jochen Guck, and Oliver Otto. High-throughput cell mechanical phenotyping for label-free titration assays of cytoskeletal modifications. *Cytoskeleton*, 74(8):283–296, 2017.

[30] Alexander Mietke, Oliver Otto, Salvatore Girardo, Philipp Rosendahl, Anna Taubenberger, Stefan Golfier, Elke Ulbricht, Sebastian Aland, Jochen Guck, and Elisabeth Fischer-Friedrich. Extracting Cell Stiffness from Real-Time Deformability Cytometry: Theory and Experiment. *Biophysical Journal*, 109(10):2023–2036, 2015.

[31] Farshid Guilak, Geoffrey R. Erickson, and H. Ping Ting-Beall. The effects of osmotic stress on the viscoelastic and physical properties of articular chondrocytes. *Biophysical Journal*, 82(2):720–727, 2002.

[32] Ming Guo, Adrian F. Pegoraro, Angelo Mao, Enhua H. Zhou, Praveen R. Arany, Yulong Han, Dylan T. Burnette, Mikkel H. Jensen, Karen E. Kasza, Jeffrey R. Moore, Frederick C. Mackintosh, Jeffrey J. Fredberg, David J. Mooney, Jennifer Lippincott-Schwartz, and David A. Weitz. Cell volume change through water efflux impacts cell stiffness and stem cell fate. *Proceedings of the National Academy of Sciences*, c(Peg 300):201705179, 2017.

[33] Emad Moeendarbary, Léo Valon, Marco Fritzsche, Andrew R. Harris, Dale A. Moulding, Adrian J. Thrasher, Eleanor Stride, L. Mahadevan, and Guillaume T. Charras. The cytoplasm of living cells behaves as a poroelastic material. *Nature Materials*, 12(3):253–261, 2013.

[34] E. H. Zhou, X. Trepat, C. Y. Park, G. Lenormand, M. N. Oliver, S. M. Mijailovich, C. Hardin, D. A. Weitz, J. P. Butler, and J. J. Fredberg. Universal behavior of the osmotically compressed cell and its analogy to the colloidal glass transition. *Proceedings of the National Academy of Sciences*, 106(26):10632–10637, 2009.

[35] T Wakatsuki, B Schwab, N C Thompson, and E L Elson. Effects of cytochalasin D and latrunculin B on mechanical properties of cells. *Journal of cell science*, 114(Pt 5):1025–1036, 2001.

[36] Guillaume Salbreux, Guillaume Charras, and Ewa Paluch. Actin cortex mechanics and cellular morphogenesis. *Trends in Cell Biology*, 22(10):536–545, 2012.

[37] Walter M. Morton, Kathryn R. Ayscough, and Paul J. Mclaughlin. Latrunculin alters the actin-monomer subunit interface to prevent polymerization. *Nature Cell Biology*, 2(6):376–378, 2000.

[38] I. Spector, N. R. Shorlet, D. Blasberger, and Y. Kashman. Latrunculins - novel marine macrolides that disrupt microfilament organization and affert cell growth: I. Comparison with cytochalasin D. *Cell Motility and the Cytoskeleton*, 13(3):127–144, 1989.

[39] Jochen Guck and Edwin R. Chilvers. Mechanics meets medicine. *Science Translational Medicine*, 5(212):3–6, 2013.

[40] John D. Finan and Farshid Guilak. The effects of osmotic stress on the structure and function of the cell nucleus. *Journal of Cellular Biochemistry*, 109(3):460–467, 2010.

[41] K R Hallows, C H Packman, and P A Knauf. Acute cell volume changes in anisotonic media affect F-actin content of HL-60 cells. *The American journal of physiology*, 261(6 Pt 1):C1154–61, 1991.

[42] P. A. Janmey, U. Euteneuer, P. Traub, and M. Schliwa. Viscoelastic properties of vimentin compared with other filamentous biopolymer networks. *Journal of Cell Biology*, 113(1):155–160, 1991.

[43] K. Maruyama, M. Kaibara, and E. Fukada. Rheology of F-actin I. Network of F-actin in solution. *Biochimica et Biophysica Acta (BBA) - Protein Structure*, 371(1):20–29, Nov 1974.

[44] Thomas P. Burg, Michel Godin, Scott M. Knudsen, Wenjiang Shen, Greg Carlson, John S. Foster, Ken Babcock, and Scott R. Manalis. Weighing of biomolecules, single cells and single nanoparticles in fluid. *Nature*, 446(7139):1066–1069, 2007.

[45] Ahmad Ahsan Nawaz, Marta Urbanska, Maik Herbig, Martin Nötzel, Martin Kräter, Philipp Rosendahl, Christoph Herold, Nicole Toepfner, Markéta Kubánková, Ruchi Goswami, Shada Abuhattum, Felix Reichel, Paul Müller, Anna Taubenberger, Salvatore Girardo, Angela Jacobi, and Jochen Guck. Intelligent image-based deformation-assisted cell sorting with molecular specificity. *Nature Methods*, 17(6):595–599, jun 2020.

[46] Philipp Rosendahl, Katarzyna Plak, Angela Jacobi, Martin Kraeter, Nicole Toepfner, Oliver Otto, Christoph Herold, Maria Winzi, Maik Herbig, Yan Ge, Salvatore Girardo, Katrin Wagner, Buzz Baum, and Jochen Guck. Real-time fluorescence and deformability cytometry. *Nature Methods*, 15(5):355, 2018.

[47] M. Mokbel, D. Mokbel, A. Mietke, N. Träber, G. Salvatore, O. Otto, J. Guck, and S. Aland. Numerical Simulation of Real-Time Deformability Cytometry To Extract Cell Mechanical Properties. *ACS Biomaterials Science & Engineering*, 2017.

[48] Bob Fregin, Fabian Czerwinski, Doreen Biedenweg, Salvatore Girardo, Stefan Gross, Konstanze Aurich, and Oliver Otto. High-throughput single-cell rheology in complex samples by dynamic real-time deformability cytometry. *Nature communications*, 10(1):415, 2019.

[49] Jochen Guck. Some thoughts on the future of cell mechanics, 2019.

[50] Nathan Cermak, Selim Olcum, Francisco Feijó Delgado, Steven C. Wasserman, Kristofor R. Payer, Mark A. Murakami, Scott M. Knudsen, Robert J. Kimmerling, Mark M. Stevens, Yuki Kikuchi, Arzu Sandikci, Masaaki Ogawa, Vincent Agache, François Baléras, David M. Weinstock, and Scott R. Manalis. High-throughput measurement of single-cell growth rates using serial microfluidic mass sensor arrays. *Nature Biotechnology*, 34(10):1052–1059, Oct 2016.

[51] J. Lee, R. Chunara, W. Shen, K. Payer, K. Babcock, T. P. Burg, and S. R. Manalis. Suspended microchannel resonators with piezoresistive sensors. *Lab Chip*, 11(4):645–651, Jan 2011.

[52] Maik Herbig, Martin Kräter, Katarzyna Plak, Paul Müller, Jochen Guck, and Oliver Otto. *Real-Time Deformability Cytometry: Label-Free Functional Characterization of Cells*, pages 347–369. Springer New York, New York, NY, 2018.

[53] Christoph Herold. Mapping of Deformation to Apparent Young's Modulus in Real-Time Deformability Cytometry, 2017.

[54] Else K Hoffmann, Ian H Lambert, and Stine F Pedersen. Physiology of cell volume regulation in vertebrates. *Physiological reviews*, 89(1):193–277, 2009.

[55] Harvey Motulsky and Arthur Christopoulos. Comparing models using the extra sum-of-squares F test. In *Fitting models to biological data using linear and nonlinear regression: a practical guide to curve fitting.*, chapter Comparing, pages 138–142. Oxford University Press, 2004.

[56] Hervé Abdi. The Bonferonni and Šidák Corrections for Multiple Comparisons. In Neil Salkind, editor, *Encyclopedia of Measurement and Statistics*, pages 103–107. Sage, Thousand Oaks (CA), 2007.

[57] Christian Ritz, Florent Baty, Jens C. Streibig, and Daniel Gerhard. Dose-response analysis using R. *PLoS ONE*, 10(12):1–13, 2015.

[58] Sangwon Byun, Vivian C. Hecht, and Scott R. Manalis. Characterizing Cellular Biophysical Responses to Stress by Relating Density, Deformability, and Size. *Biophysical Journal*, 109(8):1565–1573, Oct 2015.

[59] Amy C. Rowat, Diana E. Jaalouk, Monika Zwerger, W. Lloyd Ung, Irwin A. Eydelnant, Don E. Olins, Ada L. Olins, Harald Herrmann, David A. Weitz, and Jan Lammerding. Nuclear envelope composition determines the ability of neutrophil-type cells to passage through micron-scale constrictions. *Journal of Biological Chemistry*, 288(12):8610–8618, 2013.

[60] Kendra D. Nyberg, Samuel L. Bruce, Angelyn V. Nguyen, Clara K. Chan, Navjot K. Gill, Tae Hyung Kim, Erica K. Sloan, and Amy C. Rowat. Predicting cancer cell invasion by single-cell physical phenotyping. *Integrative Biology*, 10(4):218–231, 2018.

[61] Josephine Shaw Bagnall, Sangwon Byun, Shahinoor Begum, David T. Miyamoto, Vivian C. Hecht, Shyamala Maheswaran, Shannon L. Stott, Mehmet Toner, Richard O. Hynes, and Scott R. Manalis. Deformability of Tumor Cells versus Blood Cells. *Scientific Reports*, 5(1):18542, Nov 2016.

[62] Joanne M. Kwan, Quan Guo, Dana L. Kyluik-Price, Hongshen Ma, and Mark D. Scott. Microfluidic analysis of cellular deformability of normal and oxidatively damaged red blood cells. *American Journal of Hematology*, 88(8):682–689, Aug 2013.

[63] Josephine Shaw Bagnall, Sangwon Byun, David T. Miyamoto, Joon Ho Kang, Shyamala Maheswaran, Shannon L. Stott, Mehmet Toner, and Scott R. Manalis. Deformability-based cell selection with downstream immunofluorescence analysis. *Integrative Biology*, 8(5):654–664, May 2016.

[64] Shamim M Ahmmed, Swastika S Bithi, Adity A Pore, Noshin Mubtasim, Caroline Schuster, Lauren S Gollahon, and Siva A Vanapalli. Multi-sample deformability cytometry of cancer cells. *APL Bioengineering*, 2(3):032002, 2018.

[65] Sandra Tavares, André Filipe Vieira, Anna Verena Taubenberger, Margarida Araújo, Nuno Pimpao Martins, Catarina Brás-Pereira, António Polónia, Maik Herbig, Clara Barreto, Oliver Otto, Joana Cardoso, José B. Pereira-Leal, Jochen Guck, Joana Paredes, and Florence Janody. Actin stress fiber organization promotes cell stiffening and proliferation of pre-invasive breast cancer cells. *Nature Communications*, 8:15237, May 2017.

[66] Marion Koch, Katherine E. Wright, Oliver Otto, Maik Herbig, Nichole D. Salinas, Niraj H. Tolia, Timothy J. Satchwell, Jochen Guck, Nicholas J. Brooks, and Jake Baum. Plasmodium falciparum erythrocyte-binding antigen 175 triggers a biophysical change in the red blood cell that facilitates invasion. *Proceedings of the National Academy of Sciences*, 114(16):4225–4230, 2017.

[67] Sabine Steffen, Susanne Abraham, Maik Herbig, Franziska Schmidt, Kristin Blau, Susann Meisterfeld, Stefan Beissert, Jochen Guck, and Claudia Günther. Toll-Like Receptor-Mediated Upregulation of CXCL16 in Psoriasis Orchestrates Neutrophil Activation. *Journal of Investigative Dermatology*, 138(2):344–354, 2018.

[68] Martin Kräter, Jiranuwat Sapudom, Nicole Bilz, Tilo Pompe, Jochen Guck, and Claudia Claus. Alterations in Cell Mechanics by Actin Cytoskeletal Changes Correlate with Strain-Specific Rubella Virus Phenotypes for Cell Migration and Induction of Apoptosis. *Cells*, 7(9):136, 2018.

[69] Miguel Xavier, Philipp Rosendahl, Maik Herbig, Martin Kräter, Daniel Spencer, Martin Bornhäuser, Richard O. C. Oreffo, Hywel Morgan, Jochen Guck, and Oliver Otto. Mechanical phenotyping of primary human skeletal stem cells in heterogeneous populations by real-time deformability cytometry. *Integrative Biology*, 8(5):616–623, May 2016.

[70] Angela Jacobi, Philipp Rosendahl, Martin Kräter, Marta Urbanska, Maik Herbig, and Jochen Guck. Analysis of Biomechanical Properties of Hematopoietic Stem and Progenitor Cells Using Real-Time Fluorescence and Deformability Cytometry. In *Methods in Molecular Biology*, volume 2017, pages 135–148. Humana Press Inc., 2019.

[71] Tiago Santos-Ferreira, Maik Herbig, Oliver Otto, Madalena Carido, Mike O. Karl, Stylianos Michalakis, Jochen Guck, and Marius Ader. Morpho-Rheological Fingerprinting of Rod Photoreceptors Using Real-Time Deformability Cytometry. *Cytometry Part A*, 95(11):1145–1157, Nov 2019.

[72] Matthias Christoph Munder, Daniel Midtvedt, Titus Franzmann, Elisabeth Nuske, Oliver Otto, Maik Herbig, Elke Ulbricht, Paul Müller, Anna Taubenberger, Shovamayee Maharana, Liliana Malinovska, Doris Richter, Jochen Guck, Vasily Zaburdaev, and Simon Alberti. A pH-driven transition of the cytoplasm from a fluid- to a solid-like state promotes entry into dormancy. *eLife*, 5, Mar 2016.

[73] Stefanie Tietze, Martin Kräter, Angela Jacobi, Anna Taubenberger, Maik Herbig, Rebekka Wehner, Marc Schmitz, Oliver Otto, Catrin List, Berna Kaya, Manja Wobus, Martin Bornhäuser, and Jochen Guck. Spheroid Culture of Mesenchymal Stromal Cells

Results in Morphorheological Properties Appropriate for Improved Microcirculation. *Advanced Science*, page 1802104, 2019.

[74] Mahdokht Masaeli, Dewal Gupta, Sean O'Byrne, Henry T. K. Tse, Daniel R. Gossett, Peter Tseng, Andrew S. Utada, Hea-Jin Jung, Stephen Young, Amander T. Clark, and Dino Di Carlo. Multiparameter mechanical and morphometric screening of cells. *Scientific Reports*, 6(1):37863, Dec 2016.

[75] Katherine Crawford, Aaron DeWitt, Stephen Brierre, Terrell Caffery, Tonya Jagneaux, Christopher Thomas, Mara Macdonald, Henry Tse, Ajay Shah, Dino Di Carlo, and Hollis R. O'Neal. Rapid Biophysical Analysis of Host Immune Cell Variations Associated with Sepsis. *American Journal of Respiratory and Critical Care Medicine*, 198(2):280–282, Jul 2018.

[76] Sukgyun Cha, Taeho Shin, Sung Sik Lee, Wooyoung Shim, Gwang Lee, Seong Jae Lee, Younghun Kim, and Ju Min Kim. Cell Stretching Measurement Utilizing Viscoelastic Particle Focusing. *Analytical Chemistry*, 84(23):10471–10477, Dec 2012.

CHAPTER 5

Fluorescence imaging deformability cytometry: integrating nuclear structure with mechanical phenotyping

5.1 Introduction

In the past few decades, tools measuring the mechanical properties of cells have grown in sophistication and diversification [1]. Cell mechanical phenotypes are the culmination of intracellular components such as the cytoskeleton and nucleus. As these components reorganize or change form or function, the cell's mechanical properties can change with them. These changes have been related to changes in cell cycle [2], leukocyte activation [3], cancer malignancy [4], and cell differentiation [5, 6], among many others. A variety of tools have been used to probe cells' response to force, such as atomic force microscopy (AFM) [7], micropipette aspiration [8], or optical tweezers [9], but all these methods can be labor intensive, affected by user variability, and do not scale well. Recently, several microfluidics methods have been developed that allow cells to be measured robustly, and at higher throughput [5, 10, 2]. Higher throughput methods enable more cells to be measured, providing a more complete picture of cell heterogeneity or rare subpopulations. Although all these methods aim to measure the mechanical properties, they vary widely in implementation, applied stress, time scales, and quantification of deformation [11]. These methods generally quantify cell deformation in a way that considers a cell to be a uniform elastic object, without isolating nuclear contributions, or identifying local deformation.

As a major component of the cell, the nucleus has been found to alter overall deformability

via chromatin reorganization [12, 13], nuclear envelope alteration [12, 13, 14], and cell cycle progression [15, 2, 16]. The nucleus's mechanical properties have also taken a more active role in the cell's function by facilitating cell migration [17, 14, 18] and genomic architecture reorganization [19, 20].

Massive nuclear reorganization also occurs in neutrophils when generating neutrophil extracellular traps (NETs) [21]. Neutrophils are a vital part of the innate immune system. In the defense against pathogens, neutrophils were long thought to attack invading organisms via phagocytosis, or release of anti-microbials from their granules. However, a third role has somewhat recently been discovered, where neutrophils release NETs [22]. NETs are comprised of the neutrophil's decondensed chromatin, embedded with cytosolic and granule proteins. These NETs are intended to trap and neutralize pathogens including bacteria, fungi, viruses and parasites [21]. During the process of creating NETs, or NETosis, the neutrophil's chromatin decondenses, the nuclear envelope breaks down, and the chromatin mixes with the cell's anti-microbials before being released into the extracellular environment. This process normally results in the death of the neutrophil, although there is a form of non-lytic NETosis where the NETs are released, and the chromatin-less cells remain intact. Despite the advantages of NETs in an immune response, NETs have been implicated in various autoimmune diseases including rheumatoid arthritis, psoriasis, and gout [23], as well as infertility and preeclampsia during pregnancy [24].

NETosis induces large structural changes in neutrophils within hours. This has been observed *in vitro* by inducing NETosis with Phorbol myristate acetate (PMA), and utilizing fluorescence microscopy to observe the chromatin decondense and pervade the cell before rupturing [25]. NETosis has also been characterized using imaging flow cytometry, utilizing PMA or lipopolysaccharide (LPS) to induce NETosis [26]. In addition to staining and characterizing the nuclear structure, this work also stained myeloperoxidase (MPO), a key biomarker of NETosis, which is normally compartmentalized in the neutrophil granules, but is collocated by the end of NETosis. Due to the massive structural reorganization needed to produce NETs, we believe that neutrophils undergoing NETosis should have significant

changes in deformability, which should be measurable with FI-DC. This has not been specifically measured or reported. The nuclear composition in neutrophil-like cells has previously been shown to impact the cells' deformability, and ability to pass through small spaces [14], which indicates that chromatin decondensing or nuclear envelope breakdown in NETosis should have a significant impact on cell deformability. Identifying NETosing cells in flow may be valuable to potentially assess pathogen loads or assessing the efficacy of autoimmune treatments.

However, high throughput cell deformability methods have been unable to directly include nuclear information. Many of these nuclear findings have been extracted by experiments carefully designed to alter or isolate nuclear changes. A real-time fluorescence and deformability cytometry technique has been recently developed, which is only able to provide fluorescent pulse information [27, 16]. This method has been able to identify nuclear envelope breakdown and distinguish between anaphase and metaphase cells with proper staining. Fluorescent images of nuclear structure have not been utilized in high throughout deformability methods due to the incompatibility of the time needed to integrate fluorescent images, and the speed at which cells are often flowing through the microchannels. With high resolution information of nuclear structure, we can understand how it contributes to overall cell mechanical properties, and use it to identify cell types.

To overcome these challenges, we have developed fluorescence imaging deformability cytometry (FI-DC), which uses sensitive photomultiplier tubes (PMTs) to image fluorescence channels while flowing at 0.5 $m \cdot s^{-1}$. This method utilizes fluorescence imaging using radiofrequency-tagged emission (FIRE) [28], which generates images by integrating a line of pixels across the channel of a microfluidic device. We combine this imaging with a shear flow deformability method [2] that features tunable sheath flow geometry that allows us to tune cell deformation. When used with appropriate nuclear or other intracellular stains, this platform allows us to directly combine intracellular imaging with cell deformation.

5.2 Results

5.2.1 Overview

We have developed FI-DC, a platform for deforming cells in flow, while delivering simultaneous brightfield and fluorescent images. FI-DC is the first deformability method of its kind that is able to operate at modest throughputs (0.5 m $\cdot$ s^{-1}) while delivering images that reveal both the shape and size of the cells, in addition to internal cellular structure. Here we demonstrate its capability by providing spatial information about nuclear structure, which had not yet been realized by high throughput deformability techniques. This is achieved by combining a shear flow deformability method [2] with fast fluorescent and brightfield imaging using FIRE [28] (Figure 5.1a). We use a microfluidic device that has a center sample inlet, flanked by two additional inlets to provide sheath co-flows. A similar method has recently been used to probe cell and spheroid mechanics [29]. The streams join in a straight channel, with cross section 25 µm $\times$ 30 µm , where the cells are deformed into a bullet shape and imaged. The center sample stream contains cells suspended in 1.5% w/v Alginate in PBS, and the sheath flows are 5.0% w/v Alginate in water. The viscosity in the sample stream serves to increase the average shear stress experienced by the cells. Creating a viscosity mismatch between the sample and sheath flows pinches the velocity profile in the center of the channel (Figure 5.1a inset), creating a higher velocity gradient, and higher shear stress.

FIRE provides rich, multimodal images of cells in flow. FIRE acts as a type of line scan imaging system, building images as the cells flow past the interrogation region of the microfluidic channel. The interrogation region is exposed with a 488 nm laser, and emitted and scattered light is reconstructed to create brightfield and darkfield images, and multiple fluorescent channels. Here, we use brightfield and FITC [529/28 nm] images to measure cells and their stained nuclear structure (Figure 5.1b). The fluorescent images can reveal nucleus size, location, or cell cycle, all of which might affect cell mechanical properties. FIRE images can be acquired by setting side scatter or fluorescence thresholds, which provides initial filtering of debris, and allows for long, continuous acquisition of sparse samples. With a

sufficient cell concentration, FIRE can provide a throughput of up to hundreds of events per second.

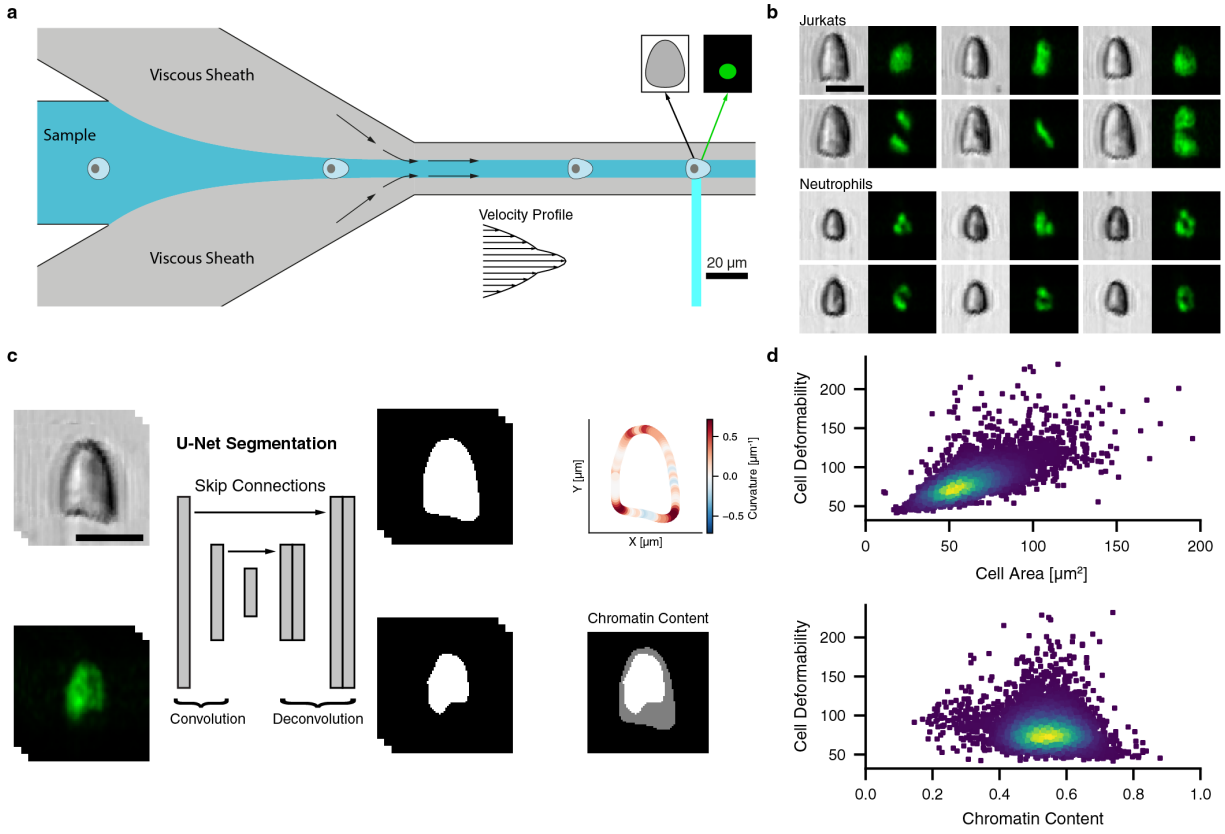

Figure 5.1: **FI-DC schematic and analysis overview.** (**a**) Cells flow through a microfluidic device with viscous sheath flows that create a pinched velocity profile (inset). After deforming, cells are interrogated in the straight channel via FIRE, producing brightfield and fluorescence images. (**b**) Jurkat and neutrophil images demonstrating varied nuclear structure. (**c**) Cells and nuclei are segmented from images using U-Net neural networks. Curvature is measured from extracted boundaries, which is integrated to yield a scale-invariant bending factor, which we use for cell deformability. Chromatin content is calculated as the ratio of nuclear and cell area. (**d**) Cell area, cell deformability and chromatin content capture fundamental features of cell populations. Unlabeled scale bars are 10 µm .

FIRE images are automatically analyzed to extract cell and nucleus morphology measures. Exported FIRE images are first filtered by a neural network to remove images with multiple cells, debris, dead cells, or partial cells. Cells and nuclei are segmented from bright-field and FITC images, respectively, using U-Net neural networks [30], which excel at segmenting biological images (Figure 5.1c). To avoid the pixelation effects from measuring the segmented objects directly, we extract smoothed contours first. We can then calculate standard morphology measurements such as cell area, perimeter, aspect ratio, and solidity.

Previous hydrodynamic deformability methods have measured cell deformability as deviations from circularity. This has been achieved by measuring the cell aspect ratio [5], or by measuring the cell's circularity [2]. Both measures do reflect some information about changes in a cell's shape, but we believe that there is some information lost about the local changes in deformation. Therefore we calculate local curvature of the extracted cell and nucleus boundaries, and use this to calculate a unit-less scale-invariant bending energy to describe the entire object [31, 32]. In this paper we will refer to this measurement as the bending factor as it is not a physical measure of energy. The bending factor gives us local information about deformation of the cell and gives us a scale-invariant measure that describes how a cell deviates from circularity. According to this scale-invariant bending factor, all perfect circles would have a value of 4π, which is the minimum possible value. The bending factor for sections along the boundaries can also be calculated, accumulating curvature measurements for any region. The bending factor is calculated for both cells and nuclei, and we use it for our definition of cell deformability. The FITC FIRE images give us information about the size and location of stained chromatin in the cells. We can leverage this information first by calculating the ratio of the chromatin area and cell area, which we refer to as chromatin content. Cell area, cell deformability, and chromatin comprise the most useful features in our analysis (Figure 5.1d).

5.2.2 Deformation characterization

Deformation of cells in FI-DC is controlled by altering the viscosity of the sample and sheath streams, while maintaining constant volumetric flow rate. Here we demonstrate the change in deformation of suspension Jurkat cells by adjusting the sample stream viscosity, as well as the differential of the sample and sheath viscosities (Figure 5.2a). As an illustration, we show cells in the following sample:sheath configurations: PBS:PBS (indigo), PBS: 2.0% w/v Alginate (violet), and 1.5% w/v Algiante:5.0% w/v Alginate (orange). As both the sample stream and sheath streams increase in viscosity, the shear stress on the cells increases, changing the cell shape from that close to a circle, to a bullet. To estimate the stress experienced by the cells, we model the channel in 3D in `COMSOL`, and calculate the average shear stress of a 10 µm × 10 µm lumen in the center of the channel (Figure 5.2a). Using the most extreme flow condition shown here, this gives us ∼44-fold increase in estimated shear stress over a PBS filled channel. The differences in cell shape seen by eye are also clear when calculating cell deformability (Figure 5.2b). Using the bending factor as the measurement for deformability, the 1.5% w/v Algiante:5.0% w/v Alginate condition gives us a clear separation from the largely undeformed cells in PBS:PBS, leading us to use this condition for the rest of the following work.

5.2.3 Revealed nuclear structure heterogeneity

FIRE's fluorescent images allow us to discover nuclear heterogeneity in Jurkat cells. Without these fluorescent intracellular images, we may only analyze cells by area and deformability. But by measuring the chromatin area per cell, we can see a subpopulation in Jurkat cells that exhibits reduced chromatin area for similarly sized cells (Figure 5.2c). This reduced chromatin content subpopulation is relatively rare (1.9%), and generally has a larger cell size and increased cell deformability than the rest of the Jurkat sample. When comparing cells within a narrow size range(Figure 5.2d), it is difficult to determine if similarly sized cells have different cell deformability due to the rare occurrence of the low chromatin content cells (Figure 5.2e).

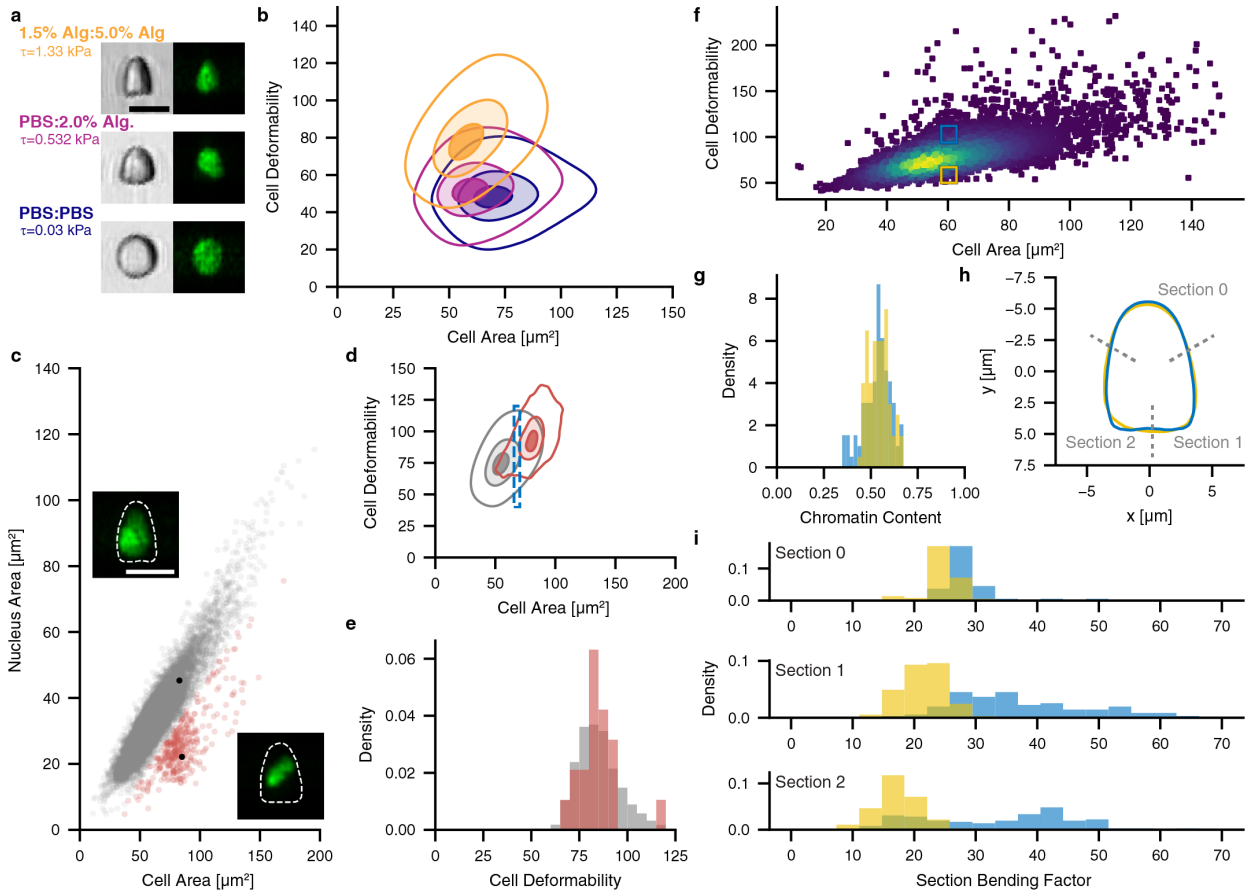

Figure 5.2: **FI-DC features tunable deformation and reveals nuclear and membrane details.** (**a**) Increasing the sample stream viscosity and the ratio of sample:sheath viscosity increases visible deformation. (**b**) Bending factor as a form of cell deformability captures the change in shape visible in images. (**c**) Nuclear images of Jurkat cells reveal a subpopulation with reduced chromatin content. (**d**) This reduced chromatin content subpopulation features a higher cell size and deformability than the rest of the cell population. (**e**) When comparing cells of similar size, there is not a drastically difference in cell deformability. (**f**) Jurkats of similar size with low (yellow) and high (blue) cell deformability are selected for comparison. (**g**) These cells do not exhibit drastically different levels of chromatin content. (**h**) Median shapes of cells in these populations reveal the high cell deformability cells are deformed more in the lower (back) corners of the cell. (**i**) Differences in the deformation of sections of the cell quantitatively demonstrates the sections of the cell responsible for overall cell deformability differences. Unlabeled scale bars are 10 μm .

5.2.4 Investigating differences in cell deformability

FI-DC's fluorescent images enable us to investigate why similarly sized cells deform differently. When comparing the mechanical properties of cells, it is useful to understand how cells of a similar size may have different deformability. This may be true when comparing different cell types or treatments, or even the natural spread within the same population. We select a sampling of approximately 100 cells at low and high deformability for the same size range, while excluding outlier cells with high deformability (Figure 5.2f). These cell groups do not have noticeably different levels of chromatin content, indicating that the difference in deformation may not be due to nuclear structure (Figure 5.2g). Instead, when using the fact that our cell boundaries have been aligned to the same polar coordinate, we can calculate median cell shapes for each of the groups (Figure 5.2h). This indicates that the group of higher deforming cells have more pronounced corners at the base of the bullet shape, as well as some negative curvature in between the corners. This observation is demonstrated quantitatively by dividing the cells into thirds (gray lines) and calculating the bending factor for each section (Figure 5.2i). This analysis illustrates that there is some increased deformation at the front of the cell (Section 0), but that the back thirds (Section 1 & Section 2) have a much higher bending factor. This, along with the chromatin content indicates that the difference in deformation is likely due to differences in the actin cortex in the cytoskeleton, rather than due to nuclear effects. Similar spread in deformability may be visible with other imaging methods or deformability calculations, but FI-DC is able to give more insight into the local changes that may contribute to deformation differences.

5.2.5 Neutrophil extracellular traps

We use FI-DC to study changes associated with NETosis in neutrophils. We induce NETosis in neutrophils from two healthy donors by stimulating *in vitro* with 2 nM PMA for 1.5 hours and comparing to a vehicle control. In both donors, we observe a decrease in chromatin content, with an increase in cell deformability (Figure 5.3a). Cell and nuclear traces from five cells from the center of the cell distributions illustrate the changes in the cells. The

cells appear to have grown, and become more bullet shaped, indicating that the chromatin content may not have decreased with PMA treatment. The nuclear bending factor of the PMA treated neutrophils shows a trend towards lower values, which is loosely correlated with chromatin content (Figure 5.3b). We do not use the nuclear bending factor as a measure of nuclear deformation, but instead to describe its shape. In this case, the lower nuclear bending factor indicates the nuclei have become less lobular and are becoming rounder. Finally, while both cell deformability and nuclear bending factor have changed with PMA stimulation, the two measures do not appear to be correlated (Figure 5.3c).

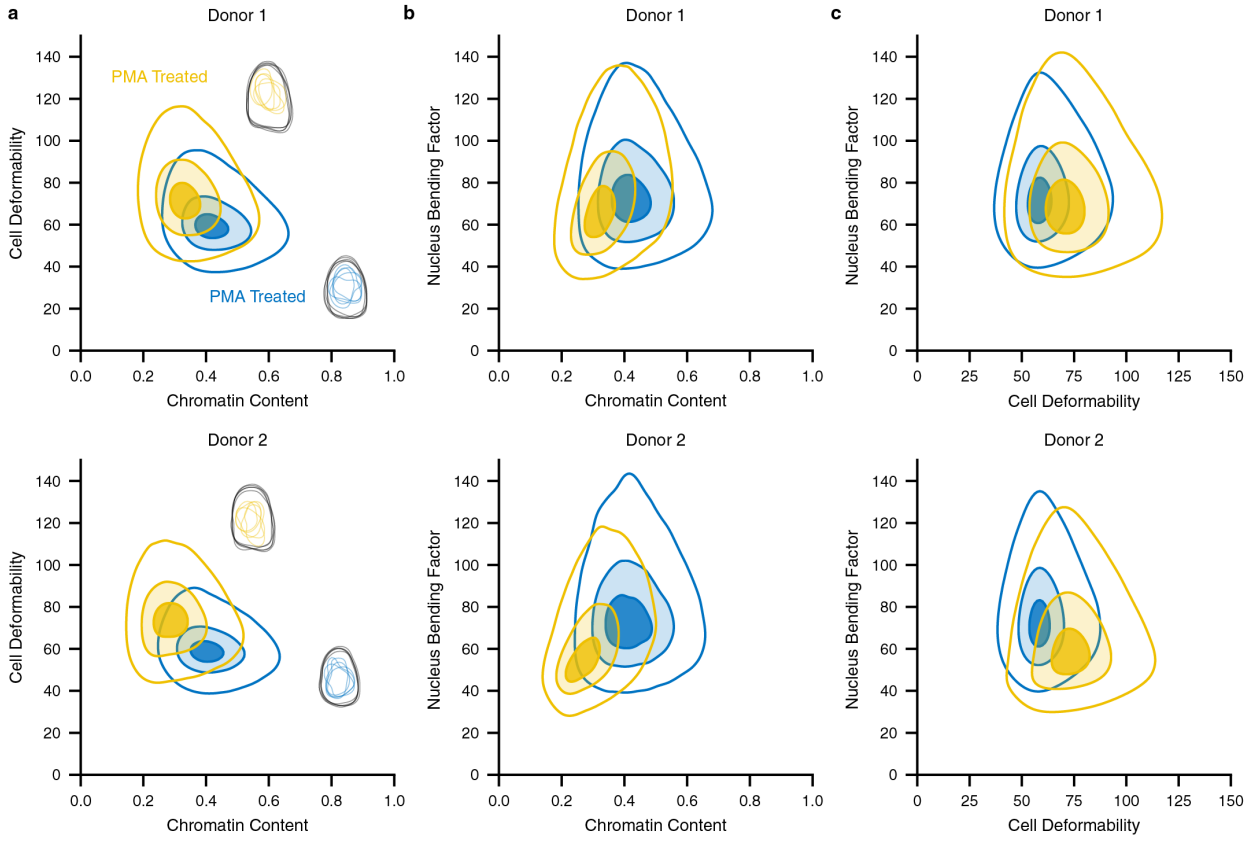

Figure 5.3: **FI-DC reveals changes in NETosing neutrophil deformation and structure.** (**a**) Stimulated neutrophils from two donors have increased cell deformability and reduced chromatin content. Traces from 5 cells from each condition reveal cells have increased in size. (**b**) The nucleus bending factor of stimulated neutrophils is slightly lower, as the cells begin the NETosis process. (**c**) There is not visible correlation between cell

deformability and the shape of nuclear structure (nuclear bending factor).

Stimulation of neutrophils with PMA results in marked increases in cell area and cell deformability (Figure 5.4a) in both blood donors. The PMA-treated distributions have a clear shift in their center of mass, but it is clear via the density contours that there remains a portion of the distributions co-located with the untreated neutrophils, indicating that not all neutrophils are stimulated equally. To compare how the mechanical properties of similarly sized cells compare, we have previously developed a measure of relative deformability [11]. Relative deformability normalizes the median deformability of treated cells within a narrow size range by the median deformability of control cells. This normalization allows us to compare values more confidently between experiments, and across platforms. Selecting a narrow size range, we can see that there is a clear shift in cell deformability of the PMA treated neutrophils, and that all distributions are strongly skewed (Figure 5.4b). Rather than converting thousands of cell measurements into a single value of relative deformability, or risk taking the median of a complex distribution, we construct relative deformability distributions instead.

Relative deformability distributions normalize entire deformability distributions, not just measures of central tendencies. Relative deformability distributions are bootstrapped by randomly sampling pairs of values from each treatment and its corresponding control and dividing them (Figure 5.4c). In this way, we get a more complete understanding of the control distribution, which is normalized against itself, instead of simply having a relative deformability of 1. Sampling in this way, we can still observe a shift in the PMA-treated neutrophils. Additionally, because of the resampling, the relative deformability distributions are roughly t-distributed, making them easier to model and compare. These distributions are compared and modeled with Bayesian inference [33]. The difference in treatment means from control is significantly greater for both Donor 1 (median=0.0649, 94% CI [0.0578, 0.0728]) and Donor 2 (median=0.04, 94% CI [0.0307, 0.0486]). The scale parameter σ for Donor 1 is significantly greater than that of the control (median=0.011, 94% CI [0.00524,

0.0177]), while the difference for Donor 2 is not significantly greater (median=0.0037, 94% CI [-0.00368, 0.0108]). We believe this calculation of a relative deformability distribution is a more accurate and richer metric for changes in deformability.

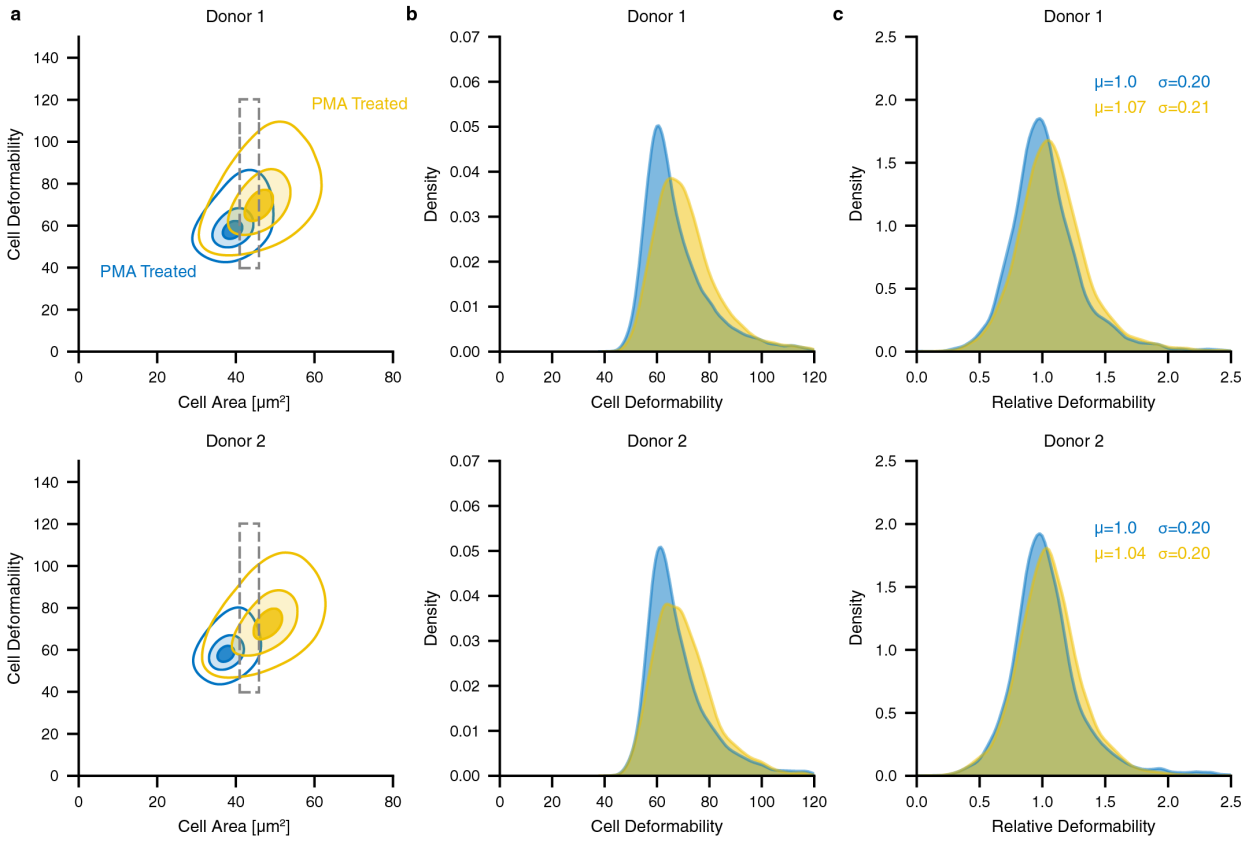

Figure 5.4: **NETosing neutrophils have increased cell deformability.** (**a**) NETosing neutrophils demonstrate a drastic increase in cell size and deformability. (**b**) The cell deformability of neutrophils from a narrow size range is compared, which illustrates a small shift in deformability. (**c**) Distributions of cell deformability are normalized, which also show an increase in treated neutrophils. Bayesian analysis indicates that there is a significant change in the distributions' means when modeled as *t*-distributions.

5.2.6 NETosing neutrophil classification

With this platform we not only want to measure NETosing neutrophils but detect them in flow as well. We perform random forest classification on the treated and untreated neu-

trophils by pooling the measured cells from both donors. These cells are split into training (n=67,530) and test (n=22,510) sets. The classifier is trained using features calculated from the brightfield and fluorescence images, and achieves 85% classification accuracy, with untreated and treated precision values of 84% and 86% respectively, and recall values of 88% and 82% respectively. We perform permutation importance tests that reveal the cell area is by far the most useful feature to classify treated neutrophils, followed by cell deformability (See Supp Figure 5.A.1a for list of features and relative importance). Due to the drastic change in cell size following PMA stimulation, we construct a new classifier, excluding features relating to cell size including cell area, cell length, cell width, cell perimeter, and chromatin content. This classifier has decreased performance, but not by much, as it has a classification accuracy of 79.7%. This classifier has untreated and treated precision values of 80% and 79% respectively, and recall values of 82% and 77% respectively. Permutation tests reveal that this classifier's most useful features are overall cell deformability, followed by the bending factor of the two back corners of the cell, and then the bending factor of the front of the cell (See Figure 5.A.1b for list of features and relative importance). These results are consistent with the higher deformability Jurkat cells which experienced more deformation in the back corners (Figure 5.2h). These classification results indicate that NETosing neutrophils can be identified in FI-DC, not only due to their increase in size, but due to their deformation as well.

5.3 Discussion

Here we have presented FI-DC, a platform that enables fluorescence imaging with high throughput cell deformability in flow. This technology enables morphological cell measurements to be combined with intracellular information, such as nuclear structure. Additionally, we have proposed a new method to quantify the deformation of hydrodynamically deformed cells, by calculating local curvature along the cell perimeter, which can be integrated into a summary bending factor. These measurements allow us finer insight into how cells may deform locally. Using this platform, we have been able to identify Jurkat subpopulations

by nuclear structure and characterize the change in mechanical properties of NETosing neutrophils. Finally, we developed a new measure to compare changes in deformability by generating relative deformability distributions.

Deformability methods can be characterized by how they deform cells, and how that deformation is measured. With the exception of AFM-based methods [7], many deformability cytometry platforms measure the entire deformation of the cell. This is even though the cell is comprised of multiple components including the actin cortex and nucleus, and all regions of a cell may not experience the same stresses. To that end, we have calculated the curvature of the cell perimeter, which gives us local information about the shape of the cell membrane. This type of analysis can help explain the difference in the shape of cells with different deformability. By itself, understanding the magnitude and sign of curvature is valuable. But the curvature can be summarized via the scale-invariant bending factor, which quantifies how the cell deviates from a perfectly undeformed circle. Additionally, the bending factor can be calculated for sections along the cell perimeter, giving a standardized, midlevel quantification between overall bending factor and curvature. These measurement techniques can be applied to any image-based deformability platform, although it requires sufficiently smooth and accurate cell boundaries.

Using this platform, we investigated the natural variation in mechanical properties of Jurkat cells. FI-DC allowed us to identify cells with varying chromatin content, that would have been missed with non-fluorescent imaging. The identified cells with reduced chromatin content had increased cell size and cell deformability, although we were unable to determine if the increase in deformability was independent of the size change. Using the capability to measure chromatin content and local cell membrane deformation, we were able to determine that cells of similar size with different levels of deformation do not differ in their chromatin content, but in how the actin cortex is likely deforming.

We further demonstrated the capabilities of the FI-DC by measuring neutrophils undergoing NETosis. In NETosis, the neutrophil's chromatin decondenses and is released extracellularly. We expected during this process that we would be able to witness the visible spread

of chromatin in the cell, as well as a change in mechanical properties. While we did observe an increase in deformability over control cells, we did not witness the change in nuclear structure, likely because our incubation timescales or PMA dose was not high enough.

In addition to measuring the change in mechanical properties in flow, we would like to be able to identify and eventually sort the cells, which may further study or utility of NETosing neutrophils. Using features calculated from the brightfield and FITC images, we developed a random forest classifier that was able to classify untreated and treated neutrophils with 85% accuracy. This classifier identified the large change in cell area of PMA treated neutrophils as the most useful feature in classification. When excluding cell size related features, we were still able to achieve a classification accuracy of almost 80%, with cell deformability and the bending factor of the back region of the cell being most important. More accurate classification may be possible with a neural network, but in our experiments, the cell populations were run through FI-DC separately, which could induce some batch effects in images. Finally, here we were trying to classify cells that came from treated and untreated samples. But that does not address whether cells were NETosing. A more useful classifier would predict which cells are actively NETosing. NETosis status could perhaps be indicated by nuclear changes or staining for MPO [26]. In our case, we were unable to find a suitable fluorescent biomarker probe that did not require fixing or permeabilizing the neutrophils.

In the future, we would like to more completely characterize the NETosing landscape. This would entail measuring neutrophils that have been stimulated for different durations, with different PMA doses. We believe that with the dose and duration used here, the neutrophils have only just begun to undergo internal changes, and have not yet decondensed their chromatin, or broken down the nuclear envelope. One challenge we face in this regard is handling and preserving cells undergoing NETosis. This process makes them especially sticky and fragile, and we cannot fix the cells as some other imaging studies have done.

We would like to our understanding of the capabilities of our platform for future use. We have demonstrated the effect that the fluid viscosity has on our ability to deform cells.

This type of shear flow deformability cytometry may be capable of deforming the nucleus, although that was not shown here [11]. It may be possible to achieve these higher levels of deformation by further increasing the viscosity of solutions, or perhaps by increasing the duration of time that the cells are being deformed. Furthermore, we can demonstrate our ability to differentiate cells in different stages of the cell cycle using the fluorescent nuclear images of FI-DC. Cells in different cell stages have been shown to deform differently [2], but this required chemically synchronizing cells. With FI-DC, intricately designed experiments to ensure synchronized cells would become less necessary. Beyond imaging and characterizing nuclear structure, FI-DC may be leveraged to stain for other biomarkers or intracellular components, which will create a more complete understanding of cell identity and its resulting mechanical properties.

5.4 Materials and methods

5.4.1 Alginate solution preparation

Alginate solutions were prepared by dissolving sodium alginate in deionized water (sheath) or sterile PBS (sample). The solutions were stirred overnight at room temperature on a stir plate until visibly dissolved. Sample stream alginate solutions were prepared at 2x concentration in order to reach proper concentration when added to cell solution.

5.4.2 Cells and treatment

The Jurkat cell line was cultured in ATCC-modified RPMI 1640 medium (Gibco) with 1% penicillin/streptomycin (Gibco), 1% 1M HEPES buffer and 10% heat-inactivated FBS (Gibco). Cells were grown at 37℃, with 5% CO_2, at densities between 10^5 and 10^6 cells $\cdot$ mL^{-1} with subculturing every second day.

5.4.3 Neutrophil isolation

Neutrophils were isolated as previously described [34], and cultured in ATCC-modified RPMI 1640 medium (Gibco) with 1% penicillin/streptomycin (Gibco), 1% 1M HEPES buffer and 2% heat-inactivated FBS (Gibco). Cells were cultured at 37℃, with 5% CO_2 in non-tissue treated well plates on an orbital shaker at densities between 5×10^5 and 10^6 cells $\cdot$ mL^{-1}.

5.4.4 Neutrophil stimulation

Neutrophils were stimulated at 2 nM PMA using 2 µm PMA solution prepared in DMSO at 1:1,000 dilution. Unstimulated receive equivalent vehicle control of DMSO at 1:1,000 dilution. After stimulation and incubation on an orbital shaker in the incubator, neutrophils were collected following vigorous pipetting, followed by a PBS wash step. Cells were spun at $400g$ for 5 minutes and resuspended in 325 µL 1% BSA PBS solution. Cells were stained with 1 µL Syto16 nuclear stain and incubated on the orbital shaker in the incubator for 10 minutes. The solution was spiked with 3 µL of 10 µm fluorescent beads and 325 µL alginate solution was added to achieve final alginate concentration. The solution was gravity filtered with a pre-wet 20 µm cell strainer before being loaded into a 1 mL syringe.

5.4.5 Device design and operation

Soft lithography was used to fabricate polydimethylsiloxane (PDMS) devices which were bonded to glass slides. The device has one sample inlet and two sheath flow inlets that meet and flow together through a straight channel. The straight channel has a width of 25 µm

and height of 30 µm . The sample stream was injected via syringe pump at 10 µL · min^{-1}, and each of the sheath flow were injected at 5 µL · min^{-1}. Cells were imaged via FIRE in the middle of the straight channel section. The FIRE equipment was operated with a 488 nm laser operating at 80 mW with a FITC (529/28 nm) bandpass filter. The transmitted light was measured using a photodiode to generate brightfield images while side scattered light was collected with a PMT to generate darkfield images. Image capture was triggered by a sufficiently low fluorescence signal threshold to capture any object with fluorescence in FITC channel. All generated images have a pixel pitch of 0.25 µm per pixel. Devices were cleaned after each use by running 800 µL dilute bleach followed by 800 µL PBS through the tubing and device between each sample. Images are analyzed by custom `Python` scripts.

5.4.6 Cell image classification with neural network

A neural network was trained to distinguish clean images of single cells from debris, dead cells, doublets, etc. A VGG16 architecture pretrained on ImageNet [35] was finetuned on 48,000 FIRE images using `Keras` and `TensorFlow2`. Results were human verified and corrected to ensure only single, live cell images were analyzed.

5.4.7 Cell segmentation with U-Net

Segmentation of cells and nuclear structure, from brightfield and FITC images, respectively was performed by a U-Net neural network [30]. The brightfield and FITC image neural networks were trained on 560 and 275 FIRE cell images, respectively. We filled in holes and performed small morphological opening and closing on cell binary images.

5.4.8 Contour extraction and smoothing

Boundaries of cells and nuclei were extracted from binary masks. Boundaries were smoothed to remove pixelation effects by first downsampling so that all vertices are 1.5 pixels widths apart, followed by local regression. Standard shape measurements are extracted from the

boundaries including cell area, width, length and perimeter.

5.4.9 Calculation of bending factor

For easy comparison, all cell and nucleus boundaries were converted to polar coordinates and interpolated to 120 points (3° apart). Curvature along the arc length parametrized boundaries ($\kappa(s)$) was calculated at each point according to [31]:

$$\kappa(s) = \frac{x(s)'y(s)'' - y(s)'x(s)''}{\left(x(s)'^2 + y(s)''^2\right)^{3/2}} \tag{5.1}$$

The scale-invariant bending factor (known as scale-invariant bending energy in other fields) was calculated from the curvature along the boundaries and allowed for comparison of similar shapes of different size, where P is the perimeter along the boundary [32]:

$$B = P \int_0^P \kappa(s)^2 ds \tag{5.2}$$

Finally, the bending factor of a portion of the boundary from a to b can be calculated as well:

$$B_{ab} = P \int_a^b \kappa(s)^2 ds \tag{5.3}$$

5.4.10 Bayesian inference

Bayesian inference is conducted with `PyMC3` [36] and No U-Turn MCMC Sampler [37] to model relative deformability distributions as a t-distribution.

5.A Appendix

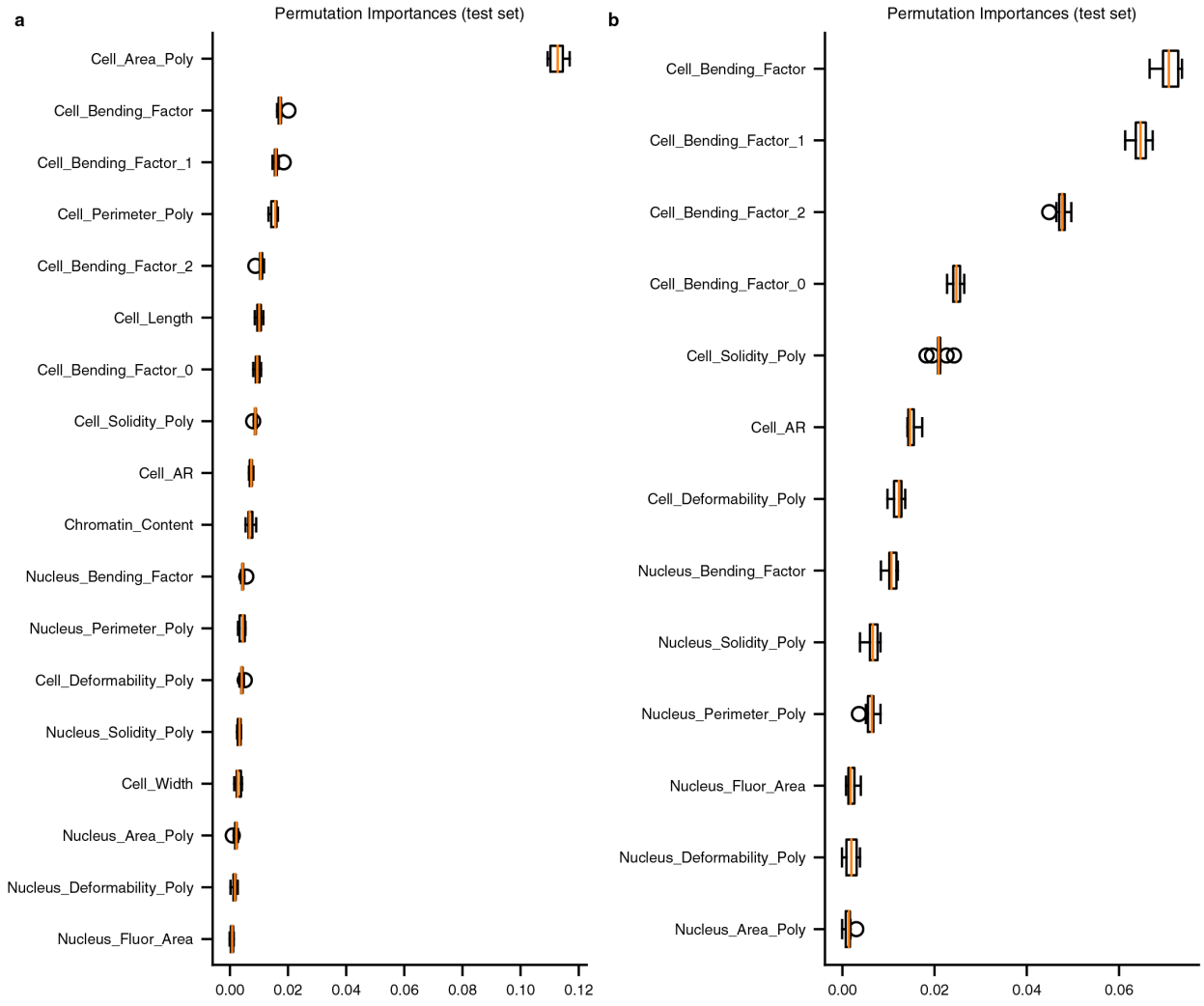

Figure 5.A.1: **Relative feature importance from neutrophil classifiers.** (**a**) A random forest classifier is trained to distinguish treated and untreated neutrophils using features generated from FIRE images. Relative feature importance shows that cell area is the most important feature, followed by the cell bending factor. (**b**) A second random forest classifier is trained only features that exclude information on cell size. Cell bending factor is the most important feature, followed by the section bending factors of the lower sections of the cell.

Bibliography

[1] Eric M. Darling and Dino Di Carlo. High-Throughput Assessment of Cellular Mechanical Properties. *Annual Review of Biomedical Engineering*, 17(1):35–62, 2015.

[2] Oliver Otto, Philipp Rosendahl, Alexander Mietke, Stefan Golfier, Christoph Herold, Daniel Klaue, Salvatore Girardo, Stefano Pagliara, Andrew Ekpenyong, Angela Jacobi, Manja Wobus, Nicole Töpfner, Ulrich F Keyser, Jörg Mansfeld, Elisabeth Fischer-Friedrich, and Jochen Guck. Real-time deformability cytometry: on-the-fly cell mechanical phenotyping. *Nature Methods*, 12(3):199–202, 2015.

[3] T J Thauland, K H Hu, M A Bruce, and M J Butte. Cytoskeletal adaptivity regulates T cell receptor signaling. *Sci Signal*, 10(469):1–11, 2017.

[4] Henry T K Tse, Daniel R Gossett, Yo Sup Moon, Mahdokht Masaeli, Marie Sohsman, Yong Ying, Kimberly Mislick, Ryan P Adams, Jianyu Rao, and Dino Di Carlo. Quantitative diagnosis of malignant pleural effusions by single-cell mechanophenotyping. *Science translational medicine*, 5(212):212ra163, 2013.

[5] D. R. Gossett, H. T. K. Tse, S. a. Lee, Y. Ying, a. G. Lindgren, O. O. Yang, J. Rao, a. T. Clark, and D. Di Carlo. Hydrodynamic stretching of single cells for large population mechanical phenotyping. *Proceedings of the National Academy of Sciences*, 109(20):7630–7635, 2012.

[6] Jonathan Lin, Donghyuk Kim, Henry T. Tse, Peter Tseng, Lillian Peng, Manjima Dhar, Saravanan Karumbayaram, and Dino Di Carlo. High-throughput physical phenotyping of cell differentiation. *Microsystems & Nanoengineering*, 3:17013, May 2017.

[7] Manfred Radmacher. Studying the Mechanics of Cellular Processes by Atomic Force Microscopy. *Methods in Cell Biology*, 83(07):347–372, 2007.

[8] Blanca González-Bermúdez, Gustavo V. Guinea, and Gustavo R. Plaza. Advances in Micropipette Aspiration: Applications in Cell Biomechanics, Models, and Extended Studies, feb 2019.

[9] Jochen Guck, Revathi Ananthakrishnan, Hamid Mahmood, Tess J. Moon, C. Casey Cunningham, and Josef Käs. The optical stretcher: A novel laser tool to micromanipulate cells. *Biophysical Journal*, 81(2):767–784, aug 2001.

[10] Kendra D. Nyberg, Kenneth H. Hu, Sara H. Kleinman, Damir B. Khismatullin, Manish J. Butte, and Amy C. Rowat. Quantitative Deformability Cytometry: Rapid, Calibrated Measurements of Cell Mechanical Properties. *Biophysical Journal*, 113(7):1574–1584, 2017.

[11] Marta Urbanska, Hector E. Muñoz, Josephine Shaw Bagnall, Oliver Otto, Scott R. Manalis, Dino Di Carlo, and Jochen Guck. A comparison of microfluidic methods for high-throughput cell deformability measurements. *Nature Methods*, pages 1–7, apr 2020.

[12] Janina R. Lange, Julian Steinwachs, Thorsten Kolb, Lena A. Lautscham, Irina Harder, Graeme Whyte, and Ben Fabry. Microconstriction Arrays for High-Throughput Quantitative Measurements of Cell Mechanical Properties. *Biophysical Journal*, 109(1):26–34, 2015.

[13] Mahdokht Masaeli, Dewal Gupta, Sean O'Byrne, Henry T. K. Tse, Daniel R. Gossett, Peter Tseng, Andrew S. Utada, Hea-Jin Jung, Stephen Young, Amander T. Clark, and Dino Di Carlo. Multiparameter mechanical and morphometric screening of cells. *Scientific Reports*, 6(1):37863, Dec 2016.

[14] Amy C. Rowat, Diana E. Jaalouk, Monika Zwerger, W. Lloyd Ung, Irwin A. Eydelnant, Don E. Olins, Ada L. Olins, Harald Herrmann, David A. Weitz, and Jan Lammerding. Nuclear envelope composition determines the ability of neutrophil-type cells to passage through micron-scale constrictions. *Journal of Biological Chemistry*, 288(12):8610–8618, 2013.

[15] Sangwon Byun, Vivian C. Hecht, and Scott R. Manalis. Characterizing Cellular Biophysical Responses to Stress by Relating Density, Deformability, and Size. *Biophysical Journal*, 109(8):1565–1573, Oct 2015.

[16] Philipp Rosendahl, Katarzyna Plak, Angela Jacobi, Martin Kraeter, Nicole Toepfner, Oliver Otto, Christoph Herold, Maria Winzi, Maik Herbig, Yan Ge, Salvatore Girardo, Katrin Wagner, Buzz Baum, and Jochen Guck. Real-time fluorescence and deformability cytometry. *Nature Methods*, 15(5):355, 2018.

[17] Xuan Cao, Emad Moeendarbary, Philipp Isermann, Patricia M. Davidson, Xiao Wang, Michelle B. Chen, Anya K. Burkart, Jan Lammerding, Roger D. Kamm, and Vivek B. Shenoy. A Chemomechanical Model for Nuclear Morphology and Stresses during Cell Transendothelial Migration. *Biophysical Journal*, 111(7):1541–1552, 2016.

[18] Hawa Racine Thiam, Pablo Vargas, Nicolas Carpi, Carolina Lage Crespo, Matthew Raab, Emmanuel Terriac, Megan C. King, Jordan Jacobelli, Arthur S. Alberts, Theresia Stradal, Ana Maria Lennon-Dumenil, and Matthieu Piel. Perinuclear Arp2/3-driven actin polymerization enables nuclear deformation to facilitate cell migration through complex environments. *Nature Communications*, 7, 2016.

[19] J. David Pajerowski, Kris Noel Dahl, Franklin L. Zhong, Paul J. Sammak, and Dennis E. Discher. Physical plasticity of the nucleus in stem cell differentiation. *Proceedings of the National Academy of Sciences of the United States of America*, 104(40):15619–15624, 2007.

[20] Sungrim Seirin-Lee, Fumitaka Osakada, Junichi Takeda, Satoshi Tashiro, Ryo Kobayashi, Takashi Yamamoto, and Hiroshi Ochiai. Role of dynamic nuclear deformation on genomic architecture reorganization. *PLoS Computational Biology*, 15(9):1–25, 2019.

[21] Venizelos Papayannopoulos. Neutrophil extracellular traps in immunity and disease. *Nature Reviews Immunology*, 18(2):134–147, 2018.

[22] Volker Brinkmann, Ulrike Reichard, Christian Goosmann, Beatrix Fauler, Yvonne Uhlemann, David S. Weiss, Yvette Weinrauch, and Arturo Zychlinsky. Neutrophil Extracellular Traps Kill Bacteria. *Science*, 303(5663):1532–1535, mar 2004.

[23] Keum Hwa Lee, Andreas Kronbichler, David Duck Young Park, Young Min Park, Hanwool Moon, Hyungdo Kim, Jun Hyug Choi, Young Seo Choi, Songjoo Shim, Il Suk Lyu, Byung Hwan Yun, Yeonseung Han, Donghee Lee, Sang Yoon Lee, Byung Hun Yoo, Kyung Hwan Lee, Tai Lim Kim, Heonki Kim, Joo Sung Shim, Wonseok Nam, Heesung So, Soo Yeon Choi, Sangmok Lee, and Jae Il Shin. Neutrophil extracellular traps (NETs) in autoimmune diseases: A comprehensive review, nov 2017.

[24] Sinuhe Hahn, Stavros Giaglis, Irene Hoesli, and Paul Hasler. Neutrophil NETs in reproduction: From infertility to preeclampsia and the possibility of fetal loss. *Frontiers in Immunology*, 3(NOV):1–8, 2012.

[25] Elsa Neubert, Daniel Meyer, Francesco Rocca, Gökhan Günay, Anja Kwaczala-Tessmann, Julia Grandke, Susanne Senger-Sander, Claudia Geisler, Alexander Egner, Michael P. Schön, Luise Erpenbeck, and Sebastian Kruss. Chromatin swelling drives neutrophil extracellular trap release. *Nature Communications*, 9(1):1–13, dec 2018.

[26] Wenpu Zhao, Darin K. Fogg, and Mariana J. Kaplan. A novel image-based quantitative method for the characterization of NETosis. *Journal of Immunological Methods*, 423:104–110, aug 2015.

[27] Ahmad Ahsan Nawaz, Marta Urbanska, Maik Herbig, Martin Nötzel, Martin Kräter, Philipp Rosendahl, Christoph Herold, Nicole Toepfner, Markéta Kubánková, Ruchi Goswami, Shada Abuhattum, Felix Reichel, Paul Müller, Anna Taubenberger, Salvatore Girardo, Angela Jacobi, and Jochen Guck. Intelligent image-based deformation-assisted cell sorting with molecular specificity. *Nature Methods*, 17(6):595–599, jun 2020.

[28] Eric D Diebold, Brandon W Buckley, Daniel R Gossett, and Bahram Jalali. Digitally synthesized beat frequency multiplexing for sub-millisecond fluorescence microscopy. *Nature Photonics*, 7(10):806–810, sep 2013.

[29] Muzaffar H. Panhwar, Fabian Czerwinski, Venkata A.S. Dabbiru, Yesaswini Komaragiri, Bob Fregin, Doreen Biedenweg, Peter Nestler, Ricardo H. Pires, and Oliver Otto. High-throughput cell and spheroid mechanics in virtual fluidic channels. *Nature Communications*, 11(1), 2020.

[30] Olaf Ronneberger, Philipp Fischer, and Thomas Brox. U-net: Convolutional networks for biomedical image segmentation. *Lecture Notes in Computer Science (including subseries Lecture Notes in Artificial Intelligence and Lecture Notes in Bioinformatics)*, 9351:234–241, 2015.

[31] Andreas Backhaus, Asuka Kuwabara, Marion Bauch, Nick Monk, Guido Sanguinetti, and Andrew Fleming. Leafprocessor: A new leaf phenotyping tool using contour bending energy and shape cluster analysis. *New Phytologist*, 187(1):251–261, 2010.

[32] Roberto Marcondes Cesar and Luciano Da Fontoura Costa. Application and assessment of multiscale bending energy for morphometric characterization of neural cells. *Review of Scientific Instruments*, 68(5):2177, 1997.

[33] John K. Kruschke. *Doing Bayesian data analysis : a tutorial with R, JAGS, and Stan*. Academic Press, 2nd edition, 2014.

[34] William M. Nauseef. Isolation of human neutrophils from venous blood. *Methods in Molecular Biology*, 1124:13–18, 2014.

[35] Karen Simonyan and Andrew Zisserman. Very deep convolutional networks for large-scale image recognition. *3rd International Conference on Learning Representations, ICLR 2015 - Conference Track Proceedings*, pages 1–14, 2015.

[36] John Salvatier, Thomas V. Wiecki, and Christopher Fonnesbeck. Probabilistic programming in Python using PyMC3. *PeerJ Computer Science*, 2:e55, apr 2016.

[37] Matthew D. Hoffman and Andrew Gelman. The no-U-turn sampler: Adaptively setting path lengths in Hamiltonian Monte Carlo. *Journal of Machine Learning Research*, 15:1593–1623, 2014.

CHAPTER 6

Concluding remarks

Mechanical phenotyping has been shown to be a useful tool in characterizing cell identity and function. It has largely been utilized in a manner that summarizes the mechanical properties of the entire cell, but there is a great value in understanding how components of a cell differentially contribute to overall deformability. Until now, understanding how the intracellular components contribute to cell mechanical properties required careful experiment design to isolate effects to the cytoskeleton or nucleus. Combining cell deformability with fluorescent imaging allows us to visualize intracellular components, and understand how their size, structure and location influence overall cell deformation. These developments require improvements in imaging technologies and deformability platform design.

This approach may give us a greater understanding and confidence in the mechanical phenotypes measured, and further the field. Although not all existing methods can be integrated with new imaging technologies, this would further our understanding of how different deformability platforms deform cells, and what they are measuring.

Throughout biological research, images provide a valuable resource. Despite the rich information that images provide they have not always been able to provide speed that high throughput methods require. As imaging methods improve and become faster and cheaper, they can be used more widely, and improve the speed of growth in science. These improvements will be integral in novel cell sorting methods. Cell sorting has been largely been absent from cell deformability platforms until recently. But the greater capabilities that arise from the intersection of these technologies will improve our study of cells and validate our hypotheses that surround cells' deformability and their identity or behavior.